MONITEUR D'IMAGES SOLAIRES FRANCO-ALGERIEN

[M. I. Sol. F. A.]

Premier document de travail

Présentation Générale et Cahier des charges

P. ASSUS, J. BORGNINO, A. IRBAH, F. MARTIN

Mars 2000

I - INTRODUCTION

Ce moniteur d'images solaires va être construit dans le contexte général de l'observation du Soleil à haute résolution angulaire avec pour les télescopes en station au sol, la mise en œuvre de la technique d'optique adaptative (par exemple dans sa forme multiconjuguée : conjugaison des miroirs adaptatifs avec différentes zones de l'atmosphère terrestre turbulente). Il s'agit plus largement de développer des techniques d'imagerie au-delà du domaine isoplanétique. Ce moniteur fonctionnera simultanément à un ensemble d'expériences utilisées pour mesurer le diamètre solaire (astrolabe, expérience DORAYSOL, réplique au sol de l'expérience spatiale PICARD). L'objectif poursuivi est la confrontation des résultats obtenus à partir de l'espace d'une part et à partir du sol d'autre part. Cela permettra d'estimer les effets atmosphériques sur les mesures, d'évaluer celles qui ont été effectuées antérieurement, soit tout d'abord de manière visuelle, soit ensuite en utilisant une caméra CCD, ainsi que celles qui seront effectuées ultérieurement à l'expérience spatiale.

Dans les prochains paragraphes, on rappellera rapidement les effets introduits par la turbulence atmosphérique dans la formation des images astronomiques, les paramètres pertinents ainsi que les différents modèles généralement utilisés. Puis, on montrera que l'analyse statistique des fluctuations d'angle d'arrivée mises en évidence par observation du bord solaire (ces fluctuations seront observées simultanément dans le plan image et dans le plan pupille) conduit à l'estimation de ces paramètres et à la modélisation des phénomènes turbulents. On présentera ensuite le dispositif expérimental proposé en soulignant les contraintes liées à l'acquisition des données. Les différentes méthodes de traitement conduisant à l'estimation des paramètres seront décrites brièvement (dans ce premier document) et un certain nombre de références bibliographiques seront données ainsi qu'un choix d'articles en annexe. Les principaux résultats obtenus lors d'études concernant les effets atmosphériques intervenant dans l'erreur commise sur la mesure du diamètre solaire seront rappelés.

II - LA TURBULENCE ATMOSPHERIQUE ET LES OBSERVATIONS A HAUTE RESOLUTION ANGULAIRE

L'atmosphère terrestre est en permanence le siège de phénomènes turbulents. On peut tout d'abord distinguer la turbulence dynamique provoquée principalement, dans la haute atmosphère, par le cisaillement du à une différence de vitesses à l'intérieur d'une couche atmosphérique et à la viscosité de l'air. L'atmosphère apparaît donc stratifiée en couches turbulentes plus ou moins énergétiques. De plus, au niveau du sol, on doit prendre en compte une turbulence de nature convective due à l'échauffement du sol et des structures instrumentales. Cette turbulence sera souvent prépondérante lors des observations effectuées le jour.

Pour les observations astronomiques, il est nécessaire de définir une turbulence dite "turbulence optique" qui se traduit par des perturbations aléatoires des surfaces d'onde lumineuses arrivant sur la pupille d'entrée des instruments. Pour décrire schématiquement cette turbulence optique, on peut considérer que la turbulence dynamique brasse des fluctuations aléatoires de température (et d'humidité). Ces fluctuations entraînent des fluctuations aléatoires de la phase des surfaces d'onde. Selon la distance à laquelle se produisent les phénomènes turbulents, on observera au sol des fluctuations de la phase et/ou de l'intensité. Pour cette turbulence, que l'on prend en compte lors des observations astronomiques, l'énergie apparaît sous forme de profils verticaux de la constante de structure des fluctuations de l'indice de réfraction de l'air $C_n^2(h)$ (h notant l'altitude), définie par :

$$D_n(\underline{\rho}) = C_n^2 \, \rho^{2/3} \qquad \text{[Loi de Kolmogorov-Obukhov]}$$

avec

$$D_n(\underline{\rho}) = < [\tilde{n}(\underline{r}) - \tilde{n}(\underline{r}+\underline{\rho})]^2 >$$

qui est la fonction de structure tridimensionnelle des fluctuations d'indice,

et $\rho = |\underline{\rho}|$ qui est la distance à laquelle on effectue les observations.

Du point de vue de la localisation de la turbulence, on distingue principalement 2 régions :

- la Couche Limite Atmosphérique (CLA), qui correspond au premier kilomètre de l'atmosphère. Dans le cas de l'observation du Soleil, il sera nécessaire d'étudier tout particulièrement l'influence de la Couche Limite Superficielle (CLS) (0-30m).
- et l'Atmosphère Libre dans laquelle apparaissent des couches turbulentes discrètes.

Dans la suite, on utilisera le concept de "couche turbulente équivalente" : il sera toujours possible de définir les caractéristiques (énergie, vitesse, altitude) d'une couche turbulente unique donnant au sol les mêmes effets sur les surfaces d'onde que l'atmosphère turbulente réelle.

Pour modéliser les effets introduits sur les images, il est nécessaire d'estimer des paramètres associés aux fluctuations locales ($C_n^2(h)$ et profil des vitesses des couches $\underline{v}(h)$) ou des paramètres optiques associés aux fronts d'onde arrivant sur la pupille d'entrée du télescope. Ces paramètres chiffrent les différentes cohérences de ces fronts d'onde.

Pour la cohérence spatiale, on distingue:

- le paramètre de Fried r_0 , que l'on peut assimiler au diamètre de la surface de cohérence du front d'onde perturbé. Il définit, à long temps de pose, le diamètre d'un télescope fictif qui, en l'absence de turbulence, donnerait la même résolution qu'un télescope de diamètre infini en présence de turbulence.
- les échelles limites de cohérence spatiale (échelle interne l_0 , échelle externe L_0) entre lesquelles se situent les tailles des différentes perturbations observées sur les fronts d'onde.

Ces paramètres permettent de formaliser (densité spectrale ou fonction de structure des fluctuations de phase) les différents modèles utilisés pour décrire la statistique de ces perturbations. Il est ensuite possible d'évaluer le filtrage linéaire réalisé sur les composantes harmoniques des objets astronomiques observés par l'ensemble constitué par le télescope et l'atmosphère.

On trouve dans la littérature différents modèles (dans la suite $\underline{f}$ représente une fréquence spatiale). On donnera ci-dessous pour illustrer ces modèles dans chaque cas l'expression de la densité spectrale des fluctuations de phase. On pourra ainsi considérer :

- le modèle de Kolmogorov-Tatarski, valable pour des décalages spatiaux compris entre les échelles limites, avec :

$$W\varphi(\underline{f}) = 0.0228\, r_0^{-5/3}\, f^{-11/3}$$

- le modèle de Von Karman, qui permet de prendre en compte directement dans la formulation mathématique les effets introduits par les échelles limites,

$$W\varphi(\underline{f}) = 0.0228\, r_0^{-5/3} (f^2 + 1/L_0^2)^{-11/6} \exp(-\alpha f^2 l_0^2)$$

expression dans laquelle

$$\alpha = (2\pi / 5.92)^2$$

- le modèle de Greenwood-Tarazano, qui a été proposé pour rendre compte de manière plus réaliste du comportement basse fréquence des fluctuations de phase,

$$W\varphi(\underline{f}) = 0.0228\, r_0^{-5/3} (f^2 + f/L_0)^{-11/6} \exp(-\alpha f^2 l_0^2)$$

- le modèle exponentiel, qui apparaît proche du modèle de Von Karman et qui peut se révéler plus commode à utiliser lors des développements analytiques,

$$W\varphi(\underline{f}) = 0.0228\, r_0^{-5/3} f^{-11/3} [1 - \exp(-f^2 L_0^2)] \exp(-\alpha f^2 l_0^2)$$

En plus de ces paramètres de cohérence spatiale, il est nécessaire de chiffrer :

- la cohérence spatiotemporelle des fronts d'onde : constante de temps τ_0

ainsi que,

- la cohérence spatioangulaire : taille du domaine d'isoplanétisme θ_0

On notera que ces paramètres doivent être définis au sens des techniques utilisées (interférométrie des tavelures, optique adaptative, angle d'arrivée).

II - L'ESTIMATION DES PARAMETRES QUALIFIANT LES IMAGES SOLAIRES A PARTIR DE L'ANALYSE STATISTIQUE DES FLUCTUATIONS D'ANGLE D'ARRIVEE

La qualification des images solaires a conduit à l'utilisation de diverses expériences basées sur l'observation des fluctuations présentées par la réponse impulsionnelle de l'atmosphère (contraste de la granulation solaire), des fluctuations d'intensité ou d'angle d'arrivée.

Pour le moniteur présenté ici, c'est l'observation des fluctuations d'angle d'arrivée qui sera utilisée. Ce choix résulte des considérations suivantes :
- Ces fluctuations sont simples à mettre en évidence, soit directement (dans le plan image) en observant le bord solaire, soit photométriquement en observant les fluctuations d'intensité dans le plan pupille à travers un diaphragme placé sur l'image du bord solaire au foyer de l'instrument (technique de type "Foucaultage"). On notera que, pour les observations de nuit, les moniteurs les plus utilisés (ESO, IAC, ONERA, GSM de l'équipe "Optique Atmosphérique" de l'UMR Astrophysique de l'Université de Nice - Sophia Antipolis) permettent de déduire les paramètres de cohérence de l'observation des fluctuations d'angle d'arrivée.
- Le moniteur devant fonctionner dans le contexte de la mesure du diamètre solaire le choix de ce concept apparaît comme naturel.
- Les proposants possèdent une forte expertise dans l'utilisation de cette technique.

Dans ce qui suit, les résultats théoriques ont été établis dans le cas du modèle de Von Karman avec une échelle interne égale à 0, une longueur d'onde égale à λ et un diamètre pupillaire égal à D.

On a montré que dans ce cadre la covariance spatiale des fluctuations d'angle d'arrivée (voir dans la bibliographie la référence "Avila et al.") s'écrivait :

$$C_\alpha(\rho) = 0.0716\lambda^2 r_0^{-5/3} \int_0^{+\infty} df.f^3 \left(f^2 + \frac{1}{L_0^2} \right)^{-11/6} \left[J_0(2\pi f\rho) \pm J_2(2\pi f\rho) \right] \left[\frac{2J_1(\pi Df)}{\pi Df} \right]^2$$

Dans cette expression, si l'on utilise la somme des 2 fonctions de Bessel J_0 et J_2 c'est que les fluctuations d'angle d'arrivée α sont considérées perpendiculairement à la base (covariance transverse); par contre, si l'on utilise la différence de ces 2 fonctions de Bessel, c'est que les fluctuations d'angle d'arrivée sont considérées parallèlement à la base (covariance longitudinale).

On peut en déduire l'expression de la fonction de structure :

$$D_\alpha(\rho) = 0.1432\lambda^2 r_0^{-5/3} \int_0^{+\infty} df.f^3 \left(f^2 + \frac{1}{L_0^2} \right)^{-11/6} \left[1 - \left(J_0(2\pi f\rho) \pm J_2(2\pi f\rho) \right) \right] \left[\frac{2J_1(\pi Df)}{\pi Df} \right]^2$$

Les 2 expressions données ci-dessus permettent donc d'interpréter les observations dans le cas où la base est orientée selon une direction parallèle ou perpendiculaire par rapport à la direction d'analyse des fluctuations. On dispose cependant par ailleurs d'une expression plus générale décrivant la statistique quelle que soit la direction de la base par rapport à celle de l'analyse.

On remarque que la mesure de cette covariance (ou de cette fonction de structure) conduit par ajustement aux données expérimentales aux estimations simultanées de r_0 et L_0 (cas d'une atmosphère ramenée à une couche turbulente équivalente). On verra plus loin (paragraphe V) que cette covariance et cette fonction de structure peuvent être transformées (moyennant des hypothèses réalistes) pour estimer le temps de cohérence et la taille du domaine d'isoplanétisme (au sens des angles d'arrivée). On présentera également dans le paragraphe V une méthode permettant d'estimer les profils verticaux d'énergie turbulente $C_n^2(h)$.

La connaissance de ces paramètres va permettre de modéliser les effets atmosphériques lors de la mesure du diamètre solaire en utilisant l'un des modèles de turbulence optique présentés ci-dessus. On pourra de plus évaluer la qualité de la modélisation et éventuellement en proposer une nouvelle.

IV - LE MONITEUR D'IMAGES SOLAIRES : PRINCIPE - DISPOSITIF EXPERIMENTAL - CONTRAINTES

Le principe de ce moniteur est basé sur l'observation simultanée des fluctuations d'angle d'arrivée dans le plan pupille (estimation du temps de cohérence) et dans le plan image (estimations des paramètres de cohérence spatioangulaire et des profils verticaux de turbulence optique).

On trouvera page suivante (hors texte) le schéma optique (hors le système de guidage).

On forme sur un capteur CCD une image du bord solaire de 32" . 32".
L'échantillonnage angulaire est de 0.5"/pixel.

Si l'on considère des pixels carrés de 10µ par 10µ, une seconde d'arc correspond à 20µ sur le capteur. Cette résolution correspond à une distance focale $f = 4m$.

Le champ utile sur le capteur est de 640µ par 640µ.

On utilise le même grandissement pour les 2 voies.

Sur la voie "**observation dans le plan pupille**", on place **une fente de 10" par 100", soit linéairement de 200µ par 2mm**. Ces dimensions typiques ont été choisies suite à des observations effectuées antérieurement.

Pour la **précision de guidage**, elle devra être **inférieure à 5" pendant le temps d'intégration égal à 2minutes (voir plus loin).**

La longueur d'onde de travail typique sera $\lambda = 530$ nm
et la bande passante spectrale $\delta\lambda = 10$ nm.

Une bonne partie du flux solaire devra être éliminée au moyen d'un filtre neutre réfléchissant.

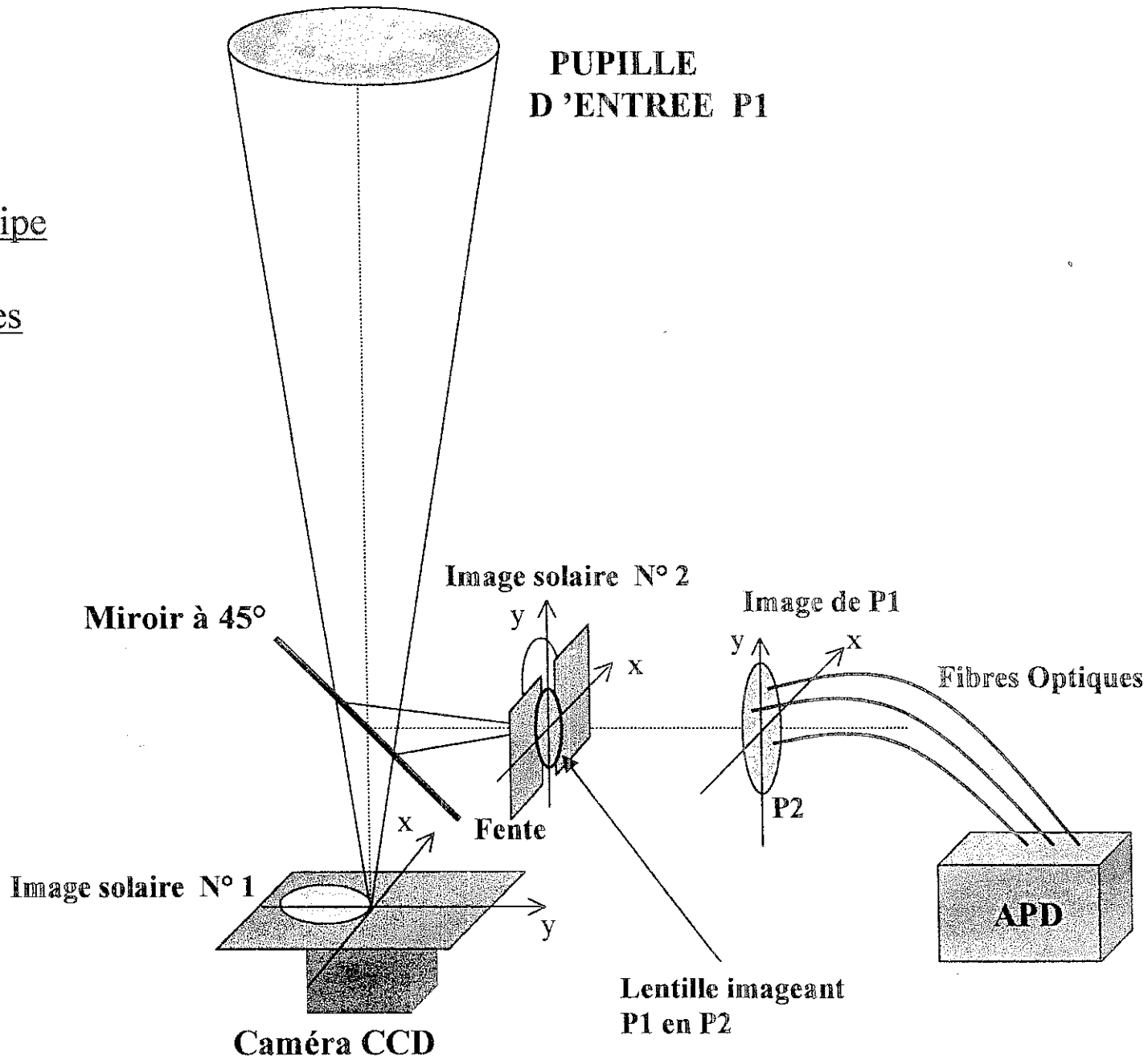
V - LES DONNEES : ACQUISITION - TRAITEMENT - STOCKAGE

Sur la voie CCD (estimation des paramètres de cohérence spatioangulaire et des profils de turbulence), **le temps d'exposition devra être inférieur à 5ms et le pas d'échantillonnage égal à 20ms.**

Sur la voie "observation dans le plan pupille" (capteurs individuels : photodiodes) (estimation du temps de cohérence), **ce pas d'échantillonnage devra être inférieur ou égal à 5ms.**

Estimation des paramètres de cohérence spatioangulaire

Schéma de principe
du moniteur
d 'images solaires
(MISOLFA)



J.Borgnino, A.Irbah et
F.Martin (Février 2000)

On rappelle qu'il s'agit du paramètre de Fried r_0, de l'échelle externe de cohérence spatiale L_0 et de la taille du domaine d'isoplanétisme θ_0 (défini ici au sens des angles d'arrivée).

Pour estimer ces paramètres, on va calculer expérimentalement la covariance angulaire des fluctuations d'angle d'arrivée à laquelle on ajustera la covariance théorique calculée en utilisant le modèle de Von Karman.

Cette covariance théorique peut se déduire aisément de l'expression donnée pour la covariance spatiale dans le paragraphe III. Il suffit de remplacer la variable spatiale par $\underline{\rho}$ par $\underline{\theta}h$.

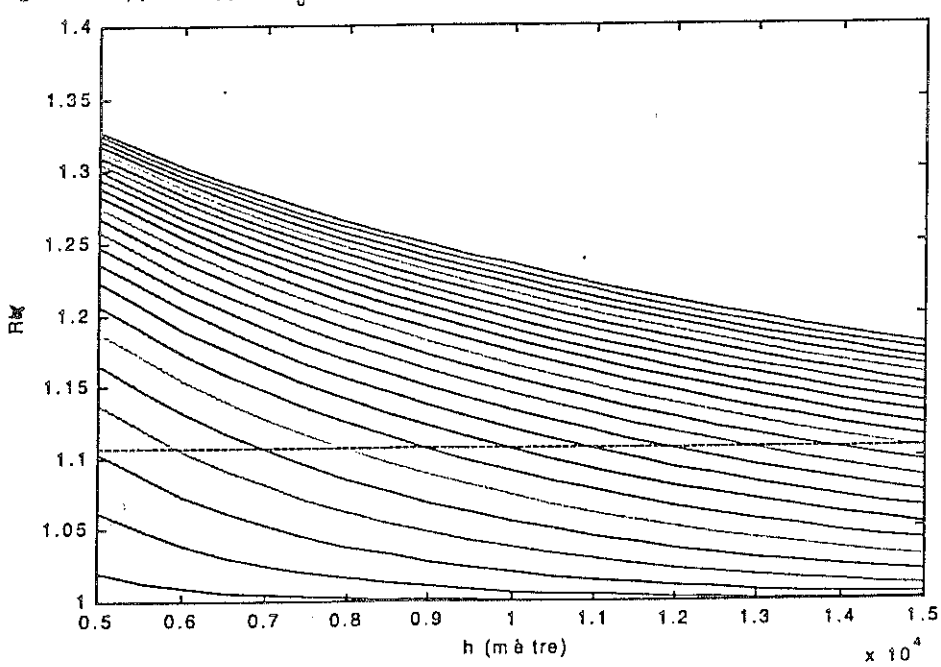
On se place ici dans le cas où l'atmosphère terrestre est assimilée à une seule couche turbulente équivalente et dans celui de l'observation des fluctuations du bord solaire (covariance transverse). On obtient alors l'expression suivante qui est fonction des paramètres r_0, L_0 et h (altitude de la couche équivalente) :

$$C_{a,\alpha}(\theta) = 0.0716\lambda^2 r_0^{-5/3} \int_0^{+\infty} df.f^3 \left(f^2 + \frac{1}{L_0^2} \right)^{-11/6} \left[J_0(2\pi f\theta h) + J_2(2\pi f\theta h) \right] \left[\frac{2J_1(\pi Df)}{\pi Df} \right]^2$$

On est donc conduit à un ajustement portant sur ces 3 paramètres. Pour obtenir ces estimations sans temps de calcul prohibitif, il est proposé la procédure suivante :

- on calcule tout d'abord l'intégrale de la covariance angulaire pour 2 valeurs θ_1 et θ_2, ce qui conduit à $I_\alpha(\theta_1)$ et $I_\alpha(\theta_2)$. Le rapport $R_\alpha = I_\alpha(\theta_1) / I_\alpha(\theta_2)$ n'est plus fonction de r_0 . On le représente ci-dessous en fonction de h pour différentes valeurs de L_0 .

Fig 4 : Rapport R_α pour L_0 variant de 0.3 à 4.9 m par pas de 0.2 m (de bas en haut)



Lorsque l'on porte R_α correspondant à l'observation, on sélectionne un certain nombre de couples (h , L_0) qui peuvent convenir vis-à-vis des valeurs expérimentales.

- On utilise ensuite $I_\alpha(\theta_1)$. Cette intégrale est représentée ci-dessous en fonction du paramètre de Fried r_0 pour les différents couples (h , L_0) sélectionnés précédemment.

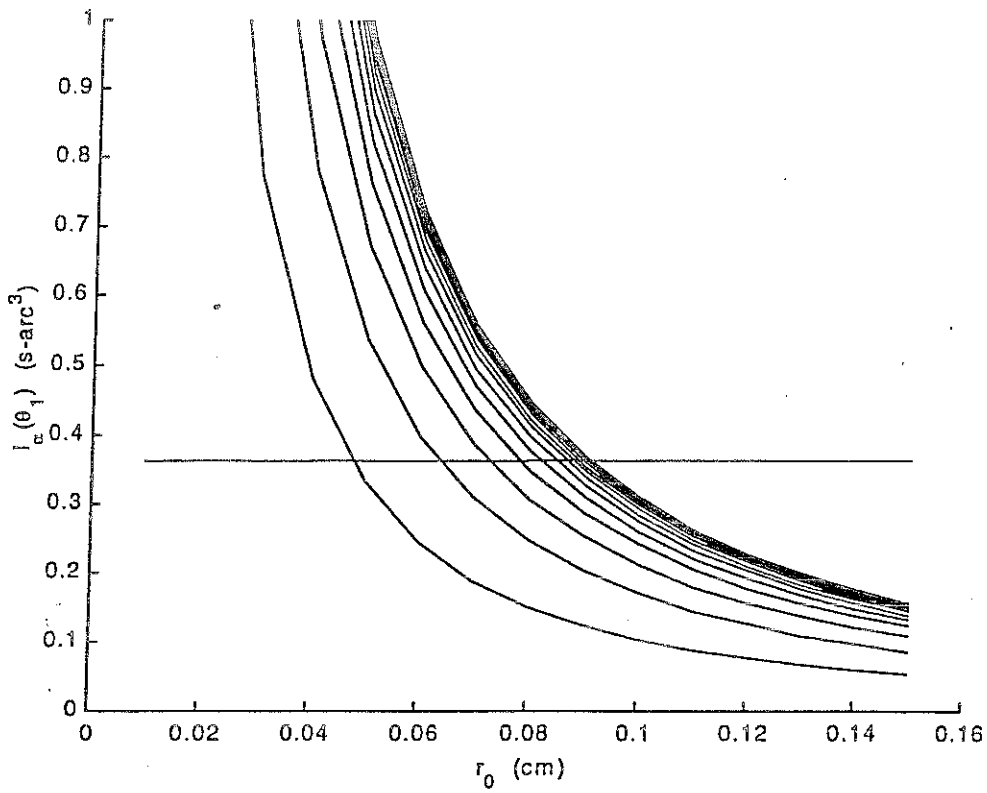


Fig. 2 : Evolution de $I_\alpha(\theta_1)$ en fonction de r_0 pour chaque couple potentiel (h,L_0).
De bas en haut, les courbes correspondent aux couples de la fig. 1 pris de gauche à droite (h croissant).
Elles sont calculées pour une intégration angulaire égale à 6.7 s-arc.

Lorsque l'on porte $I_\alpha(\theta_1)$ correspondant à l'observation, on constate que l'on constitue des triplets (r_0, h, L_0). Il suffit alors de choisir le triplet qui minimise l'écart entre les données expérimentales et l'expression théorique. La taille du domaine d'isoplanétisme θ_0 est déduite en effectuant le rapport r_0/h.

Estimation du paramètre de cohérence temporelle τ_0

Le temps de décorrélation τ_0 peut être défini comme le temps pour lequel la covariance temporelle $C_{t,\alpha}(\tau)$ a chuté d'un facteur k par rapport à sa valeur pour $\tau = 0$. De manière identique à ce qui à était fait pour déduire la covariance angulaire de la covariance spatiale, il suffit de remplacer la base ρ par $v\tau$ pour obtenir la covariance temporelle. Pour pouvoir effectuer cette transformation, il faut se placer dans le cadre de l'hypothèse de la turbulence figée (dite hypothèse de Taylor). La vitesse v est la composante suivant la base du vecteur vitesse équivalent (du point de vue des effets temporels) à l'ensemble des vecteurs vitesses des couches turbulentes. L'utilisation de la Transformation de Mellin permet de mettre cette covariance sous la forme de séries convergentes qui conduisent à d'excellentes approximations avec un nombre de termes petit. Le temps de décorrélation peut ensuite se calculer simplement. La procédure détaillée est décrite dans l'article signé R. Conan et al. qui doit paraître prochainement dans J.O.S.A. (voir la bibliographie).

Estimation par inversion des profils $C_n^2(h)$

La covariance angulaire donnée ci-dessus pour le front d'onde en fonction de r_0, L_0 et h (altitude équivalente) peut également être écrite en fonction du profil vertical d'énergie turbulente $C_n^2(h)$. On obtient alors :

$$C_{a,\alpha}(\theta)=1.19\int_0^{+\infty} dh.C_n^{\,2}(h)\int_0^{+\infty} df.f^3\left(f^2+\frac{1}{L_0(h)^2}\right)^{-11/6}\left[J_0(2\pi f\theta h)+J_2(2\pi f\theta h)\right]\left[\frac{2J_1(\pi Df)}{\pi Df}\right]^2$$

On remarquera que l'échelle externe de cohérence spatiale apparaît maintenant comme une fonction de h. Dans une première étape, on supposera que cette échelle varie peu avec l'altitude et qu'on peut la considérer comme constante, égale à L_0 déduite de l'analyse du front d'onde résultant. L'estimation du profil vertical d'énergie turbulente $C_n^2(h)$ passe par l'inversion de la forme intégrale donnée ci-dessus (ou de l'expression équivalente obtenue pour la fonction de structure). Le problème inverse est linéaire en C_n^2 mais est mal conditionné comme le montre la décomposition en valeurs singulières. Pour obtenir une solution stable , on peut utiliser une méthode de régularisation dite de Marquardt-Levenberg (voir dans les annexes la référence 6). La méthode a été validée par application sur des données synthétiques puis des données réelles ont été traitées.

Procédure de prétraitement des données :

Nettoyage des images : Pour obtenir une bonne estimation des fluctuations d'angle d'arrivée (perturbations présentées par l'image du bord solaire observée au foyer de l'instrument), il est nécessaire de nettoyer les images de tous les défauts (taches, défauts de nature instrumentale.....). Une méthode a été proposée, basée sur la transformation en ondelettes, permettant une correction des images sans perte de résolution. Cette correction est effectuée sur les détails issus de la décomposition. Une procédure itérative est appliquée jusqu'à ce que les taches soient ramenées au niveau du bruit. La méthode a été appliquée sur des données synthétiques puis sur des données réelles obtenues à l'astrolabe du plateau de Calern. Les résultats obtenus sont présentés dans l'article signé A. Irbah et al. (voir dans la bibliographie : Solar Physics, 185, 255-273, 1999).

Correction du bruit de photons : Pour éliminer ce bruit on calcule la covariance en passant par la densité spectrale des fluctuations. C'est sur cette densité spectrale que s'effectuera le filtrage du bruit. C'est une procédure qui est décrite dans l'article 5 donné dans les annexes. Le niveau du bruit est simplement estimé au-delà de la fréquence de coupure du télescope, puis soustrait avant que soit effectuée la transformation de Fourier inverse qui conduit à la covariance.

Cadence d'acquisition des données

Une estimation des paramètres sera obtenue toutes les 4 minutes, avec un temps d'intégration de 2 minutes. Il n'y aura pas de repointage dû au guidage durant la mesure. Il faudra donc 2 ordinateurs configurés en réseau, l'un étant dédié à la gestion de l'expérience et à l'acquisition des données, l'autre permettant le prétraitement et le traitement des données ainsi que la gestion de la base de données.

VI - LA MESURE DU DIAMETRE SOLAIRE A L'ASTROLABE ET L'ERREUR DUE AUX EFFETS ATMOSPHERIQUES

L'étude de cette erreur a été effectuée récemment en simulation numérique. Les résultats sont présentés dans l'article référencé 7 dans les annexes. La simulation numérique des observations à l'astrolabe a été réalisée pour diverses conditions de turbulence. Dans un premier temps, on a ainsi obtenu des images du Soleil telles qu'elles apparaissent à travers l'atmosphère terrestre. Dans une seconde étape, les trajectoires des images directe et réfléchie ont été déduites comme dans l'expérience réelle de mesure du diamètre à l'astrolabe. Le point d'intersection des trajectoires, correspondant à l'instant de transit du Soleil par le petit cercle de hauteur a pu être déterminé en association avec les conditions d'observation définies par le paramètre de Fried r_0 , l'échelle externe de cohérence spatiale L_0 et le rapport entre le temps d'exposition et le temps d'évolution caractéristique des phénomènes turbulents. L'étude de l'erreur a été centrée sur l'analyse du comportement de ce temps de transit avec les conditions d'observation. La valeur de cette erreur diminue lorsque la qualité des images augmente et ce d'autant plus que le temps d'exposition est petit. Par contre, elle augmente avec la valeur de l'échelle externe de cohérence

spatiale. Le paramètre le plus influent sur la qualité des mesures semble être le temps d'exposition vis-à-vis du temps d'évolution caractéristique.

VII - DISCUSSION - PERSPECTIVES

Ce document est une première ébauche, encore largement imparfaite, qui devrait cependant permettre de démarrer la discussion et l'analyse critique, dont les éléments seront intégrés dans une version ultérieure.

Le concept expérimental retenu devrait permettre d'estimer l'ensemble des paramètres associés aux fronts d'onde dans le cadre d'un modèle de turbulence, de proposer éventuellement une autre modélisation plus réaliste, de retrouver ainsi la fonction de transfert atmosphérique (ou la réponse impulsionnelle) à long temps de pose. L'observation des fluctuations d'angle d'arrivée simultanément dans les plans image et pupille conduit à une information complète sur l'état de cohérence des fronts d'onde ainsi que sur la localisation de la turbulence atmosphérique via les variances, les covariances (ou les fonctions de structure). L'intercalibration des 2 voies de l'expérience devrait rendre plus robuste l'estimation.

Dans la prochaine période, il sera nécessaire :

- d'affiner les choix expérimentaux
- de réaliser une simulation numérique complète de l'expérience. Un chercheur de l'observatoire d'Alger arrive dans environ 1 mois pour une durée de 3 mois pour mener à bien ce travail. Il existe déjà une simulation des observations effectuées à l'astrolabe sur laquelle il va pouvoir s'appuyer. Il va falloir augmenter la qualité et la puissance du matériel informatique que l'on mettra à sa disposition.
- de classer et de préciser l'ensemble des études théoriques. Un document spécifique devrait être produit. Il faudra sans doute prévoir plusieurs niveaux de réduction des données.
- de prévoir une organisation cohérente de la base de données qui va se constituer. Ceci va devoir se faire en liaison avec la définition et l'architecture des bases de données PICARD-SOL et PICARD-ESPACE de façon à définir une stratégie optimale pour la comparaison des données sol et espace, prenant en compte les effets atmosphériques.

.....

VIII - BIBLIOGRAPHIE : Estimation des paramètres qualifiant les images astronomiques, modélisation, effets sur les observations à Haute Résolution Angulaire.

A - Références relatives à G.S.M. (Generalized Seeing Monitor)

- AVILA (R.), ZIAD (A.), BORGNINO (J.), MARTIN (F.), AGABI (A.), TOKOVININ (A.), (1997) Theoretical spatio-temporal analysis of angle of arrival induced by atmospheric turbulence as observed with the Grating Scale Monitor. ***J. Opt. Soc. Am. A***, **14**, 3070-3082.

- CONAN (R.), BORGNINO (J.), ZIAD (A.), MARTIN (F.), (2000) Analytical solution for the covariance and for the coherence time of the angle of arrival of a wave front corrugated by atmospheric turbulence. A paraître dans ***J. Opt. Soc. Am.***.

- MARTIN (F.), TOKOVININ (A.), ZIAD (A.), CONAN (R.), BORGNINO (J.), AVILA (R.), AGABI (A.), SARAZIN (M.), (1998) First statistical data on wavefront outer scale at La Silla observatory from the G.S.M. instrument. ***Astron. Astrophys.***, **336**, L49-52.

- MARTIN (F.), CONAN (R.), TOKOVININ (A.), ZIAD (A.), TRINQUET (H.), BORGNINO (J.), AGABI (A.), SARAZIN (M.), (2000) Optical parameters relevant for HIGH Angular

resolution at Paranal from GSM instrument and surface layer contribution. A paraître dans *Astron. Astrophys. Supplement Series.*

B - **Références relatives à l'observation plan-pupille**

- BORGNINO (J.), (1978) Etude de la dégradation des images astronomiques diurnes par analyse statistique des fluctuations d'angle d'arrivée. ***Thèse de Doctorat d'Etat*** (ès Sciences Physiques), Université de Nice - Sophia Antipolis.

- BORGNINO (J.), MARTIN (F.), (1977) Analyse statistique des déformations aléatoires d'une surface d'onde dues à la turbulence atmosphérique au voisinage du sol. I - Exposé de la méthode - Premiers résultats. ***J. of Optics (Paris),*** **8**, 319-326.

- BORGNINO (J.), VERNIN (J.), (1978) Experimental verification of the inertial model of atmospheric turbulence from solar limb motion. ***J. Opt. Soc. Am.***, **68**, 1056-1062.

- BORGNINO (J.), RICORT (G.), CEPPATELLI (G.), RIGHINI (A.), (1982) Lower Atmosphere and Solar Seeing : an experiment of simultaneous measurements of nearby turbulence by thermal radiosondes, by angle-of-arrival statistics and image motion observation. ***Astron. Astrophys.,*** **107**, 333-337.

C - **Références relatives à l'observation plan-image**

- DRUESNE (P.), BORGNINO (J.), AIME (C.), PETROV (R.G.), KADIRI (S.), (1983) Etude spatio-temporelle de la réponse impulsionnelle de l'atmosphère terrestre par observation du bord solaire. ***J. of Optics (Paris),*** **14**, 11-17.

- IRBAH (A.), (1986) Mesure des paramètres atmosphériques qualifiant les images en Astronomie solaire. ***Thèse de Doctorat de 3^{ième} Cycle.*** Université de Nice - Sophia Antipolis.

- IRBAH (A.), BORGNINO (J.), LACLARE (F.), MERLIN (G.), (1993) Isoplanatism and High Spatial Resolution solar imaging. ***Astron. Astrophys.***, **276**, 663-672.

- BOUZID (A.), IRBAH (A.), BORGNINO (J.), LANTERI (H.), (1999) Atmospheric turbulence profile estimation from fluctuation analysis of extended object images. ***14^{ième} Symposium ESA.*** "Models, simulation and laboratory studies". Postdam - Germany. 31 May-3 June 1999.

D - **Références relatives au traitement des données de l'astrolabe**

- IRBAH (A.), BORGNINO (J.), LACLARE (F.), MERLIN (G.), (1994) Solar diameter measurements with Calern Observatory astrolabe and atmospheric turbulence effects. ***Solar Physics***, **149**, 213-230.

- IRBAH (A.), BOUZARIA (M.), LAKHAL (L.), MOUSSAOUI (R.), BORGNINO (J.), LACLARE (F.), DELMAS (C.), (1999) Feature extraction from solar images using wavelet transform : image cleaning for applications to solar astrolabe experiment. ***Solar Physics***, **185**, 255-273.

- LAKHAL (L.), IRBAH (A.), BOUZARIA (M.), BORGNINO (J.), LACLARE (F.), DELMAS (C.), (1999) Error due to atmospheric turbulence effects on solar diameter measurements performed with the astrolabe. ***Astron. Astrophys. Supplements Series***, **138**, 155-162.

-=-=-=-=-=-=-=-=-=-=-=-=-=-=-=-=-=-=-

IX - ANNEXES

1 AVILA (R.), ZIAD (A.), BORGNINO (J.), MARTIN (F.), AGABI (A.), TOKOVININ (A.), (1997) Theoretical spatio-temporal analysis of angle of arrival induced by atmospheric turbulence as observed with the Grating Scale Monitor. ***J. Opt. Soc. Am. A***, **14**, 3070-3082.

2 MARTIN (F.), CONAN (R.), TOKOVININ (A.), ZIAD (A.), TRINQUET (H.), BORGNINO (J.), AGABI (A.), SARAZIN (M.), (2000) Optical parameters relevant for HIGH Angular resolution at Paranal from GSM instrument and surface layer contribution. A paraître dans ***Astron. Astrophys. Supplement Series.***

3 BORGNINO (J.), MARTIN (F.), (1977) Analyse statistique des déformations aléatoires d'une surface d'onde dues à la turbulence atmosphérique au voisinage du sol. I - Exposé de la méthode - Premiers résultats. ***J. of Optics (Paris),*** **8**, 319-326.

4 BORGNINO (J.), VERNIN (J.), (1978) Experimental verification of the inertial model of atmospheric turbulence from solar limb motion. ***J. Opt. Soc. Am.***, **68**, 1056-1062.

5 IRBAH (A.), BORGNINO (J.), LACLARE (F.), MERLIN (G.), (1993) Isoplanatism and High Spatial Resolution solar imaging. ***Astron. Astrophys.***, **276,** 663-672.

6 BOUZID (A.), IRBAH (A.), BORGNINO (J.), LANTERI (H.), (1999) Atmospheric turbulence profile estimation from fluctuation analysis of extended object images. ***14^{ième} Symposium ESA.*** "Models, simulation and laboratory studies". Postdam - Germany. 31 May-3 June 1999.

7 LAKHAL (L.), IRBAH (A.), BOUZARIA (M.), BORGNINO (J.), LACLARE (F.), DELMAS (C.), (1999) Error due to atmospheric turbulence effects on solar diameter measurements performed with the astrolabe. ***Astron. Astrophys. Supplements Series***, **138,** 155-162.

-=-

Theoretical spatiotemporal analysis of angle of arrival induced by atmospheric turbulence as observed with the grating scale monitor experiment

Remy Avila, Aziz Ziad, Julien Borgnino, François Martin, and Abdelkrim Agabi

Unité Mixte de Recherche 6525 Astrophysique, Université de Nice–Sophia Antipolis, Centre National de la Recherche Scientifique, Parc Valrose, 06108 Nice Cedex 2, France

Andrey Tokovinin

Sternberg Astronomical Institute, Universitetsky Prospelet 13, 119899 Moscow, Russia

Received November 20, 1996; revised May 15, 1997; accepted May 16, 1997

Theoretical investigations of the statistical properties of the wave front perturbed by atmospheric turbulence are presented. They are deduced from the calculation of the two-dimensional spatial covariance and the temporal cross spectrum of the angle-of-arrival fluctuations with a finite outer scale over a pair of circular pupils as in the case of the grating scale monitor or any other Shack–Hartmann-type sensor. Both calculations lead to integral expressions that are numerically evaluated and hold for any baseline vector in the mean wave-front plane. It is proposed to retrieve the wave-front outer scale $\mathscr{L}_0$ from estimations of this two-dimensional spatial covariance, normalized by the angle-of-arrival structure function. To eliminate instrument vibration errors, the covariance and the structure function are estimated from measurements obtained by mechanically independent and mechanically coupled devices, respectively. The angle-of-arrival temporal cross spectrum is calculated for any mean wind velocity vector. It is shown that the baseline component in the mean wind direction affects the phase of the angle-of-arrival temporal cross spectrum, whereas the component in the perpendicular direction affects the modulus. From simultaneous measurements of the phase of the angle-of-arrival temporal cross spectrum obtained with two nonparallel baselines, one can calculate the mean wind speed and direction, which allows estimation of the coherence time for techniques of optical observation at high angular resolution through the atmosphere. © 1997 Optical Society of America [S0740-3232(97)01211-8]

1. INTRODUCTION

The size of an astronomical long-exposure image depends on a single turbulence parameter, the Fried parameter r_0. However, high-angular-resolution techniques in the optical and infrared domains, namely, stellar interferometry and adaptive optics, require a better understanding of the optical effects of the atmospheric turbulence. Their performances depend on spatiotemporal and spatioangular coherence properties of the resultant wave front on the ground. With the development of long-baseline interferometry and the increase of telescope diameters, evidence of departure from standard Kolmogorov theory for long baselines has been collected.

One of the most important effects that appears when going to long baselines is that related to the spatial coherence outer scale $\mathscr{L}_0$ (Ref. 1) of the wave front reaching the telescope(s) (also called the wave-front outer scale). At distances r comparable with $\mathscr{L}_0$, the spatial structure function of the phase fluctuations no longer increases as $r^{5/3}$ but begins to saturate. $\mathscr{L}_0$ can be interpreted as some weighted mean of the local optical turbulence outer scale $L_0(h)$, the weighting factor being the refractive index structure constant profile $C_n^2(h)$.[1] *In situ* measurements[2,3] have given very small local outer scales [$L_0(h) \leqslant 5$ m for $h \geqslant 2$ km], which agrees with the repeatedly confirmed thin optical turbulence layers[4–8] and their recently proposed formation mechanism.[8] The wave-front outer scale $\mathscr{L}_0$ has also been estimated directly on the ground. Table 1 summarizes the available measurements, which can be divided into four categories: integrated outer scales from *in situ* soundings, interferometric techniques, Shack–Hartmann-type techniques with a single telescope, and Shack–Hartmann-type techniques with multiple telescopes. As can be seen, the reported values of $\mathscr{L}_0$ are somewhat controversial. They will be discussed further in Section 5.

We give here a nonexhaustive list of consequences of a few-meter outer scale model, compared with those of an infinite outer scale model, for long-baseline interferometry and adaptive optics: Buscher *et al.*[15] mentioned that the uncertainty in the white-light fringe position would very much decrease, making blind-pointed observations practicable in long-baseline interferometry, and that its astrometric capabilities would be improved because the major error comes from the fringe position offset caused by the low-spatial-frequency phase perturbations that would be reduced. The spectral bandwidth and the exposure time for both techniques would be widened.[24,25] As for the spatial modal expansion of the perturbed wave front, a lower proportion of energy would be concentrated

0740-3232/97/113070-13$10.00 © 1997 Optical Society of America

Table 1. Reported Measurements of the Wave-Front Outer Scale $\mathscr{L}_0$

Measurement	Instrument/Telescope[b]	$\mathscr{L}_0$ (m)[a]	Reference
In situ soundings			
Refractive index structure function	Balloons (Paranal, Chile)	2.5	Fuchs[9]
Interferometry			
Phase structure	I2T (Calern, France)	~8	Mariotti and Di Benedetto[10]
function (Ph.S.F.)	Sydney University Stellar Interferometer (Australia)	5–10	Davis *et al.*[11]
Ph.S.F. + phase temporal	Mounted on WHT (Canary Islands)	$\sim 2 \times 2\pi$	Nightingale and Buscher[12]
power spectrum (Ph.T.P.S.)	WHT + COAST (Cambridge, UK)	∞	Haniff *et al.*[13]
Ph.T.P.S., single baseline	Mark III (Mt. Wilson, U.S.)	>2000	Colavita *et al.*[14]
Ph.T.P.S.	Mark III (Mt. Wilson)	~30	Buscher *et al.*[15]
with different baselines	Mark III (Mt. Wilson)	~30	Buscher *et al.*[16]
	ISI (Mt. Wilson)	5–20	Bester *et al.*[17]
Spectral decorrelatiion	GI2T (Calern)	~22	Berio *et al.*[18]
Shack–Hartmann-type technique with a single telescope			
AA structure function	Canada–France–Hawaii (Hawaii)	5–8	Tallon[19]
Zernike variances	3.6-m European Southern Observatory (La Silla, Chile)	~50	Rigaut *et al.*[20]
AA variances	OHP (Provence, France)	5–100	Ziad *et al.*[21]
Tilt covariances	Keck (U.S.)	16–80	Takato and Yamaguchi[22]
Shack–Hartmann-type technique with multiple telescopes			
AA covariance	GSM (Calern)	10–300	Agabi *et al.*[23]

[a] Nightingale and Buscher[12] used a definition of the outer scale that differs from that used in this paper [Eq. (7)] by a factor of 2π. All other $\mathscr{L}_0$ values are consistent with the definition used here.

[b] I2T, Interférométre à 2 Telescopes; WHT, William Herschel Telescope; COAST, Cambridge Optical Aperture Synthesis Telescope; ISI, Infrared Spatial Interferometer; GI2T, Grand Interférométre à 2 Telescopes; OHP, Observatoire de Haute Provence.

in the low-order Zernike components of the wave front,[26–28] which would affect the design of adaptive optics systems.

The temporal behavior of the wave front governs the temporal parameters in high-angular-resolution techniques, e.g., the exposure time in speckle and long-baseline interferometry, limiting the magnitude of reference sources, and the temporal bandwidth of compensating systems in adaptive optics. Several authors have studied the temporal characteristics of the wave front. Roddier *et al.*[29] proposed a theoretical formulation of the speckle lifetime that is due to dispersion of wind velocities in multiple turbulent layers. Roddier and Lena[30] extended this work to long-baseline interferometry. Aime *et al.*[31] noticed that the speckle temporal behavior is governed mostly by image motion. Ziad[25] studied the evolution of the signal-to-noise ratio in high-angular-resolution techniques as a function of the exposure time. As mentioned above, many authors[12–17] have measured the temporal phase power spectrum by interferometric techniques. The development of adaptive optics systems has encouraged many studies of the temporal power spectra of the turbulence-induced Zernike aberrations. Roddier *et al.*[32] calculated theoretically those spectra and presented some measurements. Conan *et al.*[33] published similar theoretical calculations for any wind speed direction and presented some data.[34,35] Voitsekhovich and Cuevas[27] studied the effect of a finite outer scale on the temporal power spectrum of image centroid motion and Zernike coefficients. Martin[36] investigated the influence of the exposure time in the angle-of-arrival (AA) variance and structure function measurements. Lopez[37] studied the statistical properties of the AA velocity. Finally, Martin *et al.*[38] presented an example of experimental AA power spectra. Every model concerning the wave-front temporal behavior is based on the Taylor hypothesis. Some of them include several turbulent layers, and some do not. A brief discussion of those aspects is presented in Section 5.

In response to the need for systematic measurements of the optical effects of the atmospheric turbulence at long baselines, a new version of the grating scale monitor (GSM)[23,38] is being developed. It consists of a Shack–Hartmann-type technique based on independent synchronized modules allowing the measurement of the AA fluctuations, in a given direction on the sky, with 10-cm-diameter pupils placed at four points on the wave front and with baselines varying from 14 cm to several tens of meters in any direction. The spatial wave-front parameters r_0 and $\mathscr{L}_0$ are derived from, respectively, the spatial structure function and the spatial covariances of the AA fluctuations measured with several pairs of modules. As for the temporal characteristics, we propose to compute their temporal cross spectrum (TCS). The advantage of calculating the TCS, instead of simply the temporal power spectrum, is that the TCS contains spatiotemporal

information. Hence one can obtain from the TCS both temporal and spatial characteristics, as well as the mean propagation velocity vector of the wave front, as will be shown in this paper. Such data analysis has to be compared with the corresponding theoretical models. The previous version of the GSM used only α UMi (Polaris) as a light source without tracking, whereas the new version, equipped with equatorial mounts, can observe any star, so that it can be installed anywhere in the world. This implies that all the theoretical results concerned have to be extended for any baseline direction.

In this paper we present the theoretical calculation and analysis of the AA two-dimensional (2-D) spatial covariance (in Section 2) and the AA TCS (in Section 4), valid for any pair of circular pupils of any Shack–Hartmann-type AA sensor. Both results take into account a finite outer scale and apply to any baseline in the wave-front plane. The AA TCS holds for any mean wind direction, under the frozen turbulence hypothesis. Applications for retrieving the parameters of interest are discussed in Section 5, as well as some more general aspects mentioned above.

2. TWO-DIMENSIONAL SPATIAL COVARIANCE OF THE ANGLE-OF-ARRIVAL FLUCTUATIONS

The theoretical AA covariance is currently expressed for the particular cases in which the baselines between the two pupils are either parallel (longitudinal covariance) or perpendicular (transverse or lateral covariance) to the direction of the observed fluctuations.[23,39,40] To interpret experimental results obtained when observing any star, it is necessary to calculate the 2-D covariance for any baseline direction, which can vary with time. Figure 1 gives the most general situation and presents the notations used (the velocity vector in that figure is not of any interest in this section; it concerns Section 4). Let $\alpha(\mathbf{r}, t)$ and $\alpha(\mathbf{r} + \mathbf{B}, t)$ be the AA fluctuations, with respect to the mean AA, measured along an arbitrary x direction, at time t, averaged over circular pupils P_1 and P_2 of the same diameter D centered at positions $\mathbf{r}$ and $\mathbf{r} + \mathbf{B}$, respectively. In Fig. 1 $\mathbf{r}$ is chosen null without any loss of generality, as the covariance does not depend on r, assuming that α obeys a homogeneous random process.

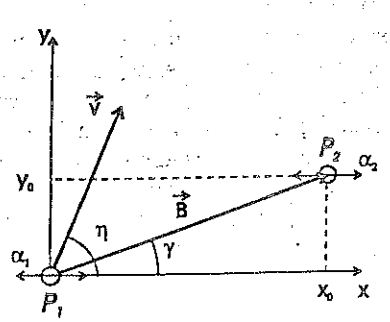


Fig. 1. General configuration for the calculation of the angle-of-arrival (AA) two-dimensional (2-D) covariance and temporal cross spectrum (TCS). α_1 and α_2 represent the AA fluctuations along the x direction, measured at pupils P_1 and P_2, respectively. The baseline between both pupils has coordinates (x_0, y_0) in the Cartesian system (x, y) and polar coordinates (B, γ). The mean wind velocity with polar coordinates (v, η) is also represented.

A. General Expression

The 2-D AA covariance may be obtained from the Fourier transform of the AA power spectrum. If λ is the wavelength and $W_\phi(f_x, f_y)$ is the power spectrum of the phase fluctuations ϕ, one can write this covariance as[40]

$$C_\alpha(x_0, y_0) = \lambda^2 \int_{-\infty}^{+\infty} \int_{-\infty}^{+\infty} df_x df_y \, f_x^2 W_\phi(f_x, f_y) \times \exp[2i\pi(x_0 f_x + y_0 f_y)], \quad (1)$$

where f_x and f_y are spatial frequencies corresponding, respectively, to the direction of fluctuation x of the AA α and the perpendicular direction y. Changing the integration variables (f_x, f_y) into polar coordinates (f, θ) leads, at first, to

$$C_\alpha(x_0, y_0) = \lambda^2 \int_0^{+\infty} df \, f^3 W_\phi(f) I(x_0, y_0, f), \quad (2)$$

where

$$I(x_0, y_0, f) = \int_0^{2\pi} d\theta \cos^2\theta \times \exp[2i\pi f(x_0 \cos\theta + y_0 \sin\theta)], \quad (3)$$

and then, by using (as shown in Fig. 1) $x_0 = B\cos\gamma$ and $y_0 = B\sin\gamma$, to

$$I(x_0, y_0, f) \doteq \mathcal{I}(B, \gamma, f) = \int_0^{2\pi} d\theta \cos^2\theta \exp[2i\pi f B \cos(\theta - \gamma)]. \quad (4)$$

The definition of Bessel functions of the first kind allows us to rewrite this expression as

$$\mathcal{I}(B, \gamma, f) = \pi[J_0(2\pi f B) - \cos(2\gamma) J_2(2\pi f B)], \quad (5)$$

and Eq. (2) becomes

$$C_\alpha(x_0, y_0) = \mathcal{C}_\alpha(B, \gamma) = \pi\lambda^2 \int_0^{+\infty} df \, f^3 W_\phi(f) \times [J_0(2\pi f B) - \cos(2\gamma) J_2(2\pi f B)]. \quad (6)$$

In the framework of the so-called von Kármán model, the phase power spectrum is given by

$$W_\phi(f) = 0.0228 r_0^{-5/3} (f^2 + 1/\mathscr{L}_0^2)^{-11/6}, \quad (7)$$

where r_0 is the Fried parameter, $\mathscr{L}_0$ is the wave-front outer scale, and the wave-front inner scale l_0 is assumed to be equal to 0. Introducing expression (7) into Eq. (6), taking into account the spatial filtering performed by the pupils, and making explicit the dependence on $\mathscr{L}_0$ and D, we can write the 2-D AA covariance as

$$\mathscr{C}_a(B,\ \gamma,\ D,\ \mathscr{L}_0) = 0.0716\lambda^2 r_0^{-5/3} \times \int_0^{+\infty} df\, f^3 \left(f^2 + \frac{1}{\mathscr{L}_0^2}\right)^{-11/6} \times [J_0(2\pi fB) - \cos(2\gamma) J_2(2\pi fB)] \times \left[2\frac{J_1(\pi Df)}{\pi Df}\right]^2. \quad (8)$$

Substituting X for the dimensionless variable $2\pi fB$ and assuming that $B \neq 0$ lead to

$$\mathscr{C}_a(B,\ \gamma,\ D,\ \mathscr{L}_0) = 0.0388\lambda^2 r_0^{-5/3} B^{-1/3} \times \int_0^{+\infty} dX\, X^3 \left[X^2 + \left(\frac{2\pi B}{\mathscr{L}_0}\right)^2\right]^{-11/6} \times [J_0(X) - \cos(2\gamma) J_2(X)] \times \left[2\frac{J_1\left(\frac{DX}{2B}\right)}{\frac{DX}{2B}}\right]^2. \quad (9)$$

The restriction on B in Eq. (9) is not troublesome, as expression (8) can be used in the case of $B = 0$ to obtain the AA variance.

Figure 2 shows a 2-D plot of the AA 2-D covariance as a function of the baseline vector $(B,\ \gamma)$, obtained from numerical integration of Eq. (8) for $D = 10$ cm, $\mathscr{L}_0 = 10$ m, $\lambda = 0.5\ \mu$m, and $r_0 = 10$ cm. Only baselines with $0° \leq \gamma \leq 180°$ are represented. The missing half of the surface is symmetrical to the plane of equation $\gamma = 0°$. One can notice the smooth transition between longitudinal ($\gamma = 0°$) and transverse ($\gamma = 90°$) covariances.

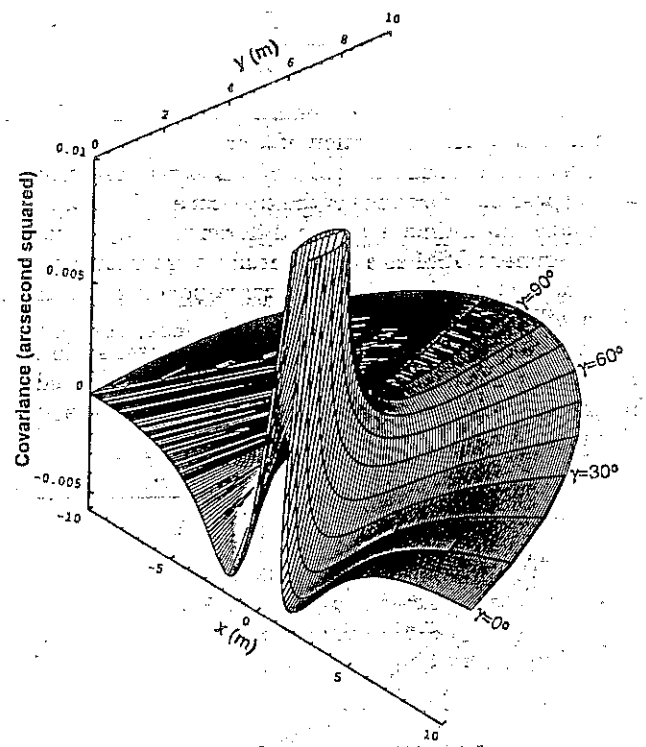


Fig. 2. 2-D plot of the AA covariance as a function of the baseline vector $(B,\ \gamma)$, obtained from numerical integration of Eq. (8) for $D = 10$ cm, $\mathscr{L}_0 = 10$ m, $\lambda = 0.5\ \mu$m, and $r_0 = 10$ cm. The missing half of the surface is symmetrical to the one shown, with respect to the plane of equation $\gamma = 0°$. Covariance values higher than 0.01 arcsec^2 are not represented in order to reduce the dynamic range in the covariance axis, making visible the smooth transition from longitudinal ($\gamma = 0°$) to transverse ($\gamma = 90°$) covariances.

B. Particular Cases

Putting $\gamma = 0$ and $\gamma = \pi/2$, we find again the longitudinal and transverse covariances, respectively, as[40]

$$\mathscr{C}_a\left(B,\ \begin{matrix}\pi/2\\ 0\end{matrix},\ D,\ \mathscr{L}_0\right) = 0.0388\lambda^2 r_0^{-5/3} B^{-1/3} \int_0^{+\infty} dX\, X^3 \left[X^2 + \left(\frac{2\pi B}{\mathscr{L}_0}\right)^2\right]^{-11/6} \times [J_0(X) \pm J_2(X)] \left[2\frac{J_1\left(\frac{DX}{2B}\right)}{\frac{DX}{2B}}\right]^2, \quad (10)$$

where the minus and plus signs correspond to $\gamma = 0$ and $\gamma = \pi/2$, respectively.

C. Distortion Function

Here let us recall that in the framework of the Kolmogorov–Tatarski model the 2-D AA covariance, without any filtering effect taken into account, is[39]

$$C_{K_a}(x_0, y_0) = 0.145\lambda^2 r_0^{-5/3} \left[(x_0^2 + y_0^2)^{-1/6} - \frac{1}{3} x_0^2 (x_0^2 + y_0^2)^{-7/6}\right]. \quad (11)$$

This expression is valid when the spatial shifts are contained between and very far from the limit wave-front scales l_0 and $\mathscr{L}_0$ and when the pupils are assumed to be infinitely small. Passing over to polar coordinates, with the above notations, gives

$$\mathscr{C}_{K_a}(B,\ \gamma) = 0.145\lambda^2 r_0^{-5/3} B^{-1/3} [1 - (\cos^2\ \gamma)/3]. \quad (12)$$

One can define a distortion function H_{VK}, with respect to the Kolmogorov–Tatarski model, as the ratio of Eq. (9) to Eq. (12), which includes filtering effects that are due to the finite wave-front outer scale (for the von Kármán model) and to the finite pupil size. It can be expressed in the form

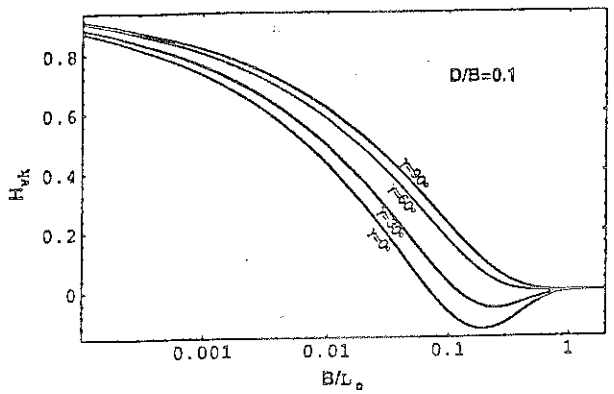


Fig. 3. Distortion function H_{VK}, obtained from numerical integration of Eq. (13) for $D/B = 0.1$ and for different values of the baseline angle γ.

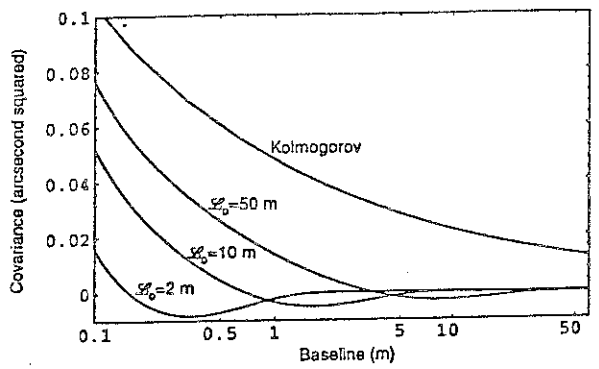


Fig. 4. AA longitudinal covariance ($\gamma = 0°$) obtained from numerical integration of Eq. (10) for $D = 10$ cm and $r_0 = 10$ cm at $\lambda = 0.5\ \mu$m for three values of the wave-front outer scale. The case of Kolmogorov's law is also presented.

$$H_{VK}(B, \gamma, D, \mathscr{L}_0) = \frac{0.0388}{0.145[1 - (\cos^2\gamma)/3]} \times \int_0^{+\infty} dX\, X^3 \left[X^2 + \left(\frac{2\pi B}{\mathscr{L}_0}\right)^2\right]^{-11/6} \times [J_0(X) - \cos(2\gamma) J_2(X)] \times \left[2\frac{J_1\left(\frac{DX}{2B}\right)}{\frac{DX}{2B}}\right]^2. \quad (13)$$

Then, in the general case presented in Fig. 1, the 2-D AA covariance is given by

$$\mathscr{C}_\alpha(B, \gamma, D, \mathscr{L}_0) = \mathscr{C}_{K_\alpha}(B, \gamma) H_{VK}(B, \gamma, D, \mathscr{L}_0). \quad (14)$$

Figure 3 shows, as a function of the dimensionless variable $B/\mathscr{L}_0$, the distortion function $H_{VK}(B, \gamma, D, \mathscr{L}_0)$ for different values of the angle γ between the baseline and the direction of the AA fluctuations observed. Variations of $H_{VK}(B, \gamma, D, \mathscr{L}_0)$ between the extreme values of D/B, 0.01 and 0.2, are less than 1%. The curves are shown for the single value $D/B = 0.1$. Note the behavior of this function as γ passes from 0° (longitudinal fluctuations) up to 90° (transverse fluctuations). For any value of γ, the distortion function reaches 0 when $B/\mathscr{L}_0$ is close to 1. The dependence of longitudinal covariance on the baseline B and the wave-front outer scale $\mathscr{L}_0$ is presented in Fig. 4. The case of an infinite outer scale (Kolmogorov's law) also appears in the figure. There is a strong sensitivity of the covariance to the outer scale for small values of the baseline.

3. NORMALIZED COVARIANCE OF THE ANGLE OF ARRIVAL

From Eq. (8) one can obtain, putting $B = 0$, the expression for the variance of the AA fluctuations along the x axis, $\sigma_\alpha^2(D, \mathscr{L}_0)$. Moreover, the structure function is given by

$$D_\alpha(B, \gamma, D, \mathscr{L}_0) = 2[\sigma_\alpha^2(D, \mathscr{L}_0) - \mathscr{C}_\alpha(B, \gamma, D, \mathscr{L}_0)]. \quad (15)$$

A first way to normalize the 2-D AA covariance is to calculate

$$\Gamma_\alpha' = \frac{\mathscr{C}_\alpha(B, \gamma, D, \mathscr{L}_0)}{\sigma_\alpha^2(D, \mathscr{L}_0)}, \quad (16)$$

which, for a given baseline, remains a function of D and $\mathscr{L}_0$ but is no longer a function of λ or r_0.

However, the variance $\sigma_\alpha^2(D, \mathscr{L}_0)$ is experimentally biased by possible vibrations of the telescope. To avoid this effect, one can estimate r_0 in a differential way by using the experiment GSM as a differential image motion monitor and then recalculating the corresponding variance, which will be thus corrected.

But, for small values of the wave-front outer scale $\mathscr{L}_0$, this effect leads to an overestimation of r_0, as stated by Borgnino *et al.*,[40] and consequently to an underestimation of the calculated values of $\sigma_\alpha^2(D, \mathscr{L}_0)$.

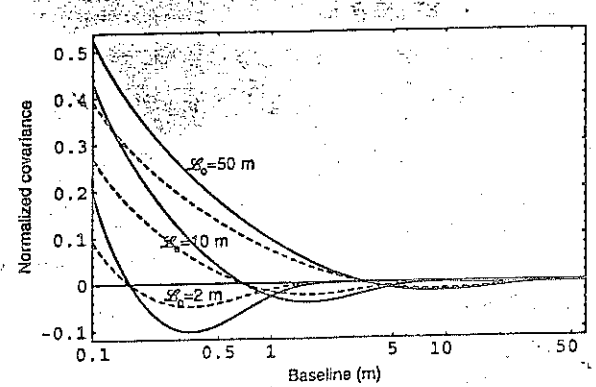


Fig. 5. AA longitudinal covariance normalized by the AA variance (solid curves) and by the AA structure function (dashed curves), calculated by using Eqs. (16) and (17) (with $B_2 = 0.2$ m and $\gamma_2 = 0°$), respectively, for three values of the wave-front outer scale and $D = 10$ cm.

To solve this problem, one can normalize the covariance by the structure function, given by formula (15) and measured for a small baseline (B_2, γ_2) (of the order of a few tens of centimeters). Considering that the covariance $\mathscr{C}_\alpha(B, \gamma, D, \mathscr{L}_0)$ is unaffected by vibration errors, as further discussed in Subsection 5.A, the vibration-free normalized covariance is obtained as

$$\Gamma_\alpha = \frac{\mathscr{C}_\alpha(B, \gamma, D, \mathscr{L}_0)}{D_\alpha(B_2, \gamma_2, D, \mathscr{L}_0)}, \tag{17}$$

from which one can deduce $\mathscr{L}_0$, knowing all other parameters.

Figure 5 shows, for different values of the wave-front outer scale, the longitudinal covariance normalized by the variance (solid curves) and by the structure function (dashed curves). The curves in the first case are slightly more separated than in the second, mainly for small values of the baseline. This can be explained by the fact that the variance is more sensitive to $\mathscr{L}_0$ than the structure function.[21]

4. ANGLE-OF-ARRIVAL TEMPORAL CROSS SPECTRUM

A. General Expression

Let $\alpha_1(t) = \alpha(\mathbf{r}, t)$ and $\alpha_2(t) = \alpha(\mathbf{r} + \mathbf{B}, t)$. Figure 1 represents the general situation, where vector $\mathbf{v}$ is the mean wind velocity. The quantity to be calculated is the cross spectrum of the random processes $\alpha_1(t)$ and $\alpha_2(t)$,

$$W_{\alpha,\mathbf{B}}(\nu) = \langle \hat{\alpha}_1(\nu)\hat{\alpha}_2^*(\nu)\rangle, \tag{18}$$

which may be regarded as an estimation of their statistical similarity at each temporal frequency ν. The caret indicates a Fourier transform, the asterisk denotes a complex conjugate, and angle brackets mean an ensemble average. Throughout this paper $\alpha(\mathbf{r}, t)$ is assumed to be described by a wide-sense stationary and homogeneous random process.

The temporal cross correlation of the AA fluctuations at two positions separated by a baseline $\mathbf{B}$ is

$$\mathscr{C}_{\alpha,\mathbf{B}}(\tau) = \langle \alpha(\mathbf{r}, t)\alpha(\mathbf{r} + \mathbf{B}, t + \tau)\rangle. \tag{19}$$

Assuming that the wave front propagates without deformation, with a velocity $\mathbf{v}$ (Taylor hypothesis in a single turbulent layer), one can write

$$\alpha(\mathbf{r} + \mathbf{B}, t + \tau) = \alpha(\mathbf{r} + \mathbf{B} - \mathbf{v}\tau, t). \tag{20}$$

No particular assumption is made on $\mathbf{v}$. It makes an angle η with the AA measuring direction considered (see Fig. 1). If we substitute Eq. (20) into Eq. (19), the temporal cross correlation reduces to the spatial covariance:

$$\begin{aligned}\mathscr{C}_{\alpha,\mathbf{B}}(\tau) &= \langle \alpha(\mathbf{r}, t)\alpha(\mathbf{r} + \mathbf{B} - \mathbf{v}\tau, t)\rangle \\ &= C_\alpha(\mathbf{v}\tau - \mathbf{B}).\end{aligned} \tag{21}$$

From the Wiener–Khintchin theorem, $W_{\alpha,\mathbf{B}}(\nu)$ and $\mathscr{C}_{\alpha,\mathbf{B}}(\tau)$ form a one-dimensional (1-D) Fourier transform pair. Replacing $\mathscr{C}_{\alpha,\mathbf{B}}(\tau)$ by $C_\alpha(\mathbf{v}\tau - \mathbf{B})$ in the Fourier transform, one can write

$$W_{\alpha,\mathbf{B}}(\nu) = \int_{-\infty}^{+\infty} d\tau\, C_\alpha(\mathbf{v}\tau - \mathbf{B})\exp(2i\pi\nu\tau). \tag{22}$$

The spatial covariance $C_\alpha(\mathbf{r})$ is the 2-D inverse Fourier transform of the spatial AA power spectrum $W_\alpha(\mathbf{f})$, $\mathbf{f}$ being the spatial frequency. Making explicit the Fourier transform, one can write

$$\begin{aligned}W_{\alpha,\mathbf{B}}(\nu) = \int_{-\infty}^{+\infty} d\tau \Bigg\{ \iint_{-\infty}^{+\infty} d\mathbf{f}\, W_\alpha(\mathbf{f}) \\ \times \exp[-2i\pi\mathbf{f}\cdot(\mathbf{v}\tau - \mathbf{B})]\Bigg\}\exp(2i\pi\nu\tau).\end{aligned} \tag{23}$$

Inverting the integration order and rearranging the exponential arguments to isolate the terms that depend on τ, one can identify a delta distribution in the integral over τ, thus obtaining

$$W_{\alpha,\mathbf{B}}(\nu) = \iint_{-\infty}^{+\infty} d\mathbf{f}\, W_\alpha(\mathbf{f})\delta(\nu - \mathbf{v}\cdot\mathbf{f})\exp(2i\pi\mathbf{f}\cdot\mathbf{B}). \tag{24}$$

This is a very expressive equation, analogous to Eq. (22) but now in the spatial-frequency plane. The spatial 2-D power spectrum $W_\alpha(\mathbf{f})$ is cut perpendicularly to this plane along a line of equation $\mathbf{v}\cdot\mathbf{f} = \nu$, and a Fourier transform of the resulting 1-D function is performed. This is exactly the way $W_{\alpha,\mathbf{B}}(\nu)$ is numerically computed.

B. Case of a von Kármán Model

Equation (24) suggests that the calculation will be simplified by rotating the reference system by an angle η in order to have one axis parallel to $\mathbf{v}$ and the other one perpendicular to it. Applying this transformation and simplifying, we obtain

$$\begin{aligned}W_{\alpha,\mathbf{B}}(\nu) = \frac{1}{v}\exp\left[2i\pi B\,\frac{\nu}{v}\cos(\eta - \gamma)\right] \\ \times \int_{-\infty}^{+\infty} dq\; W_\alpha\left(\frac{\nu}{v}\cos\eta - q\sin\eta,\right. \\ \left.\frac{\nu}{v}\sin\eta + q\cos\eta\right)\exp[2i\pi qB\sin(\gamma - \eta)],\end{aligned} \tag{25}$$

where v and B are the moduli of $\mathbf{v}$ and $\mathbf{B}$, respectively, and q represents the spatial frequency along the line where $W_\alpha(\mathbf{f})$ is cut, as explained above. Replacing $W_\alpha(\mathbf{f})$ by its explicit expression in the case of a von Kármán phase power spectrum [Eq. (7)] with the filtering term introduced by the pupils of diameter D, one finally gets

$$W_{\alpha,B}(\nu) = 0.0228\lambda^2 r_0^{-5/3} \frac{1}{v} \exp\left[2i\pi B \frac{\nu}{v} \cos(\eta - \gamma)\right] \times \int_{-\infty}^{+\infty} dq \left(\frac{\nu}{v} \cos\eta - q \sin\eta\right)^2 \times \left[\left(\frac{\nu}{v}\right)^2 + q^2 + \frac{1}{\mathscr{L}_0^2}\right]^{-11/6} \times \left[2\frac{J_1(\pi D[(\nu/v)^2 + q^2]^{1/2})}{\pi D[(\nu/v)^2 + q^2]^{1/2}}\right]^2 \times \exp[2i\pi qB \sin(\gamma - \eta)]. \quad (26)$$

To obtain dimensionless variables and to reduce the number of independent parameters, as in the case of the 2-D AA covariance in Eq. (9), one can redefine the integration variable as $Z = qB$. However, this will not be done, because the analysis of the influence of physical parameters on the TCS is made simpler by using Eq. (26).

C. Numerical Calculation and Physical Analysis

The TCS has been numerically calculated by means of a fast Fourier transform for each value of ν as suggested by Eq. (26). It also shows that $vW_{\alpha,B}(\nu)$ is a function of the ratio ν/v, which reduces the number of independent variables, and indicates that any change in the wind speed translates simply as a shift of the curve of $W_{\alpha,B}(\nu)$ in a log–log plot, without changing its shape. This is why we represent below in Figs. 7–11 modulus [plots (a)] and phase [plots (b)] of $vW_{\alpha,B}(\nu)$ as a function of ν/v (except for Fig. 8, where the phase is equal to 0 and thus is not shown). They show the influence of the baseline separation B (Figs. 7 and 8), the baseline angle γ (Fig. 9), the wind direction angle η (Fig. 10), and the wave-front outer scale $\mathscr{L}_0$ (Fig. 11). All calculations were carried out under the assumption of a Fried parameter $r_0 = 10$ cm at wavelength $\lambda = 0.5\ \mu$m and a pupil diameter $D = 10$ cm.

Before analyzing in detail the influence of each parameter, let us explain roughly what one could expect from the TCS modulus and phase. Consider the very general case described in Fig. 6. Points P_1 and P_2 denote pupil

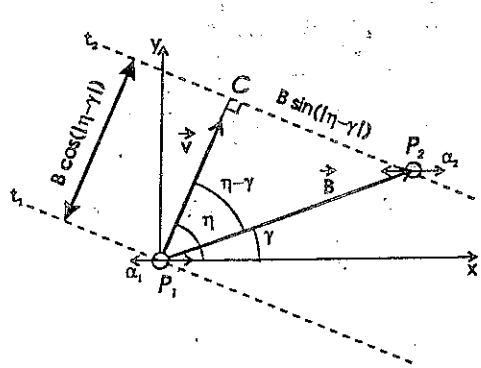


Fig. 6. Baseline components in the direction of the wind velocity and perpendicular to it. α_1 and α_2 represent the AA fluctuations along the x direction, measured at pupils P_1 and P_2, respectively. The baseline has polar coordinates (B, γ), and those of the mean wind velocity are (v, η). Dashed lines represent the perturbed wave front reaching P_1 at time t_1 and P_2 at time t_2.

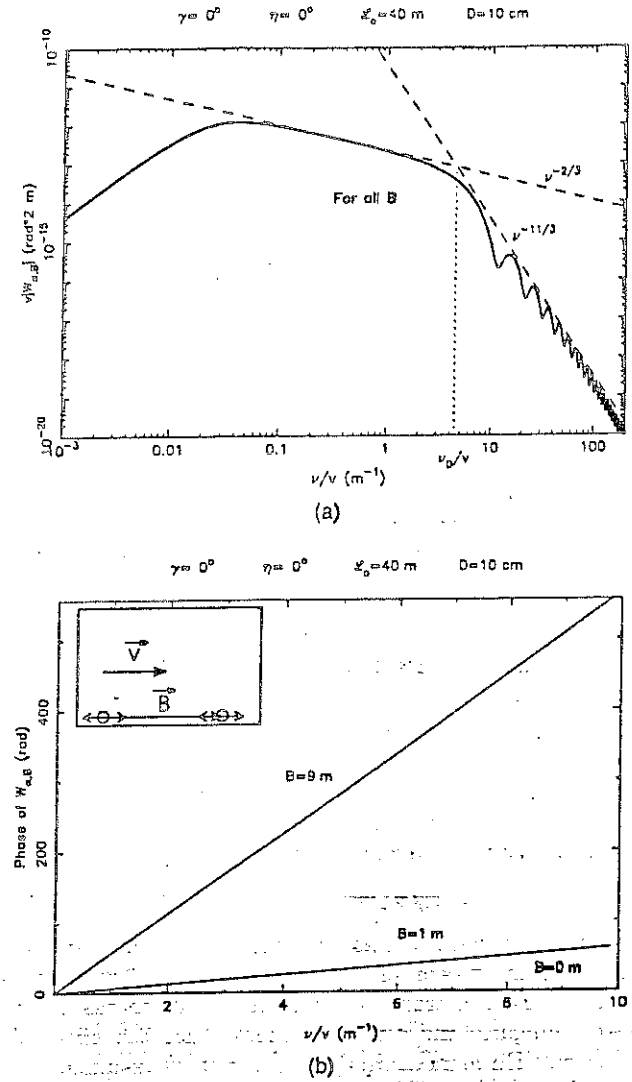


Fig. 7. Influence of the baseline separation on the AA TCS. The TCS modulus multiplied by the wind speed (a) and the TCS phase (b) is represented as functions of ν/v for three values of B, other parameters being fixed to the values shown. The scheme in (b) represents the orientations of the mean wind velocity, the baseline vector (between two circular pupils), and the AA fluctuations (arrows on pupils). Wind velocity and baseline are parallel to each other, in which case the TCS modulus in (a) equals the AA temporal power spectrum for all B. Power laws and high-frequency cutoffs are shown. In (b) the total phase and the linear phase term [Eq. (28)] are plotted, but they are exactly superimposed for all B. The unit in the vertical axis of (a) is radian^2 meter.

location. Dashed lines represent the perturbed wave front reaching pupil P_1 at time t_1 and pupil P_2 at time t_2. The perturbation, after crossing pupil P_1, passes through point C at time t_2 without deformation, assuming the Taylor hypothesis. The baseline vector B (or P_1P_2) can be decomposed as the sum of two orthogonal vectors, P_1C (in the wind direction) and CP_2. The TCS modulus with baseline B is an estimation of the statistical resemblance of the AA measured at both pupils in the frequency domain. But the measurement at P_1 is the same as the one that would be obtained at C after a time $t_2 - t_1$. So the TCS obtained with baseline B will differ from the TCS with baseline CP_2 by only a phase factor. This indicates

that the component of B in the wind direction influences only the phase of $W_{\alpha,B}(\nu)$ and that the component in the perpendicular direction modifies only its modulus. To illustrate this, Figs. 7 and 8 represent, for different values of B ($B = |\mathbf{B}|$), the TCS modulus and phase for, respectively, $\eta = \gamma = 0°$ (baseline in the wind direction) and $\eta = 0°$ and $\gamma = 90°$ (baseline perpendicular to the wind direction). In the first case, the TCS modulus is independent of B and equal to the AA power spectrum[33] that corresponds to the case $B = 0$, and its phase does depend on B; whereas, in the second case the modulus depends on B, and the phase (not represented) is equal to zero for all B. A physical justification of this behavior is the following: When the baseline is parallel to the wind direction, all the turbulent structures, small as well as large ones, cross each pupil with a temporal shift, provoking a linear phase term in the TCS. And as they travel without deformation, they are completely correlated when passing over each pupil, indicating that the TCS modulus remains unchanged when B increases. If wind and baseline are not parallel to each other, only the large turbulent structures will be able to cross both pupils. The higher the angle between wind and baseline, the larger the turbulent structures that no longer pass in front of both pupils. This explains the decorrelation at high frequencies as this angle increases.

Following this qualitative reasoning, one can expect that the TCS phase is governed mainly by the time ($t_2 - t_1$) needed for the perturbed wave front to travel from one pupil to another, which produces in the frequency domain a phase term equal to

$$\varphi(\nu) = 2\pi(t_2 - t_1)\nu. \tag{27}$$

From Fig. 6 one can easily calculate the time $t_2 - t_1$ and introduce it in the last equation to obtain

$$\varphi(\nu) = 2\pi \frac{B\cos(\eta - \gamma)}{v}\nu. \tag{28}$$

When $\eta - \gamma > 90°$, $\varphi(\nu)$ has a negative slope because the turbulent structures go from P_2 to P_1.

One can notice that expression (28) is equal to the argument of the phase factor in Eq. (26), expressed in the exponential term outside the integral. The phase term $\varphi(\nu)$ is not exactly equal to the phase of $W_{\alpha,B}(\nu)$. The integral in Eq. (26) can be seen as the Fourier transform of a function of q that is not even because of the first factor ($[(\nu/v)\cos\eta - q\sin\eta]^2$), producing a nonzero imaginary part of the integral result. This factor comes from the particular direction of the AA fluctuations that provokes an anisotropy in the AA spatial spectrum. Indeed, the AA spatial spectrum is a product of the spatial spectrum of the wave-front phase (which is isotropic) multiplied by one component of the spatial frequency squared.[40] However, the contribution of this integral to the total TCS phase is weak, limited to low frequencies, and noticeable only for some parameter combinations. For instance, in the case of $\eta = \gamma = 0°$, the phases for three values of B, represented in Fig. 7(b), are exactly given by Eq. (28). Almost the same behavior is found in Fig. 9(b), which rep-

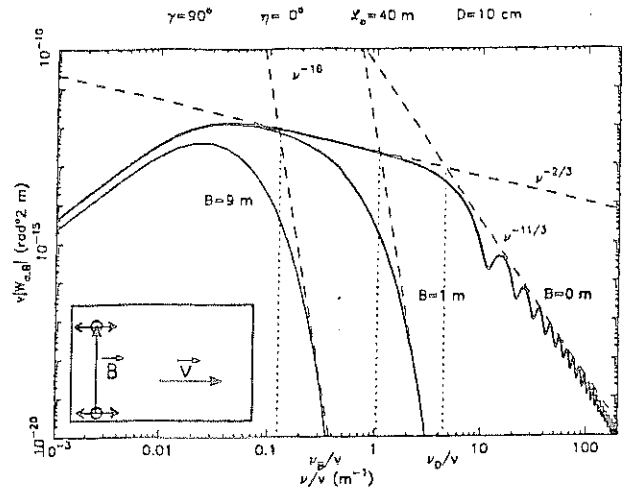
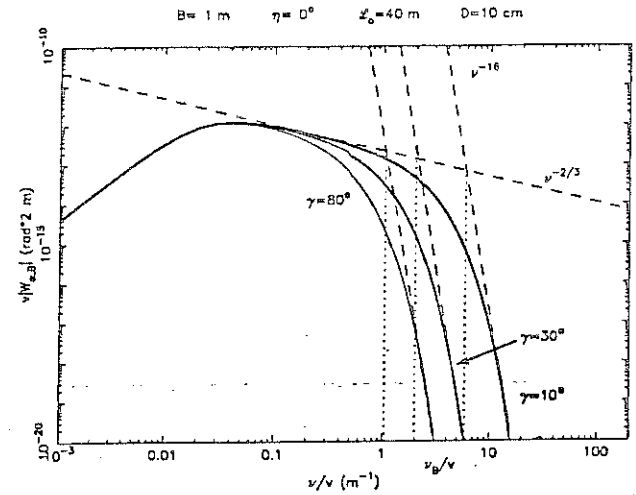


Fig. 8. Similar to Fig. 7, but with wind velocity perpendicular to the baseline, in which case the TCS phase is equal to 0 for all B and thus is not represented.



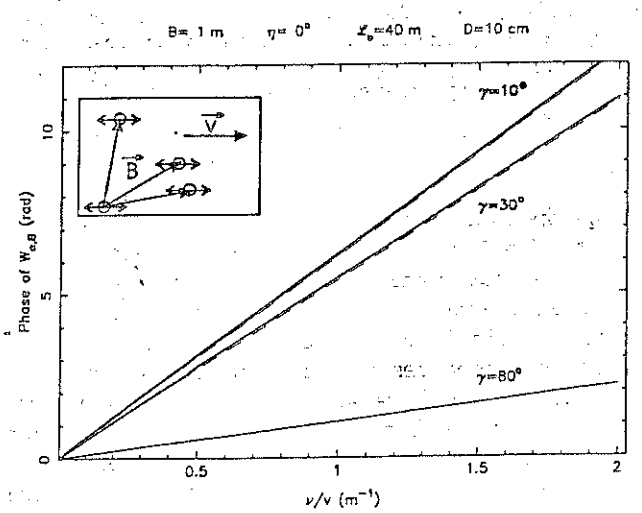


Fig. 9. Influence of the baseline angle of the AA TCS. This figure is similar to Fig. 7, but the TCS (a) modulus and (b) phase are shown for three values of the baseline angle γ. Dashed lines in (b) represent the linear phase terms [Eq. (28)], which are almost superimposed on the total phase (solid lines) for $\gamma = 10°$ and $\gamma = 30°$ and are exactly superimposed for $\gamma = 80°$.

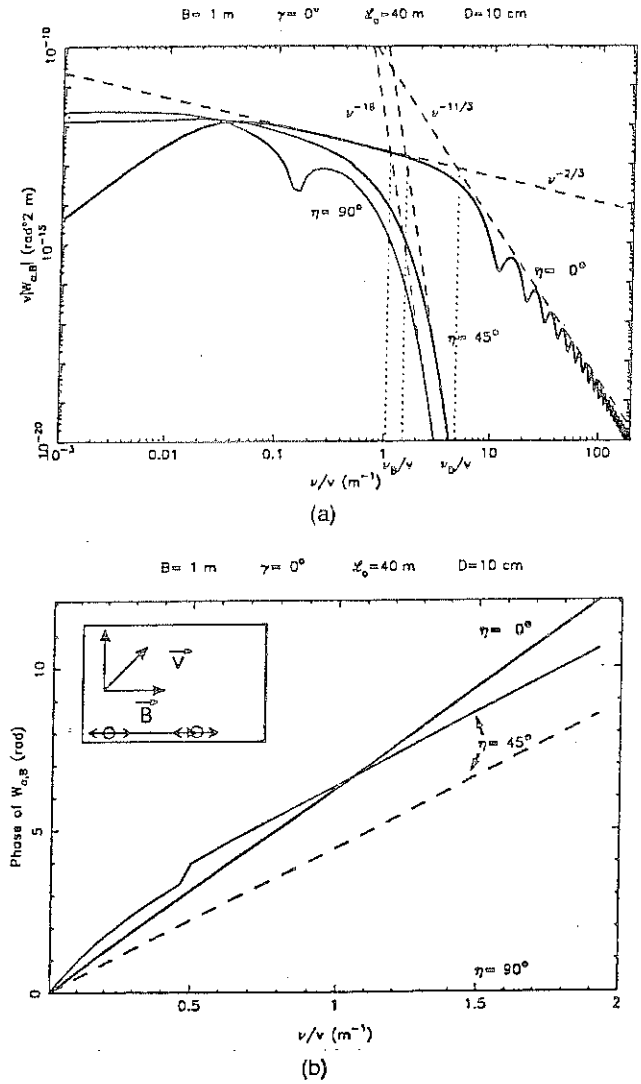


Fig. 10. Influence of the mean wind velocity angle on the AA TCS. This figure is similar to Fig. 7, but the TCS (a) modulus and (b) phase are shown for three values of the mean wind velocity angle η. The dashed line in (b) represents the phase contribution $\varphi(\nu)$ [Eq. (28)] for $\eta = 45°$. For the two other values of η, this contribution appears superimposed on the total phase, represented as solid curves.

resents the TCS phase for three values of the baseline angle γ, $B = 1$ m, and $\eta = 0°$. As the wind velocity angle η becomes higher, the contribution of the abovementioned integral to the total phase can be noticeable, as shown in Fig. 10(b), in which the TCS phase is represented for three values of η, the other parameters being fixed. In the case of $\eta = 45°$, at low frequencies the total phase (solid curve) diverges from $\varphi(\nu)$ (dashed line), but at higher frequencies both have the same slope. As explained in Subsection 5.B, the measurement of this slope leads to the wind velocity vector. No influence of the wave-front outer scale on the TCS phase has been noticed, as attested in Fig. 11(b).

Three characteristic frequencies can be identified for the TCS modulus. There is a frequency cutoff that is a consequence of a finite wave-front outer scale, given approximately by

$$\nu_{\mathscr{L}_0} \sim v/\mathscr{L}_0. \tag{29}$$

It defines a low-frequency domain for $\nu \leqslant \nu_{\mathscr{L}_0}$. It appears in all the TCS modulus plots presented, but, for simplicity, only in Fig. 11(a) is this cutoff frequency shown explicitly, for different values of $\mathscr{L}_0$. Another feature is produced by the baseline component in the direction perpendicular to the wind. It is manifested as a second frequency cutoff

$$\nu_B \simeq \frac{v}{|CP_2|} = \frac{v}{B\,\sin(|\eta - \gamma|)}. \tag{30}$$

As it is generally expected that the projection of the baseline in the direction perpendicular to the wind $[B\,\sin(|\eta - \gamma|)]$ is less than $\mathscr{L}_0$, ν_B appears at higher frequencies than $\nu_{\mathscr{L}_0}$, allowing for the definition of middle- and high-frequency domains: $\nu_{\mathscr{L}_0} \leqslant \nu \leqslant \nu_B$ and $\nu_B \leqslant \nu$, respectively. Figure 9(a) represents the TCS modulus for different values of the baseline angle γ, showing ν_B

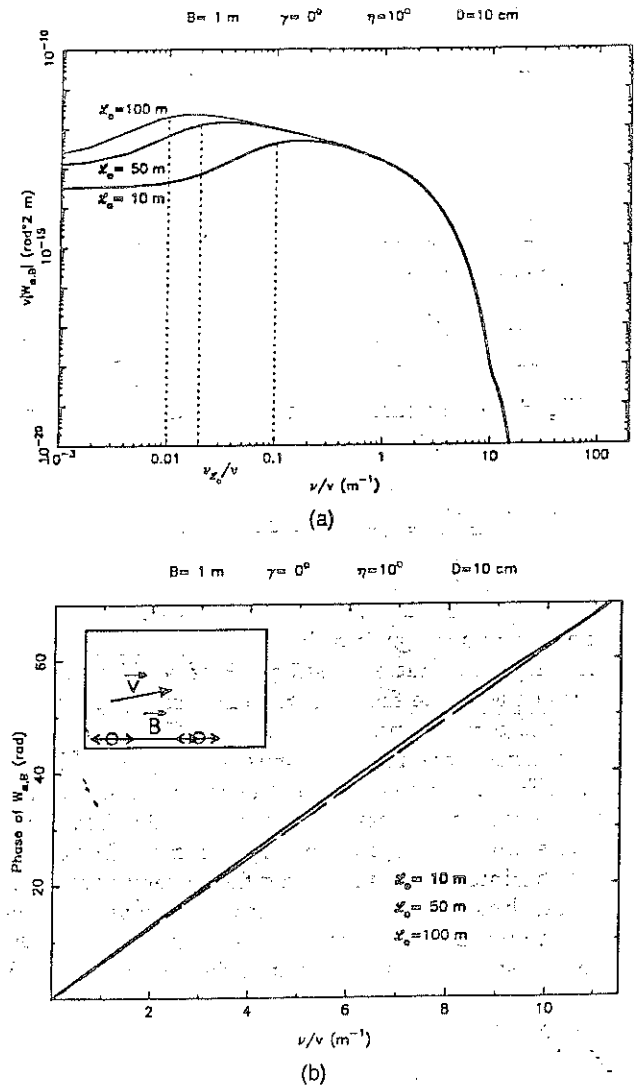


Fig. 11. Influence of the outer scale on the AA TCS. This figure is similar to Fig. 7, but the TCS (a) modulus and (b) phase are shown for three values of the outer scale $\mathscr{L}_0$. Low-frequency cutoffs are shown. No significant influence on the TCS phase is noticed.

explicitly. It is empirically found that in the middle-frequency domain the TCS modulus follows a $\nu^{-2/3}$ power law (encountered also in the AA power spectrum) and that at high frequencies the TCS modulus tends approximately to a ν^{-16} power law. These power laws are represented by lines with the corresponding slopes and tangent to the TCS modulus curve. Note that the value of the cutoff frequency ν_B defined by relation (30) corresponds very precisely to the abscissa of the intersection point of the lines representing the power laws for all the parameter-value combinations in which this cutoff frequency is present.

When $B\ \sin(|\eta - \gamma|)$ becomes smaller than the pupil diameter, the TCS modulus equals the AA power spectrum. The high-frequency cutoff is then dominated by the pupil filtering and is estimated by

$$\nu_D = 0.5\,\frac{v}{D}, \tag{31}$$

in which case the middle- and high-frequency domains are defined by $\nu_{\mathscr{L}_0} \leqslant \nu \leqslant \nu_D$ and $\nu_D \leqslant \nu$, respectively. Figure 7(a) shows an example of such a case for three values of B and $\eta = \gamma = 0°$. The curves are exactly superimposed because the baseline and the wind are in the same direction ($\eta - \gamma = 0°$), implying that $B\ \sin(|\eta - \gamma|) = 0$ for all B. At high frequency a $\nu^{-11/3}$ power law is found. The graphical procedure for determining the cutoff frequency ν_D is analogous to the one employed in the case of ν_B. Conan *et al.*[33] found the same high-frequency power law for the AA power spectrum with an infinite outer scale, but they estimated the corresponding cutoff frequency to be near $0.3(v/D)$. The difference between this expression and relation (31) comes from the graphical procedure used for identifying the cutoff frequency. Figure 10(a) represents the influence of the wind velocity angle η on the TCS modulus. It includes another example of an AA power spectrum for the case $\eta = \gamma$. For the two other values of η, one can notice the high-frequency cutoff ν_B and the ν^{-16} power law explained in Subsection 5.B. When η gets close to 90°, a valley appears in the middle-frequency range. This feature is independent of the baseline angle. It depends on the angle η between the AA measurement direction and the wind velocity. In the low-frequency range, the relative amount of energy increases as η increases. This influence of η makes it impossible to establish a power-law behavior at low frequencies. This is why the cutoff frequency $\nu_{\mathscr{L}_0}$ has not been graphically determined like ν_B and ν_D. A more complicated model would be necessary for establishing a precise graphical method of determination of $\nu_{\mathscr{L}_0}$.

5. DISCUSSION: EXPERIMENTAL POSSIBILITIES

A. Estimation of the Two-Dimensional Normalized Covariance

Takato and Yamaguchi[22] gave an analytical expression of the spatial correlation of Zernike phase-expansion coefficients with finite outer scale. It includes the correlation of the tilt, which is equivalent to the AA in one direction. As declared by those authors, the calculation is easier by numerical integration than by using the formula obtained. They also concluded that the experimental tip and tilt correlations obtained at the Keck telescope[41] do not fit theoretical curves well because the data are biased by mechanical vibrations. To avoid these problems, the normalized covariance of the AA, defined by Eq. (17), is experimentally determined in the following way by using the GSM experiment:

The covariance in the numerator of Eq. (17) is estimated from measurements obtained by using mechanically independent modules, each having a different resonance frequency. Vibrations of both modules can be considered as statistically independent processes. Tracking errors are negligible because the measurement direction of the AA is kept perpendicular to the tracking direction. For these reasons the covariance of the AA induced by vibrations and tracking errors can be different from zero solely because of statistical errors. Thus this covariance does not significantly affect the covariance of the turbulence-induced AA. Measurements used to calculate the structure function in the denominator of Eq. (17) are obtained from two modules solidly coupled to the same mounting, forming a baseline of approximately 30 cm. Vibrations and tracking errors are identical in each module, and they cancel out when calculating the structure function. Takato and Yamaguchi[22] proposed to measure tip and tilt structure functions and normalize them by the values obtained with the smallest baseline by using a Shack–Hartmann sensor on a single telescope.

B. Temporal Cross Spectrum

The TCS is a very complete statistical tool, as it contains temporal as well as spatial information on the random process under study (AA in this case). Usually, the theoretical temporal characterization of the wave front, perturbed by the atmospheric turbulence, is established by calculating exclusively temporal power spectra of the AA or any other modal component.[12–17,27,31–33] An advantage of the AA TCS in this theoretical study is that one can identify the mean wind direction in addition to the parameters obtainable from the power spectra (v, r_0, and $\mathscr{L}_0$). The most convenient method, as shown below, is to determine the slopes of $\varphi(\nu)$ [Eq. (28)] from the TCS phase in its linear region for two known baselines having different angles γ. This gives two independent linear equations from which the mean wind velocity vector (v and η) can be determined. The simplest way is to choose $\gamma = 0°$ for one of the baselines and $\gamma = 90°$ for the other, both with the same modulus B. In principle, v and η may also be deduced from the estimation of the cutoff frequency ν_B in the TCS modulus, as suggested by relation (30). However, determining ν_B implies being able to detect the ν^{-16} power law. This appears to be beyond the possibilities offered by any measurement because the expected noise at high frequencies would drastically limit the dynamic range, making it impossible to reach the asymptotic behavior. A third method consisting of the measurement of both TCS modulus and phase would lead to the same experimental difficulties. An eventual solution to this problem could be a modeling of the TCS modulus in the middle-frequency domain with ν_B/v as a pa-

rameter. Nevertheless, relation (30) contains an absolute value, which brings an ambiguity in the determination of η.

The TCS model given here assumes the frozen turbulence hypothesis. Gendron and Lena[42] have published experimental evidence of the validity of this hypothesis for baselines up to the telescope diameter that they used (3.6 m). This leads us to suppose that the TCS model is valid for short baselines, although we are convinced that this model has to serve as a basis for more detailed models including, in decreasing order of importance, multiple turbulent layers, variations in the wind velocity, and unfrozen turbulence. In the case of multiple layers, the TCS of the AA at pupils on the ground is equal to the sum of the TCS of the AA induced by each layer, assumed to be statistically independent of each other. However, the behavior of modulus and phase of the resulting TCS is not straightforward, because each individual TCS is a complex quantity. The expected effect of variations in the wind velocity for the single-layer case is to affect mainly the TCS modulus at high temporal frequencies, whereas a failure of the frozen turbulence hypothesis would rather affect principally low frequencies, because at the corresponding long time intervals there would be significant evolution of the turbulence, as already outlined by Davis *et al.*[11] Each of the three situations just mentioned needs specific investigation, which is beyond the scope of this paper.

C. Determination of $\mathscr{L}_0$

There are arguments in favor of and against the variability of $\mathscr{L}_0$ values reported in the literature (Table 1). It should not be forgotten that the wave-front outer scale can depend on the site and on seeing conditions. If thin optical turbulent layers in the free atmosphere[8] were systematically confirmed, one would expect that the contribution for large $\mathscr{L}_0$ values comes from the boundary layer. On the other hand, one can notice that the largest outer scales reported were obtained from measurements of the temporal phase power spectrum, assuming the frozen turbulence model in its interpretation. Disagreement between the spatial phase structure function at long baselines and the temporal phase power spectrum at very low frequency, when compared with the use of such a model, has been reported.[15] Estimation of $\mathscr{L}_0$ from temporal power spectra suffers strongly if the frozen turbulence hypothesis fails, because the signature of $\mathscr{L}_0$ occurs at very low frequencies. Our understanding of the effect of turbulence at baselines near the wave-front outer scale needs further work, especially concerning the temporal evolution. For these reasons we decided to estimate the wave-front outer scale from the spatial AA covariances measured with several baselines, which has been the leading idea in designing the GSM,[23,38] instead of exploiting the cutoff frequency $\nu_{\mathscr{L}_0}$ of the AA TCS modulus, expressed in relation (29). The theoretical model of the spatial 2-D covariance of the AA fluctuations does not assume any temporal behavior, such as, for instance, the frozen turbulence hypothesis. The only condition in the experimental estimation is to measure the AA simultaneously at both pupils during an exposure time sufficiently short to admit that the turbulence does not evolve at all. In the specific case of the GSM experiment, the effective exposure time is 5 ms. Until now, interferometric techniques have not been able to achieve multiple simultaneous baselines, making a purely spatial analysis for determining $\mathscr{L}_0$ difficult, which explains the repeatedly reported phase temporal power spectrum measurements toward that same goal.

6. SUMMARY

Theoretical calculation and analysis of the 2-D covariance and the TCS of the AA fluctuations induced by atmospheric turbulence have been presented. This theoretical work was inspired by the data analysis that will be performed with the GSM AA measurements. Great attention was paid to the wave-front outer scale $\mathscr{L}_0$, introduced by means of the von Kármán phase spectrum, with an infinitely small inner scale. Both results apply for any baseline vector in the mean wave-front plane. The AA TCS was calculated under the consideration that the wave front is carried by the wind without deformation, with a mean velocity $\mathbf{v}$, for times greater than or of the order of $\mathscr{L}_0/|\mathbf{v}|$. A method for obtaining an experimental 2-D normalized covariance of AA that avoids bias introduced by possible mechanical vibrations and that correctly takes into account the effect of the wave-front outer scale consists of dividing the covariance of AA measured with mechanically uncoupled devices by the structure function of AA measured with mechanically coupled devices, both measurements being synchronized. Fitting experimental AA normalized covariance to the theoretical model presented here allows retrieval of the wave-front outer scale. The Fried parameter r_0 can also be estimated from the same AA structure function measurements. The behavior of the AA TCS modulus at temporal frequencies lower than the cutoff imposed by the outer scale is similar to the behavior of the AA temporal power spectrum. The baseline component in the wind direction influences the slope of the TCS phase, whereas the component in the perpendicular direction defines cutoff frequencies in the TCS modulus. When the projection of the baseline in the direction perpendicular to the wind is smaller than the pupil size, the AA TCS modulus equals the AA temporal power spectrum. It was shown that one can calculate the mean speed, as well as the mean direction, of the wind from slopes of TCS phases obtained with at least two baselines not parallel to each other. The coherence time of the wave front can be evaluated from the Fried parameter r_0 and the mean wind speed.[15] We prefer not to try to determine $\mathscr{L}_0$ from the AA TCS, because strong uncertainties remain in the validity of the Taylor hypothesis for long baselines. Results presented here concerning the AA TCS are valid for a frozen turbulence and should serve as a basis for further work toward a multilayer model. Further investigations are to be undertaken for a satisfactory model of the temporal behavior of the wave front at baselines greater than the outer scale.

When this research was performed, Remy Avila was on leave from Instituto de Astronomía, Universidad Nacional Autonoma de México, Apartado Postal 70-264, 04510 México D.F., México.

REFERENCES

1. J. Borgnino, "Estimation of the spatial coherence outer scale relevant to long baseline interferometry and imaging in optical astronomy," Appl. Opt. **29**, 1863–1865 (1990).
2. C. E. Coulman, J. Vernin, Y. Coqueugniot, and J. L. Caccia, "Outer scale of turbulence appropriate to modeling refractive-index structure profiles," Appl. Opt. **27**, 155–160 (1988).
3. R. R. Beland and J. H. Brown, "A deterministic temperature model for stratospheric optical turbulence," Phys. Scr. **37**, 419–423 (1988).
4. C. E. Coulman, "Vertical profiles of small-scale temperature structure in the atmosphere," Boundary-Layer Meteorol. **4**, 169–177 (1973).
5. J. L. Bufton, "Comparison of vertical profile turbulence structure with stellar observations," Appl. Opt. **12**, 1785–1793 (1973).
6. R. Barletti, G. Ceppatelli, L. Paternò, A. Righini, and N. Speroni, "Daytime r_0 evaluated from vertical microthermal measurements," Appl. Opt. **16**, 2419–2421 (1977).
7. F. Delaudier, D. Sidi, M. Crochet, and J. Vernin, "Direct evidence of 'sheets' in the atmospheric temperature field," J. Atmos. Sci. **51**, 237–248 (1994).
8. C. E. Coulman, J. Vernin, and A. Fuchs, "Optical seeing-mechanism of formation of thin turbulent laminae in the atmosphere," Appl. Opt. **34**, 5461–5474 (1995).
9. A. Fuchs, "Contribution à l'étude de l'apparition de la turbulence optique dans les couches minces. Concept du SCIDAR généralisé," Thèse de doctorat (Université de Nice, Nice, France, 1995).
10. J. M. Mariotti and G. P. Di Benedetto, "Pathlength stability of synthetic aperture telescopes: the case of the 25 cm CERGA interferometer," in *Very Large Telescopes, Their Instrumentation and Programs*, Proceedings of International Astronomical Union Colloquium 79, M. H. Ulrich and K. Jear, eds. (European Southern Observatory, Garching, Germany, 1984), pp. 257–265.
11. J. Davis, P. R. Lawson, A. J. Booth, W. J. Tango, and E. D. Thorvaldson, "Atmospheric path variations for baselines up to 80 m measured with the Sydney University Stellar Interferometer," Mon. Not. R. Astron. Soc. **277**, L53–L58 (1995).
12. N. S. Nightingale and D. F. Buscher, "Interferometric seeing measurements at the La Palma Observatory," Mon. Not. R. Astron. Soc. **251**, 155–166 (1991).
13. C. A. Haniff, J. E. Baldwin, P. J. Warner, and T. R. Scott, "Atmospheric phase fluctuation measurements: interferometric results from the WHT and COAST telescopes," in *Amplitude and Intensity Spatial Interferometry II*, J. B. Breckinridge, ed., Proc. SPIE **2200**, 407–417 (1994).
14. M. M. Colavita, M. Shao, and D. H. Staelin, "Atmospheric phase measurements with the Mark III stellar interferometer," Appl. Opt. **26**, 4106–4112 (1987).
15. D. F. Buscher, J. T. Armstrong, C. A. Hummel, A. Quirrenbach, D. Mozurkewich, K. J. Johnston, C. S. Denison, M. M. Colavita, and M. Shao, "Interferometric seeing measurements on Mt. Wilson: power spectra and outer scales," Appl. Opt. **34**, 1081–1096 (1995).
16. D. F. Buscher, J. T. Armstrong, D. Mozurkewich, and C. S. Denison, "Atmospheric fluctuation measurements with the MKIII interferometer and the power spectra of everything," in *High Resolution Imaging by Interferometry II*, Proceedings of European Southern Observatory Conference 39, J. M. Beckers and J. M. Merkle, eds. (European Southern Observatory, Garching, Germany, 1991), pp. 1029–1038.
17. M. Bester, W. C. Danchi, C. G. Degiacomi, L. J. Greenhill, and C. H. Townes, "Atmospheric fluctuations: empirical structure functions and projected performances of future instruments," Astrophys. J. **392**, 357–374 (1992).
18. Ph. Berio, D. Mourard, F. Vakili, J. Borgnino, and A. Ziad, "Effects of atmospheric spectral decorrelation on visibility measurements in Michelson interferometry," J. Opt. Soc. Am. A **14**, 114–121 (1997).
19. M. Tallon, "Contributions à l'imagerie à Haute Résolution Angulaire: analyse de la surface d'onde, source laser de référence, optique adaptative," Thèse de doctorat (Université de Nice, Nice, France, 1989).
20. F. Rigaut, G. Rousset, P. Kern, J. C. Fontanella, J. P. Gaffard, F. Merkle, and P. Lena, "Adaptive optics on a 3.6 m telescope: results and performance," Astron. Astrophys. **250**, 280–290 (1991).
21. A. Ziad, J. Borgnino, F. Martin, and A. Agabi, "Experimental estimation of the spatial-coherence outer scale from a wavefront statistical analysis," Astron. Astrophys. **282**, 1021–1033 (1994).
22. N. Takato and I. Yamaguchi, "Spatial correlation of Zernike phase-expansion coefficients for atmospheric turbulence with finite outer scale," J. Opt. Soc. Am. A **12**, 957–965 (1995).
23. A. Agabi, J. Borgnino, F. Martin, A. Tokovinin, and A. Ziad, "G.S.M.: a Grating Scale Monitor for atmospheric turbulence measurements. II. First measurements of the wavefront outer scale at the O.C.A.," Astron. Astrophys. Suppl. Ser. **109**, 557–562 (1995).
24. A. Ziad, J. Borgnino, A. Agabi, and F. Martin, "Optimized spectral bandwidth in high angular resolution imaging, effect of a finite spatial-coherence outer scale," Exp. Astron. **5**, 247–268 (1994).
25. A. Ziad, "Estimation des échelles limites de cohérence spatiale des fronts d'onde et optimisation des observations à Haute Résolution Angulaire en Astronomie," Thèse de doctorat (Université de Nice, Nice, France, 1993).
26. D. M. Winker, "Effect of a finite outer scale on the Zernike decomposition of atmospheric optical turbulence," J. Opt. Soc. Am. A **8**, 1568–1573 (1991).
27. V. V. Voitsekhovich and S. Cuevas, "Adaptive optics and the outer scale of turbulence," J. Opt. Soc. Am. A **12**, 2523–2531 (1995).
28. G. Boreman and C. Dainty, "Zernike expansions for non-Kolmogorov turbulence," J. Opt. Soc. Am. A **13**, 517–522 (1996).
29. F. Roddier, J. M. Gilli, and G. Lund, "On the origin of speckle boiling and its effects in stellar speckle interferometry," J. Opt. (Paris) **13**, 263–271 (1982).
30. F. Roddier and P. Lena, "Long-baseline Michelson interferometry with ground-based telescopes operating at optical wavelengths," J. Opt. (Paris) **15**, 171–182 (1984).
31. C. Aime, J. Borgnino, F. Martin, R. Petrov, and G. Ricort, "Contribution to the space–time study of stellar speckle patterns," J. Opt. Soc. Am. A **3**, 1001–1009 (1986).
32. F. Roddier, M. J. Northcott, J. E. Graves, and D. L. McKenna, "One-dimensional spectra of turbulence-induced Zernike aberrations: time-delay and isoplanicity error in partial adaptive compensation," J. Opt. Soc. Am. A **10**, 957–965 (1993).
33. J.-M. Conan, G. Rousset, and P.-Y. Madec, "Wave-front temporal spectra in high-resolution imaging through turbulence," J. Opt. Soc. Am. A **12**, 1559–1570 (1995).
34. P.-Y. Madec, J.-M. Conan, and G. Rousset, "Temporal characterisation of atmospheric wavefront for adaptive optics," in *Progress in Telescopes and Instrumentation Technologies*, Proceedings of European Southern Observatory Conference 42, M.-H. Ulrich, ed. (European Southern Observatory, Garching, Germany, 1992), pp. 471–474.
35. G. Rousset, P.-Y. Madec, and D. Rabaud, "Adaptive optics partial correction simulation for two telescope interferometry," in *High Resolution Imaging by Interferometry II*, Proceedings of European Southern Observatory Conference 39, J. M. Beckers and J. M. Merkle, eds. (European Southern Observatory, Garching, Germany, 1991), pp. 1095–1104.
36. H. M. Martin, "Image motion as a measure of seeing quality," Publ. Astron. Soc. Pac. **99**, 1360–1370 (1987).
37. B. Lopez, "How to monitor optimum exposure times for high resolution imaging modes?" Astron. Astrophys. **253**, 635–640 (1992).
38. F. Martin, A. Tokovinin, A. Agabi, J. Borgnino, and A. Ziad, "G.S.M.: a Grating Scale Monitor for atmospheric turbulence measurements. I. The instrument and first results of angle of arrival measurements," Astron. Astrophys. Suppl. Ser. **108**, 173–180 (1994).
39. F. Roddier, "The effects of atmospheric turbulence in opti-

cal astronomy," in *Progress in Optics*, E. Wolf, ed. (North-Holland, Amsterdam, 1981), Vol. 19, pp. 281–376.
40. J. Borgnino, F. Martin, and A. Ziad, "Effect of a finite outer scale on the covariances of angle-of-arrival fluctuations," Opt. Commun. 91, 267–269 (1992).
41. F. Dekens, D. Kirkman, G. Chanan, T. Mast, J. Nelson, G. Illingworth, and P. Wizinowich, "High speed seeing measurements at Keck telescope," in *Adaptive Optics in Astronomy*, M. A. Ealey and F. Merkle, eds., Proc. SPIE 2201, 310–313 (1994).
42. E. Gendron and P. Lena, "Single layer atmospheric turbulence demonstrated by adaptive optics observations," Astrophys. Space Sci. 239, 221–228 (1996).

A&A manuscript no.
(will be inserted by hand later)

Your thesaurus codes are:
03 (03.01.2; 03.19.1; 02.20.1)

ASTRONOMY AND ASTROPHYSICS
February 21, 2000

Optical parameters relevant for High Angular Resolution at Paranal from GSM instrument and surface layer contribution

F. Martin[1], R. Conan[1], A. Tokovinin[3], A. Ziad[1], H. Trinquet[1], J. Borgnino[1], A. Agabi[1], and M. Sarazin[2]

[1] U.M.R. Astrophysique N°6525, Université de Nice-Sophia Antipolis, F-06108 Nice Cedex 2, France
[2] European Southern Observatory, Karl-Schwarzschild-Str. 2, D-85748 Garching bei München, Germany
[3] Sternberg Astronomical Institute, Universitetsky prosp., 13, 119899 Moscow, Russia

Received ... / Accepted ...

Abstract. Main atmospheric parameters characterizing the turbulence were measured at the Paranal ESO Observatory (Chile) with the Generalized Seeing Monitor (GSM) during 19 nights in November–December 1998. The median seeing for this period was 0.88″, a little worse than average , the spatial coherence outer scale of the wavefront $\mathcal{L}_0$ = 22.0 m and the median isoplanatic angle θ_0= 1.90″. A very good agreement with seeing values given by ESO DIMM was found. Effects of ground layer turbulence were estimated from measurements of temperature micro-fluctuations at several altitudes. These measurements revealed that the first 21 meters above ground account for 12.5% of the total turbulent energy. Comparison between GSM and ESO DIMM values have permitted to highlight a local phenomenon which occurs sometimes at the site in the middle of the night. Statistics of the refractive index structure constant C_n^2 in the surface layer is also studied.

Key words: turbulence – atmospheric effects – site testing – high angular resolution – outer scale

1. Introduction

It is well known that performances of high angular resolution techniques (HAR) are severely limited by the random optical effects induced by the turbulent atmosphere on the light propagation. A quantitative spatial and temporal characterization of the corrugated wavefront at the ground is necessary to optimize the operation of adaptive optics (AO) and long baseline interferometry (LBI) instruments and to guide the future development of these techniques.

The parameters which characterize the wavefront statistics from an optical point of view are the well known Fried's parameter $r_0(\lambda)$, the spatial coherence outer scale of the wavefront $\mathcal{L}_0$ (called outer scale hereafter), which becomes of importance when comparable to the telescope aperture, the isoplanatic angle $\theta_0(\lambda)$, and the characteristic time which determines the response time for the deformable mirror in AO or for the fringe tracking in LBI.

A specific instrument named GSM (Generalized Seeing Monitor)dedicated to the monitoring of these parameters has been built. It has been essentially developed (Martin et al. 1994) to evaluate the outer scale statistics because no systematic measurements existed for it. The scattered values available in the literature were deduced from various techniques and were somewhat controversial (Mariotti et al. 1984, Colavita et al.1987, Rigaut et al. 1991, Ziad et al. 1994, Buscher et al. 1995, Takato et al. 1995, Davis et al. 1995, Beriot et al. 1997)

The VLT system with its four 8 m apertures is a set of optical telescopes. It is located at the ESO Cerro Paranal observatory in Chile which is among the major world astronomical sites. The properties of the atmospheric turbulence at this site are of the utmost importance for the operation of this unique system.

A statistics of seeing and cloud coverage at Paranal over several years was obtained from the Differential Image Motion Monitor of ESO (Sarazin & Roddier 1990) and shows it to be one of the lowest among those measured at several astronomical sites, with the long-term median seeing of 0.70″. However, the information on some other properties of atmosphere at Paranal was missing. The aim of our measurement campaign with GSM in December 1998 was to provide statistics of the outer scale $\mathcal{L}_0$ and of the isoplanatic angle θ_0. The corresponding results are presented in section 3.

Previously, the GSM worked successfully at the ESO La Silla observatory (Martin et al. 1998b), and in some other observatories over the world (Oukaïmeden in Morocco, Maydanak in Uzbekistan, and Cerro Pachon in Chile, the southern site for the Gemini project).

Send offprint requests to: F. Martin
Correspondence to: Francois.MARTIN@unice.fr

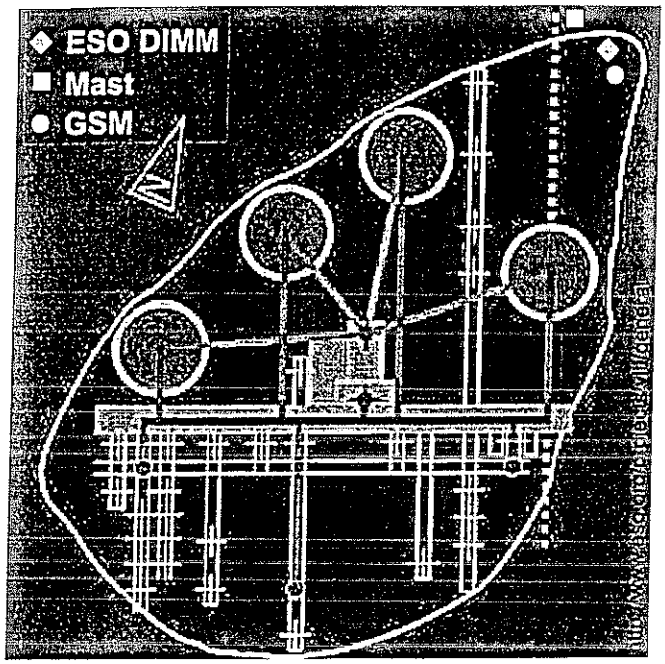


Fig. 1. The plan of Paranal site and the location of the equipment.

The schematic plan of the Paranal site is given in Fig. 1. The pillars with GSM telescopes were located near the ESO DIMM seeing monitor. A pre–existing mast was used to install three couples of temperature sensors for temperature micro–fluctuation measurements in the Surface Layer (SL).

All atmospheric parameters given in this report are calculated for a wavelength $\lambda = 500$ nm for observations at zenith. Seeing angle ε is the full width at half maximum (FWHM) of a long-exposure stellar image in a large telescope, $\varepsilon = 0.98\lambda/r_0$. Outer scale $\mathcal{L}_0$ is a C_n^2–weighted average of the local turbulence outer scale $\mathcal{L}_0(\mathrm{h})$, as defined by Borgnino (1990). The isoplanatic angle θ_0 is relevant for adaptive optics (Fried 1982).

2. Principle of measurements

Although the Generalized Seeing Monitor was the main instrument used in this campaign, we devote little space to its description, which can be found in our previous works.

2.1. Principle of the GSM

In its initial version GSM is presented in Martin et al. (1994). The actual instrument is described in Martin et al. (1998b) and Tokovinin et al. (1998b). Description and performance analysis are also given in Ziad et al. (1999). We refer the interested readers to the reports on the previous GSM missions (Martin et al. 1998a and Tokovinin et al. 1998a).

The GSM instrument consists of four 10-cm telescopes with their individual image analysis devices to sense the angle of arrival (AA) fluctuations in one direction, called *modules*. The telescopes are installed on three equatorial mounts; two modules share the same mount and are working as the ESO DIMM. At a distance of 1 meter to the south of these modules a third one is installed on a separate mount. The fourth one, with its mount, is located at 0.8 m to the east. The same L–shaped configuration has been used in the previous GSM missions except at Maydanak site.

GSM modules and their mounts were installed on top of 3 concrete pillars, with the height of telescopes 1.7 m above ground. From 3 sides the experiment was surrounded by a wind-protective enclosure consisting of a 2 m high net.

Atmospheric AA fluctuations are measured by each module in the declination direction, with 5 ms time resolution. A typical measurement consists of a 2 mn long data acquisition. It is processed immediately, providing the estimate of the Fried's coherence diameter r_0 (from differential AA fluctuations in modules 1 and 2), outer scale $\mathcal{L}_0$ (inferred from the covariances of AA and computed via the Von Karman model for the phase spectrum of the turbulent atmosphere), and isoplanatic angle θ_0 (from scintillation index).

The ESO DIMM seeing monitor (Sarazin & Roddier 1990) which operates at the Paranal site continuously was located at a distance of the order of 10 meters from GSM. It is installed on a 6 m high tower, in order to avoid the near-ground turbulence effects as much as possible.

2.2. Temperature micro-fluctuation measurements in the surface layer

Turbulence sensing in the SL has been undertaken in order to gain a better understanding of the turbulence effects near the ground. For balloon measurements of the vertical turbulence profiles,very sensitive temperature sensors have been developed in our laboratory. Each probe consists of two thin-wire sensors mounted at a separation of 1 m on a rod. The structure constant of temperature fluctuations, C_T^2, is calculated from the dispersion of the temperature difference between the pair of sensors. The time resolution of the micro–thermometers with their electronics and transmitting devices is about 5 ms and an integrated value of the structure constant is transmitted to the ground each 1.5 s. The typical noise level can reach a few 10^{-8} (Celsius degree)^2. The refractive index structure constant C_n^2 is calculated from C_T^2 using the appropriate values of mean temperature and pressure. C_n^2 values are obtained with a precision around 10^{-20} m$^{-2/3}$. Previous results obtained with this equipment can be found in Vernin & Muñoz-Tuñon (1992).

Four pairs of sensors were installed on the meteorological mast at the heights of 3, 7, 21, and 31 m above the base of the mast. The upper sensor, however, was damaged, and only the remaining 3 have provided valid data.

It must be noted that the base of the mast was somewhat lower (by 1 m) than the ground level of GSM/DIMM location. Hence the sensors at 3 and 7 meters are at the same heights as GSM and DIMM, respectively.

3. The GSM campaign at Cerro Paranal Observatory

The GSM instrument has been transported to Paranal after the completion of the previous mission in October 1998 at Cerro Pachon (Chile).

The excellent quality of Paranal site have permitted to collect 1884 acquisitions during 19 nights, more than in any previous GSM campaign.

Micro-thermal data acquisitions have been operational only during 9 nights.

3.1. Results of the campaign

Throughout this report the universal time (UT) is given. A date always refers to the beginning of the night. The data summary for the mission is presented in Table 1. In the first columns we give date, median speed and direction of the wind at 10 m altitude. Next 3 columns contain the nightly median values of main atmospheric parameters measured by GSM, namely seeing ε, outer scale $\mathcal{L}_0$ and isoplanatic angle θ_0. In the last column the seeing values computed by the ESO DIMM are listed.

During our mission the overall median seeing was slightly worse than long-term average for Paranal (0.70″), but typical for the whole 1998 year, with its monthly average seeing of $0.9'' - 1''$. We note a very good stability of atmospheric parameters. Notably, in the period of December $1 - 5$ surprisingly little variation of all main parameters occurred. Similar values were found again on December 15, 16 and 17.

The graphic representation of the ensemble of GSM data is given in Fig. 2.

3.2. Outer scale statistics

GSM is the first instrument capable to measure the outer scale $\mathcal{L}_0$ continuously and to study the statistics of this important parameter. During its previous missions it was found that $\mathcal{L}_0$ follows a log-normal distribution with a dispersion of $\log(\mathcal{L}_0)$ of about 0.23 , and , rather similar median values, ranging from 24 to 31 m, were obtained in all GSM campaigns (Ziad et al. 1999). Large isolated values of $\mathcal{L}_0$, called "bursts", were also noted at all sites.

At Paranal we, for the first time, registered during several periods relatively small and stable outer scales. Our overall median $\mathcal{L}_0 = 22.0$ m is smaller than at other sites studied.

In the plot of $\mathcal{L}_0$ given in Fig. 2(a) we note the occurrence of two nights with relatively large median values of $\mathcal{L}_0$ (45 and 48 m).On both these nights the wind of 6 m/s was blowing from South, which is not typical for Paranal.

During any single night there is no obvious systematic correlation of $\mathcal{L}_0$ with seeing, even if a poor correlation appears sometimes.

The bursts of $\mathcal{L}_0$ exist at Paranal, as well as at other sites.

Curiously, a burst occurred at about the same time, 03h30 UT, during several nights. We believe that this effect is not an artefact, but reflects some real changes in the turbulence regime at Paranal site. Persistent local effects occurring in the SL at the same local time during several nights were also found (see below).

Table 1. Data summary

Date	Wind at 10 m		ε	$\mathcal{L}_0$	θ_0	$\varepsilon_{\rm DIMM}$
	m/s		″	m	″	″
27.11	7.3	E→N	0.81	23.8	1.95	0.79
28.11	0.6	S→W	0.67	15.6	2.45	0.97
29.11	6.9	SE (stable)	0.99	45.3	1.68	1.05
30.11	3.6	S→W	1.02	21.7	1.90	1.00
1.12	4.1	S→NW→NE	0.90	16.7	1.78	0.85
2.12	5.4	N→E→N	0.88	16.9	1.75	0.85
3.12	4.8	E→N	0.79	16.8	1.97	0.76
4.12	4.5	E→N	0.81	17.0	2.17	0.69
5.12	5.2	E→N	0.90	16.5	2.09	0.87
6.12	8.3	N→NE	0.86	24.5	1.74	0.84
7.12	6.5	N→NE	1.03	19.4	1.48	0.95
8.12	3.2	S→N	0.90	16.9	1.51	0.80
14.12	6.3	S (stable)	0.92	48.4	1.95	0.95
15.12	3.4	SE→N	0.95	21.5	2.22	0.80
16.12	3.1	SE→N→NE	0.89	17.5	2.54	0.96
17.12	6.5	E→N	0.89	23.6	1.41	0.99
18.12	8.8	N→NE	1.31	37.0	3.17	1.46
19.12	10.8	N (stable)	0.73	33.9	2.09	0.83
20.12	6.5	E→N	1.29	23.7	1.41	1.30
Average median values			0.88	22.0	1.90	0.87

4. Contribution of the surface layer to the overall seeing

4.1. Surface layer detection from GSM and DIMM measurements

A comparison of seeing values measured simultaneously by ESO DIMM and GSM shows that most of the time both instruments are in excellent mutual agreement. An example of such agreement is given in Fig. 3.

However, for some periods GSM measured a worse seeing than DIMM because of the lower height of GSM, which makes it more sensitive to the SL turbulence. This situation appeared soon after the beginning of our mission as an enigmatic effect: for several consecutive nights, starting from December 1 and until December 5, GSM registered a much worse seeing than DIMM for a period of about one

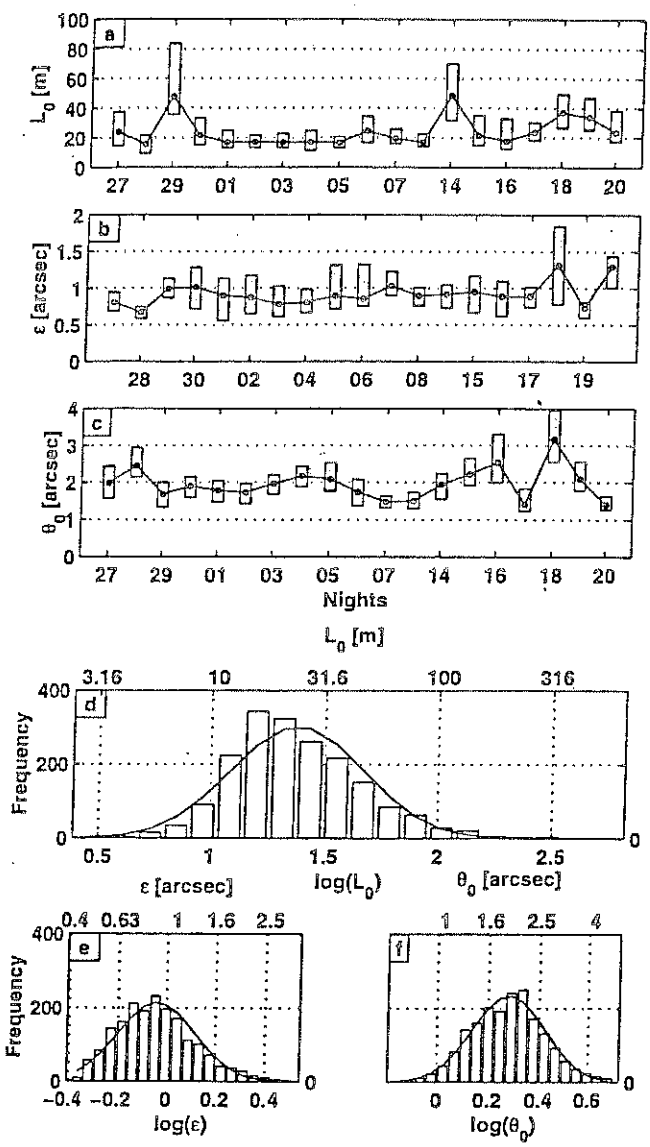


Fig. 2. Summary of the GSM data at Paranal: evolution of (a): wavefront outer scale $\mathcal{L}_0$, (b): seeing ε and (c): isoplanatic angle θ_0 during the 19 nights of the mission. For each night the median value of the considered parameter is plotted as a dot and the rectangle indicates the range in which 50% of the values are included. The histograms of these 3 parameters ((d) , (e) and (f)) correspond closely to a log–normal distribution.

hour, around local midnight. For the rest of the time, the agreement was good. A most clear example of this phenomenon (which we call here midnight local turbulence, or MLT) is given in Fig. 4. On December 2, starting from 03h00 UT, GSM gave a seeing systematically worse than that given by DIMM. This particular local phenomenon (MLT) is explained in the next subsection.

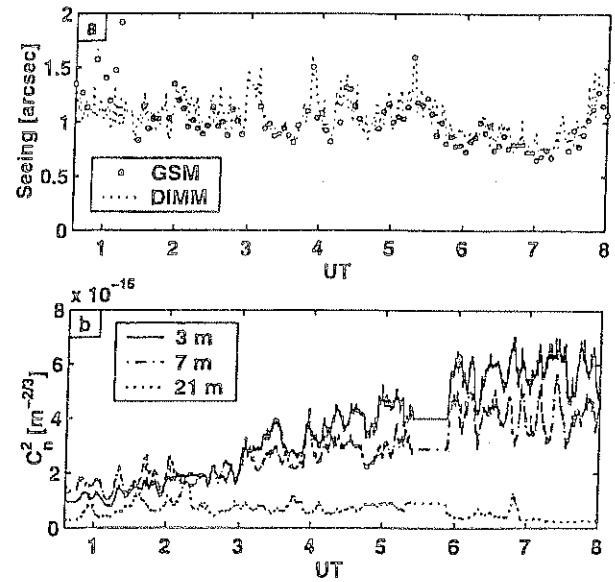


Fig. 3. The seeing measured by GSM (full circles) and ESO DIMM (dotted line) on the night of November 29 is plotted in the upper panel, showing an excellent agreement between both instruments. Simultaneous recordings of the C_n^2 with temperature sensors at the heights of 3, 7 and 21 m are plotted in the lower panel.

4.2. Statistical contribution of the surface layer to the global seeing

The micro-thermal data, also plotted in Fig. 3 and Fig. 4, confirm the idea that the divergence between GSM and DIMM seeing values is caused by the strong turbulence in the first few meters above the ground. Indeed, the period of disagreement exactly matches the turbulence increase at 3 m. Similar behavior was observed on the nights of December 1–5 corresponding to the period of stable atmospheric conditions, already noted in Sect. 3. Ground wind of 5 m/s was prevailing during this period, with a direction slowly changing from East to North during the night, and with moderate velocity variations.

A simple statistical processing of the temperature micro-fluctuation data permits to give a global behavior of the C_n^2 measured at the three heights during 9 nights. For each height, about 45000 values of the structure constant have been recorded and processed. The results can be seen in Fig. 5 which shows clearly that statistically the C_n^2 mean value near the ground (at 3 m) is greater than the one at 21 m. The ratio of the corresponding values of C_n^2 is approximately 16. Conversely, the dispersion grows with height.

To estimate the relative contribution of the SL to the total seeing degradation, a turbulent energy ratio (TER) can be defined as the ratio of the turbulent energies in the

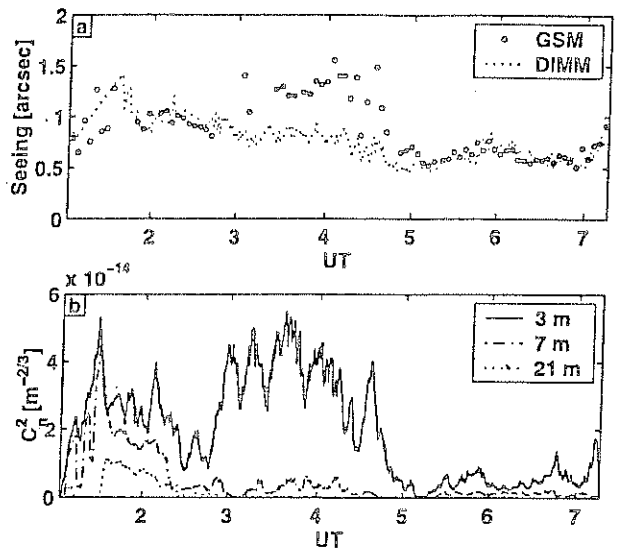


Fig. 4. Same as Fig. 3 for the night of December 2. The local turbulence around midnight caused the difference of the seeing measured by GSM and DIMM. It matches the increase of C_n^2 at the height of 3 m.

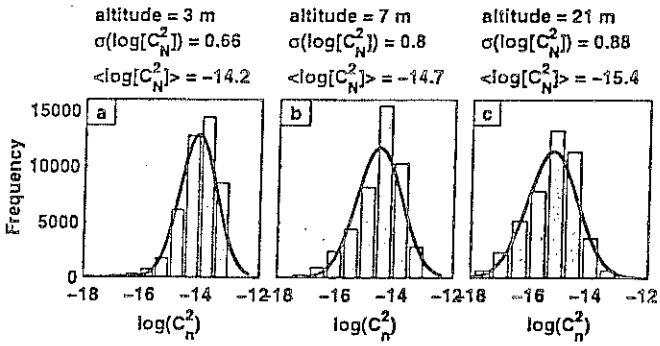


Fig. 5. Histograms of the C_n^2 values computed from the temperature sensors at 3 altitudes , (a): 3m , (b):7m and (c):21m

(3m–21m) and (3m – infinity) layers:

$$TER = \frac{\int_{3m}^{21m} C_n^2 dh}{\int_{3m}^{+\infty} C_n^2 dh} \quad (1)$$

For all the nights during which temperature data where available, this ratio has been computed each four minutes in order to match the sampling rate of the GSM which provides the turbulent energy from 3 m to infinity. Numerator of the above expression is deduced from the integration of rough C_n^2 profile given by the temperature sensors between 3 m and 21 m. Night by night mean values of the TER can be found in Fig. 6. From the table one can see that nightly values are in a ratio of 1 to 2.4.

Date	TER [%]
29.11	7.18
30.11	7.69
01.12	13.41
02.12	17.06
03.12	14.11
04.12	9.90
05.12	16.76
06.12	16.50
07.12	10.26
Mean	12.5

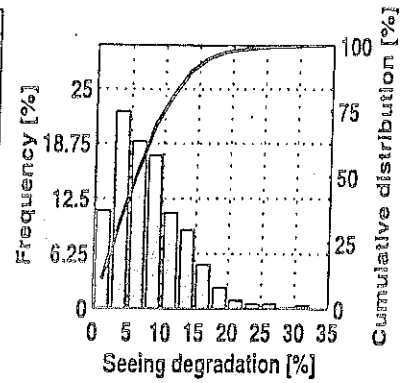


Fig. 6. Values of the turbulent energy ratio for the 9 nights for which temperature data are available. Histogram of the seeing degradation values and corresponding cumulative distribution.

In comparison with the seeing produced by turbulence layers above 21 m, a degradation would occur if the turbulent effects in the SL were added. The value of the seeing degradation (%) is given by $(1 - [1 - TER]^{0.6})$.

Histogram of the seeing degradation values and its cumulative distribution are plotted in Fig. 6. The median value is 7.2%. Fifty percent of the values centered on the median are between 4.0% and 11.0%.

It is thus evident that the contribution of the SL to the global seeing cannot always be considered as negligible and, although GSM is more affected by SL turbulence, DIMM is not always entirely free of it either. Ground turbulence, a part of which appears above DIMM but below VLT, may partially explain the difference sometimes detected between UT telescopes and DIMM seeings.

5. Conclusions

The GSM mission to Paranal was highly successful and for the first time provided statistical data on the outer scale at this site. Our main results consist in the following:

- The distribution of the outer scale $\mathcal{L}_0$ at Paranal is close to log-normal, with a median value of 22.0 m. It means that because $\mathcal{L}_0$ is comparable to the telescope aperture size the effects of the finite outer scale on the operation of VLT are significant and result in reduction of image motion.
- The correlation of $\mathcal{L}_0$ with local meteorological conditions was noted. For typical conditions of NE wind, stable nightly median values of $\mathcal{L}_0$ around 16 m are found, whereas for the southern wind (associated with the wind shear in the boundary layer) they are over 45 m.
- Excellent agreement of the seeing measured by the GSM and by the ESO DIMM is found. Median seeing for our campaign was 0.88″ for GSM and 0.87″ for DIMM.
- The median value of the isoplanatic angle θ_0 was 1.90″ during our mission. This appears as an intermediate

value in comparison with our estimations during previous measurement campaigns at other observatories (1.26″ at La Silla, 2.48″ at Maidanak and 2.73″ at Cerro Pachon). Thus, the high-altitude turbulence over Paranal appears to be not substantially different from other observatories.

- The strong local turbulence in the first few meters of the surface layer exists at Paranal for some periods of time, as evidenced by DIMM-GSM comparison and micro-thermal mast measurements.
  Turbulent energy in the SL contributes an average amount of only 12.5% to the total turbulent energy detected by GSM along the line of sight. This corresponds to an average seeing degradation around 8% if turbulence effects in the SL are added to the turbulence above 21 m. While unit telescopes of the VLT are not affected by these layers, the situation will not be the same for auxiliary telescopes (ATs) of the VLTI which have been designed closer to the ground (4.5–6.5 meters). Hence, continuous micro-thermal monitoring at Paranal appears to be desirable to study the local effects in detail and to evaluate their importance for the site seeing and particularly for the ATs.
- The temporal evolution of atmospheric parameters at Paranal seems to be rather specific (prolonged periods of stable conditions; dependence on the wind speed and its fluctuations; repeatable increases of surface layer turbulence) compared to other sites, and warrants further investigation. A better understanding of the mechanisms of Paranal seeing will eventually lead to forecast observing conditions.

The analysis of the spatio–temporal cross–correlations of the AA fluctuations can lead to the detection of the atmospheric layers (Avila et al. 1997). From the AA cross–correlations one can estimate the number of predominant turbulent layers, their respective strengths, the velocity and direction of the wind which carries the turbulent eddies. The principle of the wind measurement with GSM is given in Conan et al. (1998). The full wind analysis and cross-correlation interpretation must include simultaneous comparisons with other parameters, $\mathcal{L}_0$, ε and θ_0. The methods of such complete analysis are still under development.

Acknowledgements. The success of this observing campaign is a result of a long and tedious preparatory work done at the Département d'Astrophysique of the Nice University. We acknowledge the efforts of A. Robini, J.-F. Manigault and M. Azouit in the development of GSM and of the mast equipment, and the help of the staff of the "Observatoire de la Cote d'Azur". On–site preparation of GSM campaign at Paranal was organized and implemented by ESO under the supervision of M. Sarazin. We are indebted to Francisco Gomez for helping with observations during the second half of the mission.

Financial support came essentially from INSU , CNRS and MENRT for development of GSM experiment , and from ESO for this measurement campaign.

References

Avila R. et al., 1997, J. Opt. Soc. Am. A 14,3070
Berio P. et al., 1997, J. Opt. Soc. Am. A 14, 114
Borgnino J., 1990, Appl. Opt. 29, 1863.
Buscher D.F. et al., Appl. Opt. 34, 1081
Colavita M.M. et al., 1987, Appl. Opt. 26, 4106
Conan R. et al., 1998, Proc. ESO, Topical Meeting on Astronomy with Adaptive Optics, Present results and future programs. Sonthofen
Davis J. et al., 1995, MNRAS 273, L53
Fried D.L., 1982, J. Opt. Soc. Am. 72, 52
Mariotti J.M., Di Benedetto G.P., 1984, Proc. IAU colloq. 79, 257
Martin F. et al., 1994, A&AS 108, 173
Martin F., Tokovinin A., Ziad A., Conan R., Borgnino J., Avila R., 1998a, GSM measurement campaign at La Silla (August 26th-September 20th ,1997), ESO report VLT-TRE-UNI-17440-0005
Martin F. et al., 1998b, A&A 336, L49
Rigaut F. et al., 1991, A&A 250, 280
Roddier F. et al., 1982, J. Optics (Paris) 13, 263
Sarazin M., 1997, Proc. SPIE 3125, 366
Sarazin M., Roddier F., 1990, A&A 227, 294
Takato N., Yamaguchi I., 1995, J. Opt. Soc. Am. A 12, 958
Tokovinin A., Kornilov V.,Conan R., Ziad A., Martin F. et al., 1998a, Report on the Maydanak site testing campaign in July 1998, INTAS-96-0367-Progress report N° 1.
Tokovinin A.A. et al., 1998b, Proc. SPIE 3353, 1155
Vernin J., Muñoz-Tuñon C., 1992, A&A 257, 811
Ziad A. et al., 1994, A&A 282, 1021
Ziad A. et al., 1999, From Grating Scale Monitor to Generalized Seeing Monitor,submitted to Appl. Opt.

M noire original

J. Optics (Paris), 1977, vol. 8, n° 5, pp. 319-326

LABORATOIRE D'ASTROPHYSIQUE DE L'I.M.S.P.

Parc Valrose, F 06034 Nice Cedex (France)

ANALYSE STATISTIQUE DES DÉFORMATIONS ALÉATOIRES D'UNE SURFACE D'ONDE DUES A LA TURBULENCE ATMOSPHÉRIQUE AU VOISINAGE DU SOL

I. — Exposé de la méthode, Premiers résultats

J. BORGNINO, F. MARTIN

MOTS CLÉS :

Turbulence atmosphérique
Test de Foucault

KEY WORDS :

Atmospheric turbulence
Foucault test

**Statistical analysis of wavefront random deformations
oduced by atmospheric turbulence near the ground :
— *Description of the method. First results***

SUMMARY : A method for analysing random phase perturbations
wave surface impinging on the entrance pupil of an astronomical
servation instrument (reflector or refractor) is given. These
perturbations are observed by a Foucault test looking at the pupil
through a diaphragm, the diameter of which, $\Delta\theta$, is a few arc second ;
s diaphragm is put at the focus of the instrument pointed in the
ection of the solar limb. Simultaneous photographs of the pupil
...ough two diaphragms are necessary to measure the intercorre-
lation of the observed perturbations, leading to turbulent energy
ofile (versus altitude) by a triangulation method.
Two kinds of spatial frequency filtering are effected by the dia-
ragms : the former is the diffraction one (mostly important when
$\Delta\theta$ is small), the latter is a wavefront integration effect (mostly
portant when $\Delta\theta$ is large) ; therefore an optimisation of $\Delta\theta$ is
cessary. At last, altitude is measured for the detected turbulent
er, and the resolution of the method is given.

RÉSUMÉ : On propose une méthode permettant l'étude des déformations aléatoires des surfaces d'onde arrivant sur la pupille d'entrée d'un instrument d'observation astronomique (télescope ou réfracteur). Ces défauts sont mis en évidence par un test de Foucault réalisé en observant celle-ci à travers un diaphragme de quelques secondes d'arc placé au foyer de l'instrument d'observation pointant en direction du bord solaire. Des photographies simultanées de la pupille à travers deux diaphragmes permettent de déterminer l'intercorrélation des défauts observés, ce qui peut conduire à des profils de l'énergie turbulente avec l'altitude par une méthode de triangulation. On montre que les diaphragmes effectuent deux types de filtrage des fréquences spatiales observées sur la pupille : l'un dû à la diffraction (d'autant plus important que le diamètre est petit) et l'autre ayant pour origine un effet d'intégration des surfaces d'ondes (d'autant plus important que le diamètre des diaphragmes est grand). Un compromis entre ces deux types de filtrage doit donc être réalisé. On indique pour terminer l'altitude des couches turbulentes mises en évidence ainsi que la résolution de la méthode.

INTRODUCTION

Les méthodes actives utilisées pour l'étude de la couche limite planétaire sont essentiellement des méthodes faisant appel aux *RADAR*, *SODAR* (*) et *LIDAR* (**). Elles sont toutes basées sur le même principe : la rétrodiffusion des micro-ondes électromagnétiques ou des ondes acoustiques résultant des fluctuations d'indice produites par les variations locales, de températures, du taux de vapeur d'eau et de la vitesse du vent.

Depuis les travaux de Mac Allister *et al.* [1, 2] et Little [3] les techniques de sondages par *SODAR* ont connu un grand développement dans divers domaines. En ce qui concerne la physique de la basse atmosphère ces techniques ont permis une meilleure interprétation des mesures réalisées *in situ* et l'utilisation de *SODAR DOPPLER* est actuellement un moyen privilégié d'analyse de la dynamique des phénomènes. En ce qui concerne ce type de sondage, le lecteur intéressé

(*) *SODAR*, de SOund Detection And Ranging.
(**) *LIDAR* de LIght Detection And Ranging.

pourra se reporter aux exposés de synthèse de Béran *et al.* [4] et de Aubry [5].

Parallèlement, l'utilisation de radars pulsés haute puissance permet l'étude des structures turbulentes jusqu'à des altitudes élevées (30-35 km). En ce qui concerne la basse atmosphère et compte tenu de la haute résolution possible, ce type de radar est particulièrement bien adapté à l'étude de la variation temporelle, de la stratification atmosphérique, des ondes de gravités et des instabilités en fonction de l'altitude (Ottersten *et al.* [6]).

L'utilisation de radar et sodar doppler en configuration monostatique ou bistatique permet l'investigation du champ du vecteur vitesse du vent.

Le domaine d'emploi des *LIDAR* semble plus orienté vers les études de pollution atmosphérique compte tenu des longueurs d'onde utilisées qui sont mieux adaptées à la détection de très petites particules en suspension dans l'atmosphère (Ligda [7], Hamilton [8]). Collis *et al.* [9] ont pu aussi à l'aide de *LIDAR* déterminer des profils verticaux de température.

Pour ce qui est des méthodes passives d'investigation de la basse atmosphère, et en particulier de la couche limite superficielle elles consistent généralement en des mesures *in situ* : capteurs de température, de pression, de taux de vapeur d'eau, etc..., ces capteurs étant portés par des tours, des ballons, des avions.

Par des méthodes passives, purement optiques, deux auteurs seulement (Bystrova *et al.* [10] et Hufnagel [11]) ont à notre connaissance tenté de localiser dans la basse atmosphère les inhomogénéités responsables du phénomène d'agitation en utilisant respectivement comme source lumineuse le bord solaire et le bord lunaire. Ces inhomogénéités (de température essentiellement) créent des défauts de phase pour l'onde arrivant au sol ; l'examen de ces défauts doit permettre de déterminer notamment leur altitude, leur vitesse de déplacement, ainsi que des constantes de structure caractéristiques.

Ces travaux ne semblent pas avoir été poursuivis et tout au moins pour le bord lunaire, ils sont restés au stade de la simulation.

DESCRIPTION GÉNÉRALE DE LA MÉTHODE

Dans tout ce qui suit on se placera dans le cadre de l'approximation géométrique. A cette approximation, les déformations subies par une onde plane traversant une couche atmosphérique se retrouvent pratiquement inchangées au sol. Ceci revient à dire que si l'on appelle $\phi(\mathbf{f})$ la densité spectrale spatiale des fluctuations de phase introduite par la traversée de la couche et $W(\mathbf{f})$ la densité spectrale des fluctuations de phase produites au sol, on a :

$$W(\mathbf{f}) = \phi(\mathbf{f}) ;$$

dans ces expressions f de composantes f_x et f_y représente une fréquence spatiale dans le plan horizontal au sol. On retrouve aisément ce résultat comme cas limite des résultats de Tatarski [12] obtenus à partir de la théorie de Fresnel de la diffraction ; selon cet auteur $W(\mathbf{f}) = \phi(\mathbf{f}) \cos^2 \pi\lambda h f^2$ et, dans le cas où les fréquences spatiales caractéristiques sont très faibles devant le produit λh (approximation géométrique : $f^2 \ll 1/\lambda h$) on retrouve bien $W(\mathbf{f}) = \phi(\mathbf{f})$. Cette hypothèse est tout-à-fait justifiée dans notre cas compte tenu des fréquences spatiales, longueurs d'onde et altitudes de couches intervenant dans le phénomène étudié ; par exemple pour $\lambda = 0{,}5\ \mu$, $h = 100$ m et $f = 0{,}2\ \text{cm}^{-1}$ on obtient $f^2 \lambda h \simeq 1/50$.

Supposons maintenant que l'on pointe une lunette astronomique sur le soleil et que l'on observe la pupille d'entrée de celle-ci à travers un diaphragme de quelques secondes d'arc, placé sur le bord de l'image solaire ; on observe en chaque point de la pupille un assombrissement quasi proportionnel à la pente des défauts de la surface d'onde dans une direction perpendiculaire au bord solaire. Il s'agit d'une méthode de Foucaultage transformant les défauts de phase de l'onde arrivant sur la pupille en variations d'éclairement. Ces défauts de phase sont en fait produits par la somme de tous les défauts de phase introduits par la traversée de chaque couche turbulente atmosphérique.

Si l'on observe maintenant la même pupille à travers deux diaphragmes toujours placés sur le bord solaire, l'intercorrélation des défauts observés doit permettre de remonter au profil de la turbulence avec l'altitude. Il s'agit alors d'une méthode de triangulation par corrélation spatioangulaire analogue à celle utilisée pour la localisation des couches turbulentes atmosphériques responsables de la scintillation stellaire (Rocca *et al.* [13]).

1. — Observation à travers un diaphragme

Examinons sur la *figure 1* le schéma de principe. Sur cette figure, le soleil (S) a été représenté dans le plan S, et α est son diamètre apparent, soit 32′.

Le plan (Ox, Oy) contient la pupille d'entrée (P) de l'instrument et le plan (OX, OY) est le plan focal de cet instrument dans lequel se trouve l'image (s) du soleil.

Considérons le cas théorique *(figure 1(a))* où l'onde issue du point A du bord solaire se propage sans perturbation (absence de toute turbulence) ; une onde plane Σ, parallèle à la pupille (P) arrive sur celle-ci et l'image géométrique du point A est en O'.

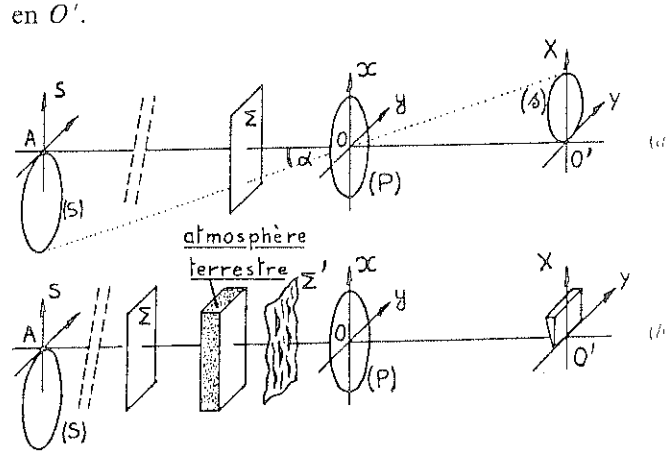


FIG. 1. — (a) *L'onde Σ issue du point A situé à l'infini arrive sur (P) sans perturbation.* (b) *L'onde Σ se déforme par traversée de l'atmosphère terrestre et c'est l'onde perturbée Σ′ qui arrive sur (P).*

Si pour isoler cette onde on plaçait au point O' un diaphragme de diamètre très petit, la pupille, vue à travers ce diaphragme apparaîtrait comme uniformément éclairée.

Si on considère maintenant le cas où l'onde Σ issue du point A subit des perturbations à la traversée de l'atmosphère terrestre *(figure 1(b))*, l'onde Σ' qui arrive sur la pupille présente des déformations liées aux fluctuations d'indice dans les couches atmosphériques traversées. Ces déformations peuvent être mises en évidence par foucaultage, c'est-à-dire en plaçant en O' un couteau rectiligne dont l'arête est parallèle à l'image du bord solaire en ce point. En fait dans la réalité, pour des raisons qui apparaîtront plus loin, ce n'est pas un couteau qui est placé en O' mais un diaphragme circulaire de diamètre angulaire égal à $\Delta\theta$ et l'on observe alors sur la pupille la superposition de toutes les surfaces d'onde dont la direction de propagation moyenne est contenue dans un cône d'ouverture $\Delta\theta$ et d'axe Oz. Si on photographie la pupille (P) dans ces conditions en plaçant un appareil photographique derrière le diaphragme on obtient des clichés tel que celui représenté sur la *figure 2.*

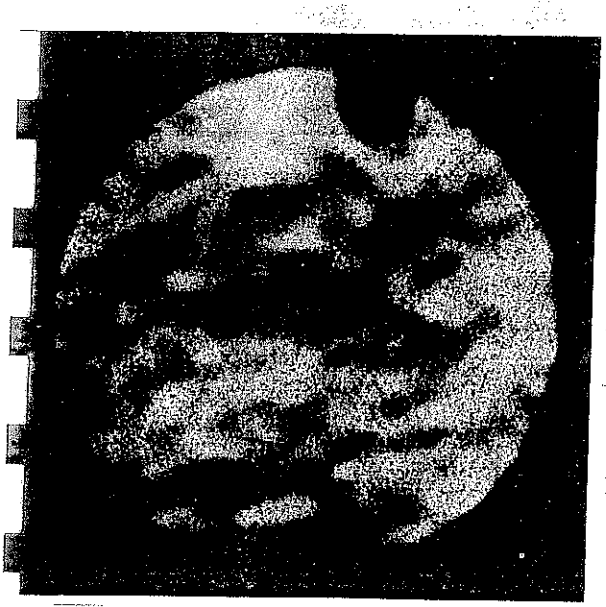


FIG. 2. — *Cliché d'ombres volantes solaires réalisé au réfracteur coudé de l'observatoire de Nice (temps de pose = 1 ms).*

Ces clichés présentent le même aspect global que ceux correspondants aux ombres volantes stellaires résultant le phénomène de scintillation et étudié photographiquement par Martin *et al.* [14]; aussi par analogie, dans la suite, nous parlerons d'ombres volantes solaires bien que ces deux phénomènes soient fondamentalement différents.

L'examen à priori de tels clichés appelle les remarques suivantes :

— les dimensions caractéristiques des structures aléatoires mises en évidence sont de l'ordre de quelques centimètres, le diamètre du cliché correspondant à 4 cm ;

— ces structures montrent un allongement très net dans la direction parallèle au bord solaire.

Afin de préciser ces points, nous avons déterminé de façon numérique les autocorrélations de tels clichés suivant deux directions perpendiculaires : l'une parallèle et l'autre perpendiculaire au bord solaire. Les résultats correspondants sont développés plus loin.

2. — Observation à travers deux diaphragmes

L'observation simultanée à travers deux diaphragmes D_1 et D_2 va permettre comme nous l'avons dit d'effectuer des corrélations spatioangulaires. Les deux diaphragmes sont placés sur $O'Y$ et symétriquement par rapport à O' comme indiqué sur la *figure 3*, leur distance angulaire étant égale à $\theta = D_1D_2/F$ *(figure 4)*. Examinons ce qui se passe alors sur cette figure représentant le dispositif optique de principe de la manipulation.

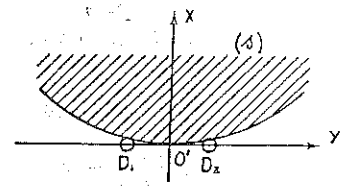


FIG. 3. — *Position des diaphragmes sur le bord solaire.*

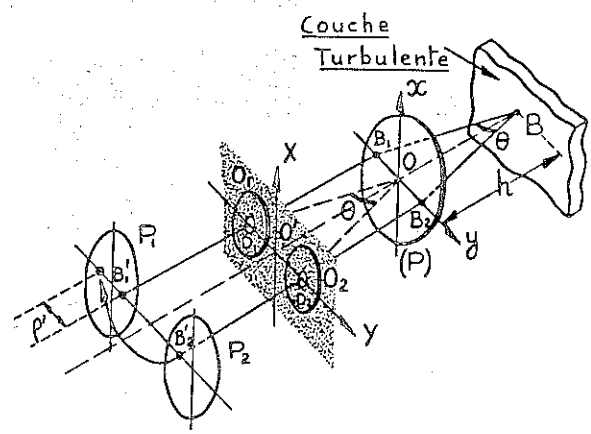


FIG. 4. — *Schéma optique de principe.*

Les deux lentilles O_1 et O_2 placées dans le même plan que les deux diaphragmes D_1 et D_2 donnent de la pupille (P) les images séparées P_1 et P_2. Celles-ci sont ensuite enregistrées simultanément sur un film photographique placé dans le plan focal des lentilles dont la distance focale est très faible devant la distance focale $F = OO'$ de l'instrument. Des exemples de clichés obtenus dans ces conditions sont montrés *figure 5.* On notera sur cette figure la chute de la corrélation entre deux clichés simultanés lorsque la distance angulaire θ des deux diaphragmes augmente. Ceci est dû au fait que les ensembles de couches atmosphériques traversées par les surfaces d'ondes observées sur la pupille sont d'autant plus différents que θ est grand.

Les images P_1 et P_2 correspondent respectivement aux rayons tombant sur la pupille avec des directions voisines de celles définies par OD_1 et OD_2 et faisant entre elles l'angle θ.

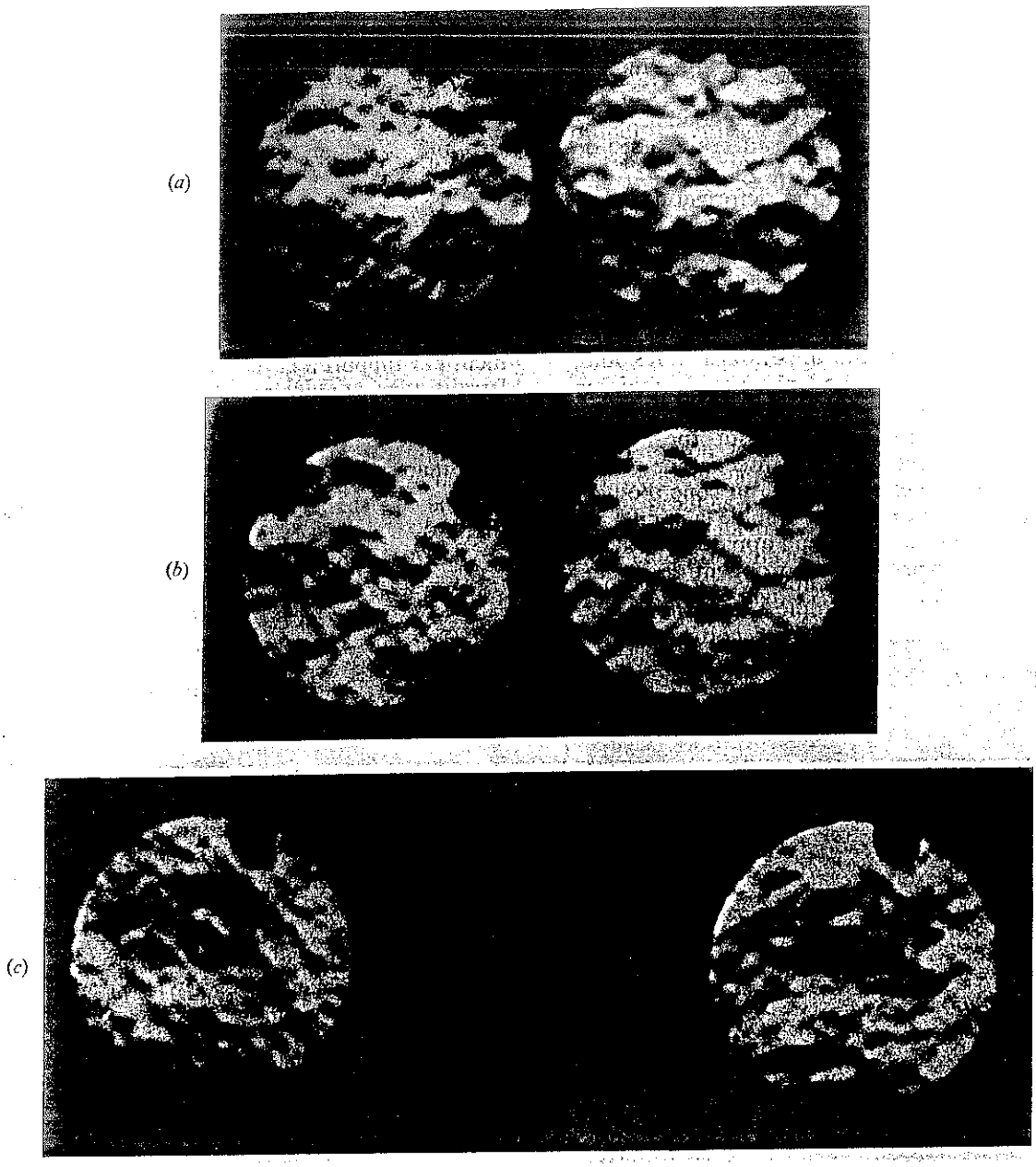


FIG. 5. — *Photographie de la pupille (P) à travers deux diaphragmes D_1 et D_2. Durée d'exposition* : 1 ms. *La distance angulaire θ vaut* : (a) 80″, (b) 160″, (c) 320″.

Considérons maintenant une couche turbulente très mince, située à une altitude h_0 à la verticale de la pupille (P) et isolons dans cette couche un défaut de phase localisé en B ; celui-ci se traduira par des défauts d'éclairement localisés en B_1' et B_2' sur les images P_1 et P_2 de la pupille vue à travers les deux diaphragmes.

B_1' et B_2' sont les images à travers O_1 et O_2 des points B_1 et B_2 autour desquels se « projettent » le défaut de phase localisé en B. La distance $B_1B_2 = \rho$ est déterminée à partir du décalage ρ' mesuré entre B_1' et B_2' sur les clichés de P_1 et P_2 en tenant compte des grandissements optiques.

Dans la suite on parlera donc de « dédoublement » sur la pupille, des ombres volantes, celui-ci n'ayant de sens évidemment que si on a isolé deux directions privilégiées OD_1 et OD_2 en interposant les deux diaphragmes D_1 et D_2.

Si on considère maintenant l'ensemble de la couche turbulente située à l'altitude h_0, chaque défaut de phase donne lieu au même dédoublement sur la pupille. Comme l'on connaît θ, on peut remonter à l'altitude h_0 de la couche par la relation $\rho_0 = \theta h_0$ en déterminant ρ_0 ; pour cette détermination on calcule la fonction d'intercorrélation des clichés P_1 et P_2. La nature aléatoire du phénomène demande nécessairement la réalisation d'un grand nombre d'intercorrélations donc d'un grand nombre de clichés afin d'obtenir par moyenne d'ensemble une bonne estimation de ρ_0' en supposant la stationnarité du phénomène.

Dans le cas de l'existence de plusieurs couches turbulentes, chacune d'elles produit un dédoublement proportionnel à son altitude et intervient avec un poids fonction de l'intensité de la turbulence, donc

des défauts de phase qu'elle produit. Si l'on a affaire à une répartition continue de l'énergie turbulente avec l'altitude, on ne pourra plus parler d'altitudes de couches mais il faudra plutôt évoquer le concept de profil de turbulence, c'est-à-dire qu'à chaque altitude h il faut associer une grandeur $P(h)$ caractérisant les fluctuations d'énergie turbulente pour cette altitude. $P(h)$ est la fonction intéressante à déterminer physiquement et c'est elle que nous baptiserons dans la suite profil de la turbulence.

3. — Fondement théorique

Soit $AC(\rho)$ l'autocorrélation spatiale des défauts de phase observés sur la pupille d'entrée de l'instrument, ρ étant le décalage spatial.

Examinons tout d'abord pour simplifier ce qui se passe dans le cas théorique d'une couche turbulente unique, très mince, située à une altitude h_0 à la verticale du télescope.

$P(h)$ s'écrit alors :

$$P(h) \simeq \delta(h - h_0)$$

δ étant la fonction de Dirac, une altitude h correspond à un décalage spatial dans le plan de la pupille $\rho = \theta h$. Pour θ fixé $P(h)$ s'exprime en fonction de ρ par :

$$P(\rho) \simeq \delta(\rho - \rho_0) \quad \text{avec} \quad \rho_0 = \theta h_0 .$$

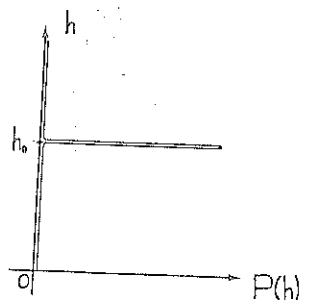


FIG. 6. — *Profil théorique de la turbulence $P(h)$ en fonction de l'altitude h, dans le cas d'une couche turbulente très mince, assimilable à une fonction de Dirac.*

$P(h)$ et $P(\rho)$ sont représentés sur la *figure 6*. Soit $IC(\rho)$ l'intercorrélation des défauts de phase observés sur deux pupilles fictives qui ont pour image P_1 et P_2 dans les lentilles O_1 et O_2, on a alors :

$$IC(\rho) = AC(\rho) * \delta(\rho - \rho_0) = AC(\rho - \rho_0)$$

où le signe $*$ représente une convolution.

C'est-à-dire que dans ce cas théorique idéal, l'intercorrélation cherchée ne serait pas autre chose que l'autocorrélation $AC(\rho)$ décalée d'une quantité ρ_0 proportionnelle à l'altitude de la couche.

Dans le cas réel, le profil $P(\rho)$ peut être de forme quelconque et l'intercorrélation $IC(\rho)$ que l'on souhaite déterminer est donnée par

$$IC(\rho) = AC(\rho) * P(\rho) .$$

Pour avoir la meilleure détermination possible de $P(\rho)$, il est nécessaire d'avoir une résolution qui soit la plus grande possible, c'est-à-dire une autocorrélation $AC(\rho)$ la plus étroite possible. La largeur de cette autocorrélation est liée à deux causes :

— *d'une part* la taille caractéristique des défauts de phase observés,

— *d'autre part*, comme nous allons le voir, à l'effet de filtrage passe bas (en fréquence spatiale) propre à la méthode utilisée. Cet effet qui ne peut être réduit autant qu'on le désire constitue donc une limitation importante pour la résolution de la méthode.

CHOIX DES PARAMÈTRES. LIMITATIONS

Nous allons voir que le choix de $\Delta\theta$, diamètre angulaire des diaphragmes placés sur le bord solaire, est en fait très critique car il résulte d'un compromis entre les deux types de filtrage de fréquence spatiale qu'il réalise, à savoir ce que nous appellerons dans la suite « filtrage angulaire » et « filtrage dû à la diffraction ».

1. — Filtrage angulaire

Le fait d'observer sur la pupille la superposition des surfaces d'ondes correspondant à un cône d'ouverture $\Delta\theta$ se traduit par une intégration de tous les défauts correspondants à celles-ci, d'où le nom de filtrage angulaire. Ainsi un défaut ponctuel situé à une altitude h apparaîtrait sur la pupille comme une tache de diamètre $\Delta D' = h.\Delta\theta$; il y a donc un étalement des défauts dû au fait que le diaphragme ne peut être ponctuel mais présente un certain diamètre. Du point de vue de la taille des éléments observés sur la pupille, seuls les éléments de taille supérieure ou égale à $h\,\Delta\theta$ seront observables et on peut définir une fréquence de coupure par

$$f_a = \frac{1}{h\,\Delta\theta} .$$

Seules les fréquences spatiales $f \leqslant f_a$ seront vues sur la pupille, d'où un élargissement pour les fonctions d'autocorrélation comme nous l'avons déjà dit.

2. — Filtrage dû à la diffraction

Si Δd est le diamètre du diaphragme, celui-ci ne permet d'observer sur la pupille (P) que des détails dont la séparation angulaire $\Delta\alpha$ est telle que

$$\Delta\alpha \geqslant \frac{1{,}2\,\lambda}{\Delta d} ;$$

$\Delta\alpha$ correspond à des éléments de taille $\Delta D = F.\Delta\alpha$ sur (P) et l'inégalité ci-dessus s'écrit :

$$\Delta D \geqslant \frac{1{,}2\,\lambda}{\Delta d/F} \quad \text{soit} \quad \Delta D \geqslant \frac{1{,}2\,\lambda}{\Delta\theta} .$$

Le diaphragme de diamètre angulaire $\Delta\theta$ réalise un filtrage des fréquences spatiales dans le plan focal de l'objectif (P) et son diamètre est tel qu'il ne permet d'observer sur celui-ci que les éléments de taille

$\Delta D \geqslant 1{,}2\,\lambda/\Delta\theta$. Là encore on peut définir une fréquence de coupure

$$f_d = \frac{1}{\Delta D} = \frac{\Delta\theta}{1{,}2\,\lambda}$$

et les fréquences spatiales observables sont telles que $f \leqslant f_d$.

Compte tenu de ces deux types de filtrage, on voit que si $\Delta\theta$ est trop grand, $f_d > f_a$, et l'ensemble du système est limité par le filtrage angulaire. A l'inverse, si $\Delta\theta$ est trop petit, $f_d < f_a$ et la limitation vient de la diffraction.

Le meilleur compromis consiste évidemment à prendre $f_a = f_d$ c'est-à-dire

$$\frac{1}{h\,\Delta\theta} = \frac{\Delta\theta}{1{,}2\,\lambda} \quad \text{d'où} \quad (\Delta\theta)^2 = \frac{1{,}2\,\lambda}{h}.$$

Nous avons tracé sur la *figure 7* un réseau de courbes mettant en évidence les effets de ces deux types de filtrage en portant en ordonnée le diamètre ΔD des éléments observables sur la pupille et en abscisse le diamètre angulaire $\Delta\theta$ des diaphragmes. Pour une couche située à une altitude h le meilleur compromis correspond à l'intersection de la droite $h\,\Delta\theta$ avec l'hyperbole $1{,}2\,\lambda/\Delta\theta$.

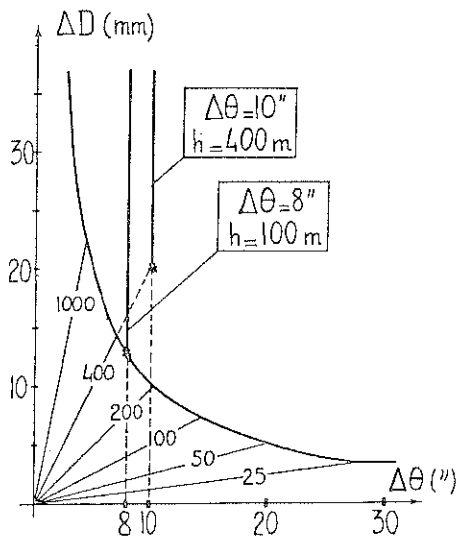


FIG. 7. — *Diamètre des plus petits éléments observables sur la pupille en tenant compte :*
— *du filtrage angulaire (droites d'équation $h\,\Delta\theta$ tracées pour différentes altitudes indiquées en mètres),*
— *du filtrage dû à la diffraction (hyperbole $1{,}2\,\lambda/\Delta\theta$ tracée pour $\lambda = 0{,}5\,\mu$).*
Les ordonnées des demi-droites en traits gras donnent ces diamètres dans les deux cas suivants : 1) Couche turbulente à 400 m, $\Delta\theta = 10''$ (limitation par le filtrage angulaire) ; 2) Couche turbulente à 100 m, $\Delta\theta = 8''$ (limitation par la diffraction).

3. — Choix des paramètres

Si D est le diamètre de la pupille de l'instrument d'observation, la hauteur maximale, h_{max}, des défauts observables est liée à l'écartement des diaphragmes par la relation $D = 0.h_{max}$.

Par exemple en fixant $h_{max} = 500$ m on obtient la valeur minimale de θ soit $\theta_m = D/h_{max} = 160''$.

Si on calcule à l'aide de la relation ci-dessus la valeur $\Delta\theta$ correspondante, on trouve, pour $\lambda = 0{,}5\,\mu$, $\Delta\theta \simeq 10''$.

C'est de cette façon que nous avons procédé pour le choix des paramètres c'est-à-dire :

— fixation à priori d'une altitude maximum h_{max},
— détermination de θ_m et du diamètre $\Delta\theta$ des diaphragmes en fonction de ce h_{max}.

Cette façon d'opérer, liée à une altitude h_{max} fixée à priori constitue évidemment un inconvénient, mais seule une méthode de traitement en temps réel permettrait un ajustement plus convenable des paramètres ; en procédant comme nous le faisons, les défauts de phase que nous pouvons localiser sont nécessairement situés à une altitude inférieure à h_{max} et le système est alors automatiquement limité par la diffraction. Pour obtenir les résultats qui vont suivre l'altitude h_{max} a été prise égale à 500 mètres.

PREMIERS RÉSULTATS

Nous indiquons dans ce qui suit les premiers résultats obtenus à partir des clichés réalisés au réfracteur Coudé de l'observatoire de Nice. La méthode de dépouillement des clichés ne sera pas traitée ici ainsi que les problèmes relatifs à ce dépouillement (problèmes de filtrage, erreurs d'estimation, etc...). Ces divers points seront développés en détail dans un second article constituant la deuxième partie de la présente étude (*). Nous indiquerons simplement que le traitement a été effectué au *Centre de dépouillement des Clichés Astronomiques* de l'I.N.A.G. situé à Nice. Ce centre est équipé d'un microphotomètre P.D.S. associé à un ordinateur PDP 1140. Après digitalisation des couples de clichés, les fonctions de corrélation unidimensionnelles sont déterminées soit directement, soit par l'intermédiaire de transformées de Fourier.

1. — Autocorrélations

Nous avons déterminé deux types de fonctions d'autocorrélations :

— les autocorrélations dans une direction perpendiculaire au bord solaire : autocorrélations transverses $C_T(\rho)$,
— les autocorrélations dans une direction parallèle au bord solaire : autocorrélation longitudinale $C_L(\rho)$

Un exemple de ces fonctions d'autocorrélation est donné sur la *figure 8*. La fonction $C_L(\rho)$ est notablement plus large que $C_T(\rho)$, le rapport des largeurs à mi-hauteur de ces deux fonctions étant de l'ordre de 3.

L'élargissement de l'autocorrélation dans une direction parallèle au bord solaire est un effet d'anisotropie introduit par le principe même de la méthode. En effet, si $\varphi(x, y)$ caractérise en chaque point de la pupille (P) la phase de l'onde tombant sur celle-ci on observe sur (P) des fluctuations d'éclairemen

(*) *A paraître* ultérieurement dans la même revue.

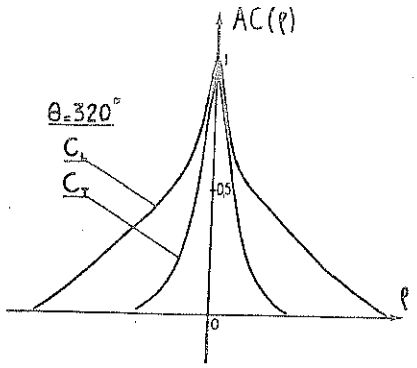


FIG. 8. — *Autocorrélations longitudinales et transverses en fonction du décalage spatial ρ sur la pupille.*

proportionnelles à $\partial\varphi(x, y)/\partial x$. Ceci se traduit par la multiplication par f_x^2 de la densité spectrale des fluctuations de phase au sol $W(f_x, f_y)$ donc par un renforcement dans la direction Ox des ombres volantes solaires observées.

Un effet géométrique introduisant une déformation analogue de ces ombres peut se superposer à celui-ci dans le cas où le système est limité par le filtrage angulaire et où la zone délimitée par le diaphragme sur le bord solaire est de forme allongée.

Les clichés ayant servi à la détermination de ces autocorrélations ont été réalisés dans les conditions suivantes :

— diamètre angulaire des diaphragmes : $\Delta\theta = 8''$,
— temps de pose pour des films peu sensibles et présentant un contraste élevé : $t = 1$ ms.

La résolution en altitude de la méthode est directement liée à la largeur de l'autocorrélation C_L ; en effet les intercorrélations nécessaires à la détermination des altitudes des zones turbulentes sont effectuées dans la direction des deux diaphragmes donc dans une direction parallèle au bord solaire. La largeur à mi-hauteur $(C_L)_{1/2}$, de l'autocorrélation relative à $\theta = 320''$ de la *figure 8* est égale à 6,8 cm ; c'est cette valeur que nous utiliserons ci-après pour calculer la résolution.

2. — Intercorrélations

Les écarts angulaires des diaphragmes pour les clichés traités sont $\theta_1 = 160''$, correspondant au θ_m défini plus haut, et $\theta_2 = 320'' = 2\,\theta_m$; cette dernière valeur a été prise de façon à augmenter la précision sur la détermination de l'altitude des zones turbulentes située à une hauteur inférieure à $1/2\,h_{max} = 250$ m.

Chacune des intercorrélations présentées sur la *figure 9* a été réalisée à partir de vingt couples de clichés analogues à ceux de la *figure 5*.

On constate que les deux maxima des intercorrélations de la *figure 9(a)* sont décalés par rapport à l'origine de quantités $\rho_1 = 1{,}7$ cm et $\rho_2 = 3{,}4$ cm qui sont bien dans le rapport $1/2 = \theta_1/\theta_2$ des écarts angulaires θ_1 et θ_2 des diaphragmes, compte tenu de la relation $\rho = \theta h$. Ceci correspond à une altitude voisine de 22 mètres montrant que le profil de l'énergie turbulente présente un maximum d'énergie à cette altitude-là. Les intercorrélations sont élargies par

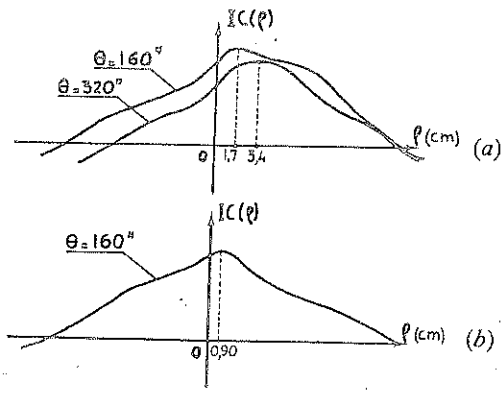


FIG. 9. — *Intercorrélations (en échelle arbitraire) : (a) Pour deux valeurs de la distance angulaire θ des diaphragmes. Les clichés correspondants à ces deux intercorrélations ont été réalisés le même jour à quelques minutes d'intervalle. (b) Intercorrélation correspondant à des clichés réalisés un autre jour.*

rapport aux autocorrélations C_L ce qui traduit une répartition de l'énergie turbulente autour de l'altitude trouvée. En tenant compte de $(C_L)_{1/2}$ et des points où les intercorrélations s'annulent on peut évaluer à une soixantaine de mètres l'épaisseur de la couche turbulente au-dessus du sol. Cette épaisseur est obtenue en retranchant à la valeur de ρ pour laquelle l'intercorrélation s'annule une quantité égale à $(C_L)_{1/2}$. Ceci permet de déterminer grossièrement l'altitude maximum de la zone turbulente dans la limite fixée par l'écartement des diaphragmes.

Deux déterminations ont été faites à partir des courbes de la *figure 9(a)* et des autocorrélations correspondantes ; elles ont donné pour $\theta_1 = 160''$ et $\theta_2 = 320''$, respectivement $h = 62$ m et $h = 54$ m.

Sur la *figure 9(b)* nous donnons une autre intercorrélation réalisée un autre jour et sur laquelle le maximum de turbulence s'observe vers 12 m, pour cet exemple l'épaisseur de la couche turbulente déterminée comme ci-dessus est voisine de 40 m.

Une méthode rigoureuse pour obtenir le profil $P(h)$ (ou $P(\rho)$) de la turbulence consisterait à effectuer une déconvolution sur l'équation

$$IC(\rho) = AC(\rho) * P(\rho)\,.$$

Malheureusement une telle déconvolution, compte tenu du bruit est difficilement réalisable et nous nous sommes limités dans cette première étape à la détermination d'une altitude caractéristique d'une part et à une estimation grossière de l'épaisseur de la zone turbulente d'autre part.

Du point de vue de la résolution en altitude de la méthode, si on considère deux couches distantes de Δh situées à des altitudes h et h' elles donneront respectivement des intercorrélations de décalages ρ et ρ' tels que $\Delta\rho = \rho - \rho' = \theta\,\Delta h$. Ces deux couches ne pourront être séparées que si $\Delta\rho \geqslant (C_L)_{1/2}$ soit

$$\Delta h \geqslant \frac{(C_L)_{1/2}}{\theta}\,.$$

Pour l'exemple donné où $\theta = 320''$ et $(C_L)_{1/2} = 6{,}8$ cm on obtient une résolution en altitude Δh de l'ordre de 40 m.

Si on examine à postériori les courbes de la *figure 7* on s'aperçoit que pour une couche située à 22 m le meilleur compromis entre les filtrages est obtenu pour des diaphragmes de diamètre angulaire voisin de 30″. Le choix qui a été fait (8″) pour les diamètres des diaphragmes utilisés s'avère donc mauvais, compte tenu de l'altitude de la zone turbulente mise en évidence. L'ensemble de la manipulation a été fortement limité par le filtrage dû à la diffraction lequel n'a pas permis de voir les éléments de taille comprise entre 15 mm et 4 mm, cette dernière valeur correspondant au meilleur compromis. Les fonctions de corrélation ont été notablement élargies et avec un meilleur choix du diamètre des diaphragmes la résolution aurait pu être augmentée de façon importante.

CONCLUSION

Nous avons présenté une méthode de corrélation spatioangulaire permettant de déterminer le centre de gravité de la répartition de l'énergie turbulente avec l'altitude pour les très basses couches. Cette méthode présente l'avantage de détecter les couches turbulentes jusqu'au voisinage du sol. Sa résolution est fortement tributaire du choix des paramètres aussi sommes-nous en train de développer des méthodes de traitement en temps réel utilisant comme capteur, une caméra de télévision ou une ligne de photodiodes, de façon à ajuster convenablement les diamètres et écartements des diaphragmes en fonction des altitudes observées. L'étape consistant à utiliser un film photographique comme récepteur n'a servi qu'à mettre au point la manipulation et à déterminer le jeu des paramètres. Bien qu'il ait été possible de mettre en évidence de cette façon des altitudes caractéristiques, avec la version actuelle de la manipulation il ne saurait être question d'exploiter plus avant les possibilités de celle-ci compte tenu, d'une part des remarques faites ci-dessus, et d'autre part de la longueur du traitement numérique nécessaire pour obtenir des estimations correctes des fonctions de corrélation. Seules les méthodes de traitement en temps réel permettront d'accéder à des grandeurs physiquement intéressantes telles que le profil de la turbulence avec l'altitude et sa comparaison avec des mesures *in situ*, ou la détermination de fonction de structures pour la phase de l'onde arrivant sur la pupille d'un télescope ou d'un réfracteur. Les manipulations décrites dans cet article peuvent aussi être réalisées sur le bord lunaire de façon à se placer dans des conditions de turbulence différentes. Dans ce but une campagne de mesure à l'*Observatoire de Haute-Provence* (10-17 mai 1976) a permis de tester un dispositif utilisant comme capteur une caméra de télévision spéciale à haute sensibilité. Des enregistrements sur magnétoscope d'« ombres volantes lunaires » ont été effectués ; ils permettront de mettre au point le traitement du signal vidéo en vue, ultérieurement, d'une exploitation de celui-ci en temps réel.

* * *

BIBLIOGRAPHIE

[1] MAC ALLISTER (L. G.). — Acoustic sounding of the lower troposphere. *J. Atm. Terr. Phys.*, 1968, *30*, 1439-1440.

[2] MAC ALLISTER (L. G.), POLLARD (J. R.), MAHONEY (A. R.). SHAW (P. J. R.). — A new approach of the study of atmospheric structures. *Proc. IEEE*, 1969, *57*, 579-587.

[3] LITTLE (C. G.). — Acoustic Methods for the remote probing of the lower troposphere. *Proc. IEEE*, 1969, *57*, 571-578.

[4] BERAN (D. W.), HOOKE (W. M.), CLIFFORD (S. F.). — Acoustic echo sounding techniques and their applications to gravity waves, turbulence and stability studies. *Boundary Layer Meteor*, 1973, *4*, 133-153.

[5] AUBRY (M.). — Les sondages Acoustiques de l'Atmosphère, exposé de synthèse présenté à la XVIII[e] Assemblée Générale de *l'U.R.S.I.*, Lima, 1975.

[6] OTTERSTEN (M.), HARDY (K. R.), LITTLE (C. G.). — Radar and Sodar probing of waves and turbulence in statically stable clear air layers. *Boundary Layer Meteor*, 1973, *4*, 47-90.

[7] LIGDA (M. G. H.). — Meteorological observations with LIDAR, in Proc. *World Conf.* Radio Meteorology. *Am. Meteorol. soc.*, Boston, 482-489.

[8] HAMILTON (P. M.). — The use of *LIDAR* in air pollution studies. Air and Wat. Pollut. Int. J., *Pergamon Press*, 1966 *10*, 427-434.

[9] COLLIS (R. T. M.), FERNALD (F. G.), LIGDA (M. G. M.). — Laser radar echoes from a stratified clear atmosphere *Nature* (Lond.), 1964, *203*, 1274-1275.

[10] BYSTROVA (N. V.), DEMIDOVA (A. N.). — Location of atmospheric inhomogeneities distorting the solar limb in clear and cloudy days. *Solnečnye dannye bull.*, 1973, *7*, 3.

[11] HUFNAGEL (R. F.). — Measurement of Atmospheric Turbulence via observations of Instantaneous Optical Blur Functions. *Proceedings* of Agard Conference, Ankara. 1967.

[12] TATARSKI (V. I.). — Wave propagation in a turbulent medium. *Dover*, New York, 1961.

[13] ROCCA (A.), RODDIER (F.), VERNIN (J.). — Detection of atmospheric turbulent layers by spatiotemporal and spatioangular correlation measurement of stellar light scintillation. *J. Opt. Soc. Amer.*, 1974, *64*, 1000-1004.

[14] MARTIN (F.), BORGNINO (J.), RODDIER (F.). — Localisation de couches turbulentes atmosphériques par traitement optique de clichés d'ombres volantes stellaires. *Nouv. Rev. Optique*, 1975, *6*, 15-23.

REMERCIEMENTS. — Nous tenons à remercier F. RODDIER pour les nombreuses et fructueuses discussions qui nous ont permis de mener cette étude à bonne fin.

(Manuscrit reçu le 20 juillet 1976.

Experimental verification of the inertial model of atmospheric turbulence from solar limb motion

J. Borgnino and J. Vernin

Département d'Astrophysique de l'I.M.S.P., Equipe de Recherche Associée No. 669 du CNRS Université de Nice, Parc Valrose, 06034 Nice-Cedex, France

and Observatoire de Nice, Le Mont Gros, B.P. 252, 06007 Nice-Cedex 2, France

(Received 30 January 1978)

A photoelectric apparatus enabled us to obtain new estimates of the longitudinal and transverse correlation functions for the angle-of-arrival fluctuations on the entrance pupil of a solar telescope. The inertial model of turbulence was verified for spatial shifts up to 35 cm. Measurements of the turbulent-layers velocity were taken. The values found for Fried's parameter r_0, the integral $\int C^2_N dh$ of the structure constant for the variations of the refractive index of the air over the thickness of the lower atmosphere, and the root-mean-square fluctuation of the angles of arrival appear to agree with independent estimates.

I. INTRODUCTION

The angle-of-arrival fluctuations on the entrance pupil of a solar telescope may be shown by placing a diaphragm of few seconds of arc over the image of the solar limb obtained t the focus of the instrument and observing the pupil through nis diaphragm.[1–4] In a previous paper,[4] the estimation of the one-dimensional correlation functions for these fluctuations llowed the experimental verification of the inertial model of turbulence for spatial shifts varying from 2 cm up to approximately 10 cm. Values of Fried's seeing parameter r_0, and so of the integral $\int C_N^2\, dh$ of the structure constant for the variations of the refractive index of the air over atmospheric layers for which the altitude is lower than a value of the order of a few hundreds of meters (see Refs. 14, p. 331–334), were deduced and found to be consistent with independent estimates made with the same telescope. These results were obtained using the photographic film that permits the re-

 0030-3941/78/6808-1056$00.50 © 1978 Optical Society of America

cording of two-dimensional information but leads to long and tedious processing when ensemble averages are to be performed.[5]

In the present paper, the sensors used are individual photodiodes making data reduction much easier. A new experimental apparatus is described later. This photoelectric method allows us to present new results in better agreement with theoretical predictions.

II. ONE-DIMENSIONAL AUTOCORRELATION FUNCTIONS—RECALLS

The illumination variations on the pupil of a telescope, observed through a diaphragm placed over an image of the solar limb, can be written,[4] in the geometrical approximation,

$$\Delta E(x,y) = k\partial\varphi(x,y)/\partial y, \tag{1}$$

where $\varphi(x,y)$ is the phase of the wave front perturbed by atmospheric turbulence, x and y are the directions, respectively, parallel and perpendicular to the edge of the sun, and k is a constant dependent on the optical system geometry (shape and size of the diaphragm, focal length of the objective) and the wavelength of the light.

The illumination variations are studied by comparing them to a mean illumination corresponding to an unperturbed wave. In the hypothesis of the inertial model of turbulence, it was proved in Ref. 4 that, for the angle-of-arrival fluctuations observed in the direction perpendicular to the edge of the sun (i.e., the fluctuations of the derivative of the phase in the y direction), the one-dimensional autocorrelation functions, parallel to the edge of the sun (spatial shift = x)—longitudinal autocorrelation function—and perpendicular to the edge of the sun (spatial shift = y)—transverse autocorrelation function—were found, respectively, equal to

$$C_{AAL}(x,0) = 5.73\, r_0^{-5/3}\, x^{-1/3}, \tag{2}$$

and

$$C_{AAT}(0,y) = (2/3)5.73\, r_0^{-5/3}\, y^{-1/3}, \tag{3}$$

where r_0 is the Fried's parameter.[6]

The one-dimensional autocorrelation functions of illumination fluctuations observed on the entrance pupil are deduced immediately from formulas (1), (2), and (3).[4] We obtain

$$C_{EL}(x,0) = 5.73\, k^2\, r_0^{-5/3}\, x^{-1/3} \tag{4}$$

and

$$C_{ET}(0,y) = (2/3)5.73\, k^2\, r_0^{-5/3}\, y^{-1/3}. \tag{5}$$

The estimation of these autocorrelation functions also allows us to evaluate the validity degree of the inertial hypothesis and to calculate Fried's parameter r_0, the constant k being determined from geometrical considerations (see Ref. 4, Appendix: Case of a Circular Diaphragm).

From r_0, the integral of the structure constant C_N^2 of the refractive index of the air over the thickness of the atmosphere traversed, is given by[7]

$$\int C_N^2\, dh = 0.062\lambda^2 \cos\theta r_0^{-5/3} \tag{6}$$

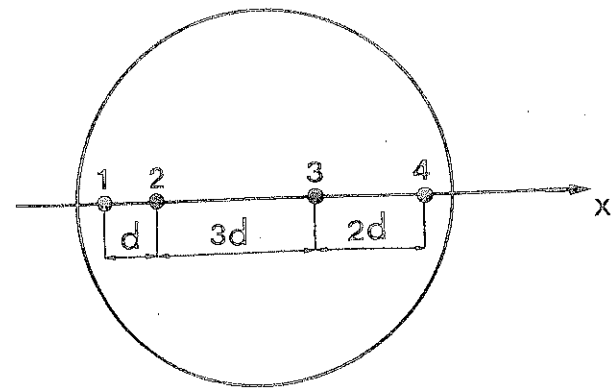


FIG. 1. Arrangement of the photodiodes in the plane of the pupil image. d is the distance between the two nearest photodiodes.

in which λ is the wavelength of the light and θ the angle between the sight line and the zenith.

III. EXPERIMENTAL PROCEDURE

A. New apparatus

The optical part of the experimental device is described in detail in Refs. 3 and 4. Here, the experiments were performed by placing over the image of the edge of the sun observed at the focus of the telescope not circular diaphragms but a rectangular slit of 10 or 20 arc sec by 100 arc sec oriented perpendicularly to the solar limb so that the sun covers approximately one-half of the slit.

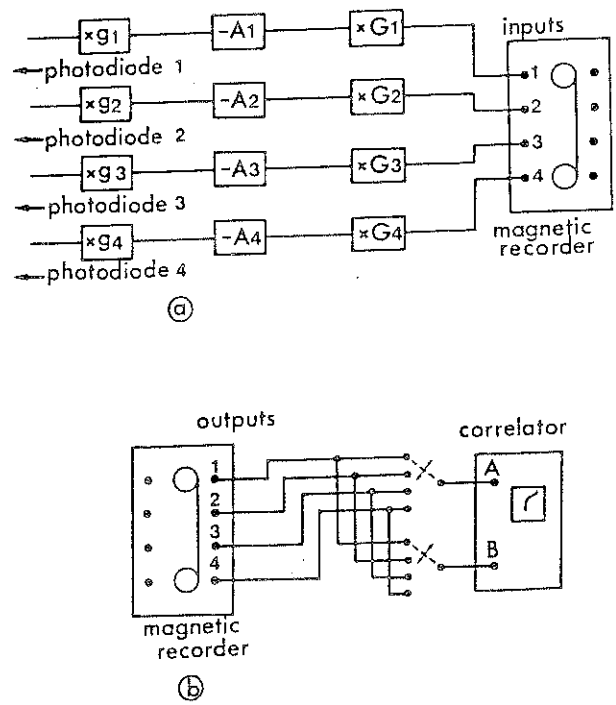


FIG. 2. Electronical apparatus. (a) *Recording.* The signal given by each photodiode is amplified a first time ($\times g_i$), then after subtraction of a constant value ($-A_i$) amplified again ($\times G_i$) and finally recorded. (b) *Processing.* The autocorrelations of the signals 1, 2, 3, and 4 ($x = 0$) are computed successively, then the cross correlation between the signals 1 and 2 ($x = d$), 3 and 4 ($x = 2d$), 2 and 3 ($x = 3d$), 1 and 3 ($x = 4d$), 2 and 4 ($x = 5d$), 1 and 4 ($x = 6d$).

The use of a relatively long slit has two advantages: the first one is to keep out possible saturations for the angle-of-arrival fluctuations, and the second is to eliminate the error on r_0 made in the determination of the parameter k from geometrical considerations in the case of a circular diaphragm, for which k becomes a function of the magnitude of the angle-of-arrival fluctuations.

The image of the telescope pupil observed through the slit is formed in a plane where four photodiodes are placed in a straight line so that the spatial information obtained presents no redundancy (see Fig. 1). It is possible, in this case, to calculate seven values of the spatial autocorrelation function corresponding to spatial shifts $0,1d, \ldots, 6d$, where d is the distance of the nearest photodiodes. For that, it is sufficient to calculate the temporal cross correlations between the signals given by the photodiodes (taken two by two) and to consider the values of these cross-correlations for temporal shifts equal to zero. The electronic part of the apparatus is shown in Fig. 2.

After a first amplification, we subtract a continuous value from the signal given by each photodiode, the difference being amplified again. Then, the signals are recorded simultaneously using a four-track magnetic recorder (FM) and the spatial correlation functions are computed, using a real-time correlator, for a nul temporal delay. The alignment of the photodiodes can be made either parallel to the edge of the sun for the calculation of $C_{EL}(x,0)$ or perpendicular to the edge of the sun for the calculation of $C_{ET}(0,y)$. Moreover, if this alignment is made in the moving direction of the turbulent layer, the velocity of this layer may be measured from the peak position of the temporal cross correlation corresponding to two photodiodes whose distance, studied on the telescope pupil, is well-known[8] (see Fig. 9).

B. Method of analysis

The signal given by each photodiode is proportional to the illumination received. The operations effected on this signal are linear (see Sec. III A or Fig. 2), so the recorded signal corresponding to one photodiode is

$$S_i = \langle S_i \rangle + s_i, \tag{7}$$

where i is an index, which can take discrete values from 1 to 4 according to the photodiode considered, $\langle S_i \rangle$ is the continuous part, and s_i is the fluctuating part of the signal, which is obtained from formula (1) by

$$s_i = k_i \, \partial\varphi/\partial y, \tag{8}$$

where the constant k_i depends not only on the optical system geometry and the wavelength of the light, but also on the various amplifications made along the channel number i.

Let ΔV_i be the maximum variation of the signal corresponding to the maximum variation of the slope (in the direction perpendicular to the solar limb) of the wave front, which can be observed with a slit whose length is a. Formula (8) gives

$$\Delta V_i = k_i \left.\frac{\partial\varphi}{\partial y}\right|_{\max}. \tag{9}$$

In Ref. 4, it was proved that

$$\left.\frac{\partial\varphi}{\partial y}\right|_{\max} = \frac{2\pi a}{\lambda f}, \tag{10}$$

where λ is the wavelength of the light and f the focal length of the telescope. From Eqs. (9) and (10), we obtain

$$k_i = \Delta V_i \lambda f/2\pi a. \tag{11}$$

The continuous part of the signal described by formula (7) will be filtered out before the calculation of the correlation functions, which generally will be written, considering two photodiodes indexed by i and j,

$$C_{ij}(x) = k_i k_j C_{\varphi'}(x) \tag{12}$$

in which $C_{ij}(x)$ is the zero-mean-value signal cross-correlation function taken for a temporal shift equal to zero, $C_{\varphi'}(x)$ is the one-dimensional autocorrelation function for the angle-of-arrival fluctuations observed in the direction perpendicular to the edge of the sun [relations (2) and (3)], x being the distance between the photodiodes i and j. Substituting Eq. (11) into (12), we find

$$C_{ij}(x) = (\lambda^2 f^2/4\pi^2 a^2)\Delta V_i \Delta V_j C_{\varphi'}(x). \tag{13}$$

Taking channel number 1 as a reference, we have

$$\Delta V_i = \Delta V_1 [C_{ii}(0)/C_{11}(0)]^{1/2} \tag{14}$$

and so

$$C_{ij}(x) = (\lambda^2 f^2/4\pi^2 a^2)\, \Delta V_1^2 \times \{[C_{ii}(0)C_{jj}(0)]^{1/2}/C_{11}(0)\}\, C_{\varphi'}(x). \tag{15}$$

Finally, using formulas (2), (3), and (15), we obtain the one-dimensional autocorrelation functions in the directions parallel and perpendicular, respectively, to the solar limb

$$C_{EL}(x) = C_{ij}(x)C_{11}(0)/[C_{ii}(0)C_{jj}(0)]^{1/2} = 5.73\, (\lambda^2 f^2/4\pi^2 a^2)\, \Delta V_1^2\, r_0^{-5/3}\, x^{-1/3} \tag{16}$$

$$C_{ET}(y) = C_{ij}(y)C_{11}(0)/[C_{ii}(0)C_{jj}(0)]^{1/2} = (2/3)5.73\, (\lambda^2 f^2/4\pi^2 a^2)\, \Delta V_1^2\, r_0^{-5/3}\, y^{-1/3}. \tag{17}$$

A least-squares adjustment of the $-\frac{1}{3}$ power law to the experimental results, permits us to verify the validity of the inertial hypothesis. If this verification is effective, it is possible to calculate the multiplicative factors of $x^{-1/3}$ and $y^{-1/3}$ in $C_{EL}(x)$ and $C_{ET}(y)$ and thus to estimate r_0 because λ, f, a, and ΔV_1 are known. $\int C_N^2\, dh$ will be deduced from r_0 using the relation (6).

IV. RESULTS

For the measurements presented in this paper, we have used a 10×100 arc sec slit whose greatest dimension was oriented perpendicularly to the edge of the sun. Before the autocorrelation function was calculated the temporal frequencies lower than 0.1 Hz were filtered out. The importance of this filtering will be examined later. The integration time was made equal to 100 s.

Examples of autocorrelation functions, calculated in the directions parallel and perpendicular to the solar limb, are shown on a log-log scale in Figs. 3–8. We have indicated in these figures the values of r_0 estimated using the method described in Sec. III B and the corresponding values of $\int C_N^2\, dh$, calculated from r_0 taking into account the correction for the angle made with the zenith. The wavelength of the light λ is assumed to be equal to 5×10^{-7} m.

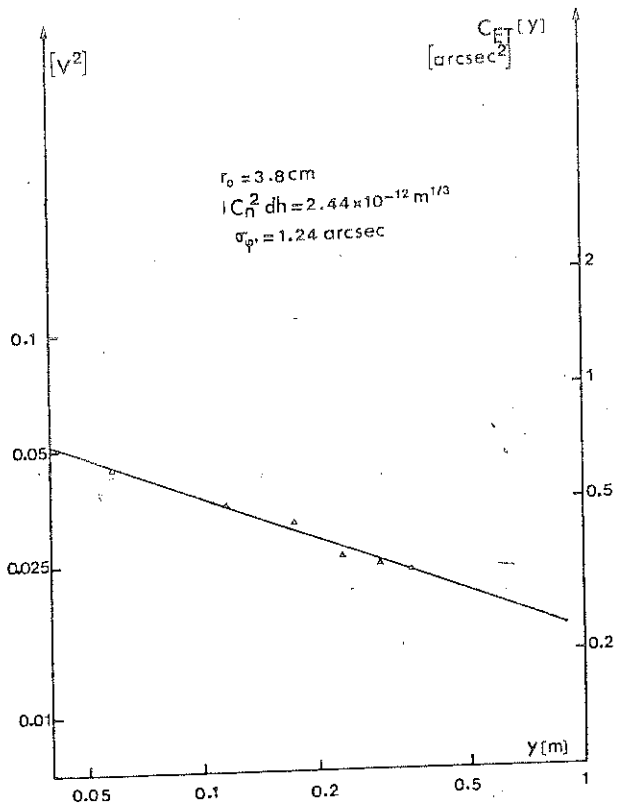


FIG. 3. Transverse autocorrelation of the angle-of-arrival fluctuations. Date, 09/05/77; local time, 10H52′. Correlation coefficient $r = 0.99$ — (▲, experimental points). Slope of the straight line is -0.37. $\sigma_{\varphi'}$ is the root-mean-square fluctuation of the angles of arrival. The unit indicated on the left scale is a voltage from a correlator.

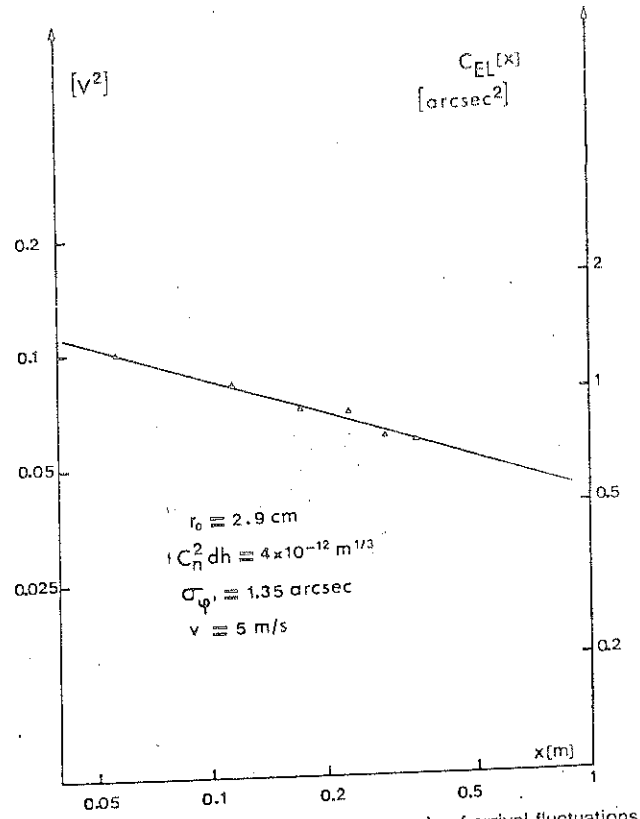


FIG. 4. Longitudinal autocorrelation of the angle-of-arrival fluctuations. Date, 09/05/77; local time, 11H15′. Correlation coefficient $r = 0.99$ — (▲, experimental points). Slope of the straight line is -0.31. $\sigma_{\varphi'}$ is the root-mean-square fluctuation of the angle of arrival; v is the velocity of the turbulent layer. The unit indicated on the left scale is a voltage from a correlator.

These results appear to be in good agreement with the theoretical expressions. Indeed, the experimental points are fitted on a log-log scale by straight lines whose slopes range from -0.37 to -0.31, the inertial model of turbulence providing a slope of -0.33 [relations (16), and (17)]. It will be observed that the correlation coefficient r is always greater than 0.98. Our results are thus consistent with the inertial hypothesis for spatial shifts up to approximately 35 cm. We have also indicated in the figures the root mean square $\sigma_{\varphi'}$ of the angle-of-arrival fluctuations.

Furthermore, when the photodiode alignment was made in the moving direction of the turbulent layer, the velocity v of this layer was measured using the method described in detail in Fig. 9.

In summary, we can say that the inertial model of turbulence is well verified up to 35 cm in the cases presented in Figs. 3–8. Exceptions will be discussed in Sec. V.

V. LOW-FREQUENCY FILTERING

The use of the photographic film as a sensor permitted the verification of the inertial model of turbulence in a spatial range lying between 2 and approximately 10 cm. In this case, all the spatial frequencies lower than the inverse of the length L of the scans ($L = 20$ cm) were filtered out[5] and this fact severely restricted the verification of the model to the spatial shifts much lower than 20 cm.

For the results shown in this paper, the calculation of the

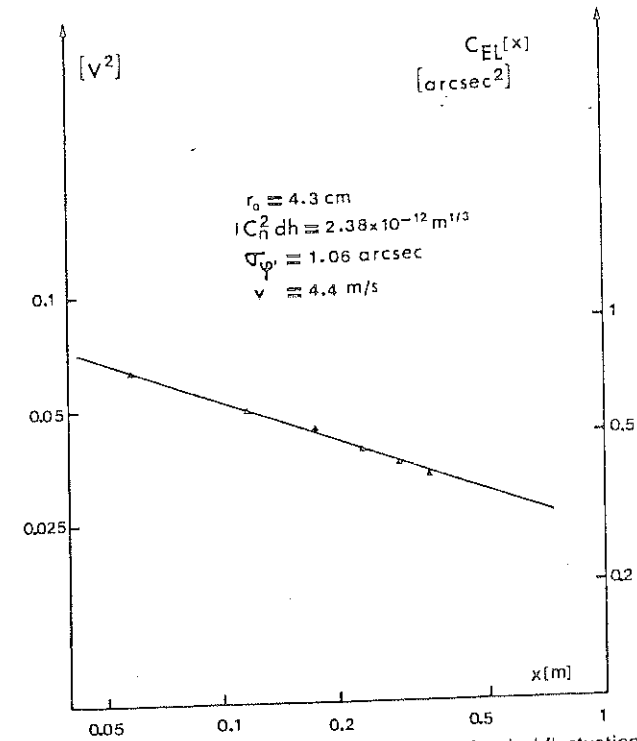


FIG. 5. Longitudinal autocorrelation of the angle-of-arrival fluctuations. Date, 09/05/77; local time, 12H17′. Correlation coefficient $r = 0.998$ — (▲, experimental points). Slope of the straight line is -0.35; $\sigma_{\varphi'}$ is the root-mean-square fluctuation of the angles of arrival; v is the velocity of the turbulent layer. The unit indicated on the left scale is a voltage from a correlator.

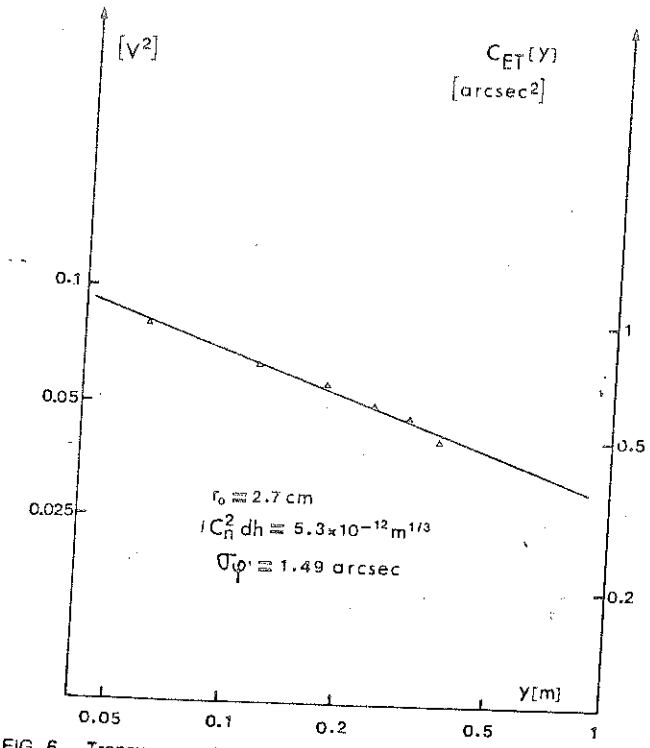


FIG. 6. Transverse autocorrelation of the angle-of-arrival fluctuations. Date, 09/05/77; local time, 12H28′. Correlation coefficient $r = 0.993$ — (▲, experimental points). Slope of the straight-line is −0.36. $\sigma_{\varphi'}$ is the root-mean-square fluctuation of the angles of arrival. The unit indicated on the left scale is a voltage from a correlator.

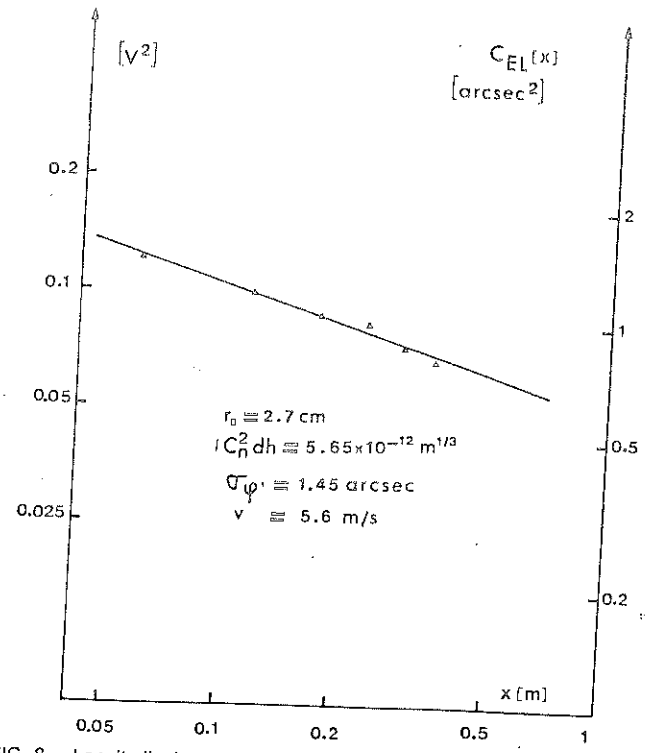


FIG. 8. Longitudinal autocorrelation of the angle-of-arrival fluctuations. Date, 09/05/77; local time, 13H54′. Correlation coefficient $r = 0.99$ — (△, experimental points). Slope of the straight-line is −0.327; $\sigma_{\varphi'}$ is the root-mean-square fluctuation of the angles of arrival; v is the velocity of the turbulent layer. The unit indicated on the left scale is a voltage from a correlator.

autocorrelation functions is made after filtering out the temporal frequencies lower than a frequency cutoff $\nu_c = 0.1$ Hz. Assuming the approximation of "frozen-turbulence"

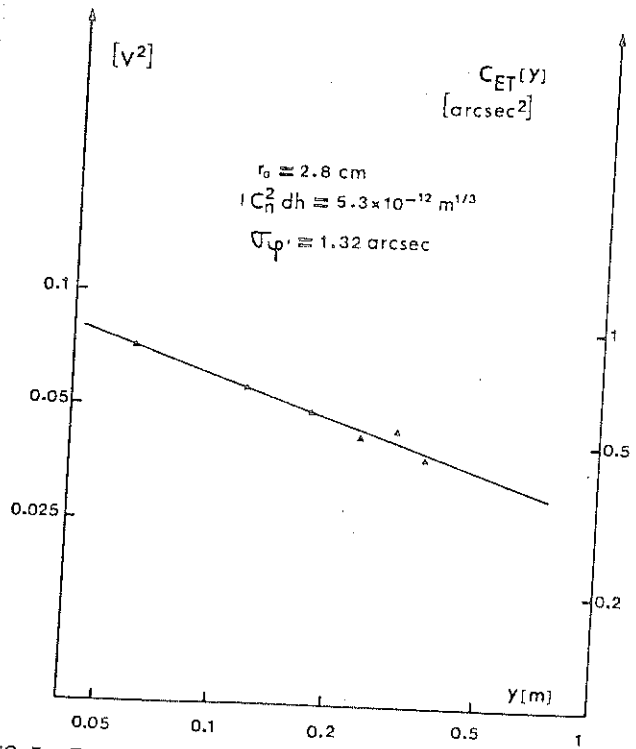


FIG. 7. Transverse autocorrelation of the angle-of-arrival fluctuations. Date, 09/05/77; local time, 13H45′. Correlation coefficient $r = 0.98$ — (▲, experimental points). Slope of the straight-line is −0.336. $\sigma_{\varphi'}$ is the root-mean-square fluctuation of the angles of arrival. The unit indicated of the left scale is a voltage from a correlator.

(Taylor's hypothesis) and that the turbulent layer moves with a velocity v, the size of the greatest observable turbulent eddies will be

$$L = v/\nu_c. \tag{18}$$

When the measurements presented above were taken, the measured velocity of the turbulent layer was approximately 5 m/s which leads to $L = 50$ m.

In the superficial atmospheric boundary layer, the outer scale of the turbulence for daytime conditions is currently supposed[9] to be of the order of a few tens of meters in which one can discern from the ground level first, a forced-convection system generated by the wind shear, second, a composite regime in which the effects of buoyancy and wind combine, and finally a free-convection process. Filtering out the turbulence at an outer scale of 50 m is consequently legitimate, though it is always difficult to know the exact thickness of the superficial atmospheric boundary layer. Furthermore, estimates of altitudes and thicknesses of turbulent layers were performed,[3] during the day, using the Coudé refractor at the Nice Observatory located not far from the sea on top of a rather steep hill at an altitude of 370 m. The altitude profile has shown a maximum energy at about a few tens of meters. The differences observed in a flat region and on clear summer days by Kallistratova,[10] who localized the turbulent fluctuations responsible for the solar limb agitation in a layer a few hundred meters high, seem to us produced essentially by the topographical differences between the observation sites.

The obtained thickness of the turbulent layers was of the

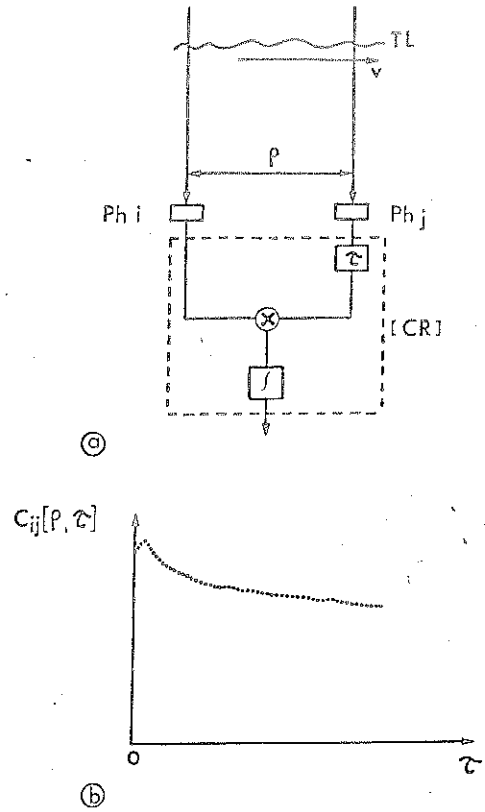


FIG. 9. Measurement of the turbulent-layer velocity. (a) *Principle.* The alignment of the photodiodes is placed in the direction of propagation of the turbulent layer (TL) which moves with a velocity v. ρ is the distance between the photodiodes numbers i(*Phi*) and j(*Phj*). A phase deformation detected by the photodiode number i is detected by the photodiode number j after a time delay τ for which the spatio-temporal correlation function shows a maximum. The velocity of the turbulent layer is given by $v = \rho/\tau$. CR is the correlator. (b) *Example of spatiotemporal correlation function.* Between two consecutive points, we have $\Delta\tau = 3.33$ ms. The distance between the photodiodes, considered on the entrance pupil of the telescope is $\rho = 0.058$ m. In this example $v \simeq 5.8$ m/s.

order of 50 m and this allowed us to select the spatial frequency cutoff to be used in the data processing.

As stated above, in some exceptional cases the inertial model was not well verified, the shift observed on the slope of the autocorrelation function shown on a log-log scale ranging up to 0.1 (30%), tending to give an underestimation of this slope; this fact is attributed to the existence of energy at frequencies lower than the spatial-frequency cutoff 1/50 m^{-1} (i.e., to a variation of the outer scale of turbulence assumed to be 50 m). An example is given in Fig. 10 where straight line (1) represents the raw results and straight line (2) is obtained by adding a constant evaluating the rate of low-frequency energy filtered out during the processing to the autocorrelation-function values[4] in order to verify the inertial hypothesis. Also given in this figure are the correlation coefficients and the estimates of r_0 and $\int C_N^2\, dh$ calculated only in the case where the constant was added; the experimental results are fitted by a $-\frac{1}{3}$ power law, i.e., only when the inertial model is verified.

In Ref. 4, a method using the difference $C_{EL}(x,0) - C_{ET}(0,y)$ [formulas (4) and (5)] permitted the verification of the inertial model of turbulence up to 6 or 9 cm depending on the size of the diaphragm.

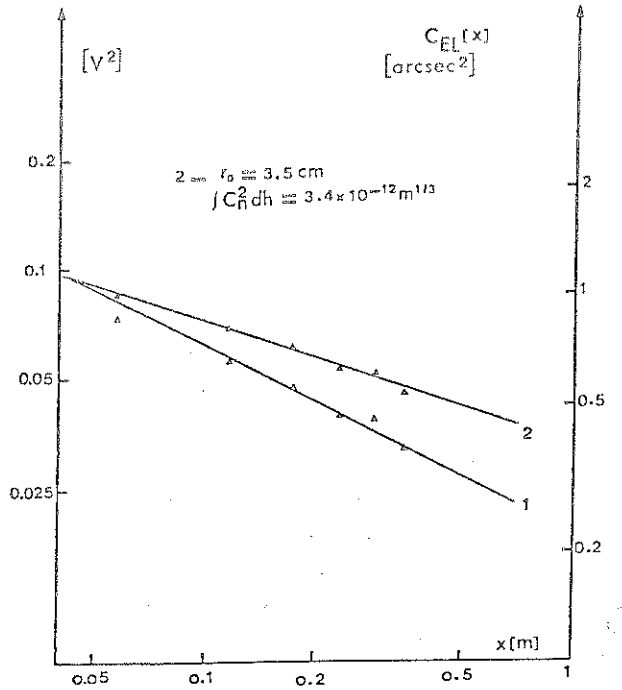


FIG. 10. Longitudinal autocorrelation of the angle-of-arrival fluctuations. Date, 09/05/77; local time, 12H05'. ▲, experimental points. The slope of the straight line (1) is −0.422 (correlation coefficient $r = 0.998$). The values of $C_{EL}(x)$ are the raw results. The slope of straight line (2) is −0.33 (correlation coefficient $r = 0.99$). In this case, the values of $C_{EL}(x)$ are obtained by adding a posteriori to the raw results a constant measuring the loss of energy due to the low-frequency filtering. The unit indicated on left scale is a voltage from a correlator.

Here, the photoelectric method does not give two-dimensional information like the photographic film. So we can obtain $C_{EL}(x,0)$ and $C_{ET}(0,y)$ with only a sequential mode and this implies the stationarity of the turbulence. The time delay between the measurements of $C_{EL}(x,0)$ and $C_{ET}(0,y)$ was usually 10 min. The inertial model of turbulence was also verified using this method but the correlation coefficient decreased from 0.99 or 0.98, values normally obtained (see Figs. 3–8 and 10), down to approximately 0.85.

It will be noticed that the tracking of the solar telescope, which has recently been motorized, presents a drift which is lower than 1 arc sec by 100 s and which is filtered out during data processing.

But, in relatively strong wind with a velocity greater than 10 m/s, the telescope shows vibrations which are detected in recorded signal and which present considerable energy. The frequency of these vibrations was of the order of 1.5 Hz. The low-frequency cutoff being 0.1 Hz, it is impossible to verify the inertial model of turbulence in this case.

VI. COMPARISON WITH RESULTS OBTAINED ELSEWHERE BY OTHER METHODS

Our results are compared with those obtained first from *in situ* temperature measurements performed by instruments carried in a balloon,[9] and which permit the determination of the structure constant C_T^2 of the temperature microfluctuations; secondly by optical methods, namely, the study of limb vibrations of solar images,[10] "image motion" and "blurring"[11] which leads, for example, to the root mean square of the

angle-of-arrival fluctuations and the statistical analysis of the solar granulation[12,13] which permits evaluations of the Fried's parameter r_0. Coulman[9] shows measurements of C_T^2 for mean conditions on clear summer days, conditions probably not very different from those observed in Nice at noon on clear sunny days in May. First of all, we notice that the greatest part of the atmospheric turbulence takes place in the 100 m nearest the ground. Knowing that, we relate the structure coefficient C_N of the refractive index of the air to C_T by

$$C_N \simeq 80 \times 10^{-6}\, pC_T/T^2, \tag{19}$$

where T is the absolute temperature in °K and p the pressure in millibars. Taking for C_T^2 a mean value evaluated on the first 100 m (Ref. 9, Fig. 4), making $T = 300$ °K and $p = 1033$ mbars, we were thus able to calculate $\int_0^{100} C_N^2\, dh$, which is found approximately equal to 5.5×10^{-12} m$^{1/3}$; this value is consistent with those indicated in Figs. 3–8.

In Ref. 3, we have studied the filterings performed by the diaphragm placed on the solar limb. From the ground up to an altitude h_c, the diffraction produced by the slit filters the energy of turbulent eddies, the size of which ranges from 1 mm [lower limit of the inertial subrange in the troposphere (Ref. 14, p. 86)] up to a certain value constant with the altitude, but which depends on the size of the diaphragm and on the wavelength of the light.

For altitudes higher than h_c, the angular filtering becomes predominant and the spatial high-frequency cutoff is a function of the altitude considered. As an example, for a turbulent layer located at an altitude of 200 m this cutoff is equal to 100 m^{-1} (size of turbulent eddies equal to 1 cm).[3]

These filterings result in the root mean square of the angle-of-arrival fluctuations to be always underestimated.

Taking into account this underestimation and also the angle made between the line of sight and the zenith, the results shown in Figs. 3–8 seem to be comparable to those of Kallistratova,[10] who, for well-developed convection conditions and using a scanning technique of the solar limb, estimated that the root-mean-square vibrations of solar-limb images do not exceed 1.5 arc sec (at the zenith) for objective diameters $d \geq 5$ cm. At the Nice Observatory, however, it would appear that values of this root mean square much greater than the above value can be reached. Our results are also in good agreement with those obtained by Brandt,[11] who estimated photoelectrically the root mean square of the fluctuations of the solar-limb image.

Our results are still consistent with independent estimates obtained on the same telescope by statistical analysis of the solar granulation.[4] However, it is now necessary to compare the results obtained from simultaneous experiments, the study of solar granulation allowing the calculation of r_0 and $\int C_N^2\, dh$ integrated on the whole atmosphere, while our method will give an estimation of the same quantities integrated on the lowest part of the atmosphere. Such a comparison is currently being undertaken.

VII. CONCLUSION

From the estimates of the transverse or longitudinal one-dimensional autocorrelation functions for the angle-of-arrival fluctuations considered perpendicularly to the solar limb, the inertial model of turbulence was verified for spatial shifts up to 35 cm. The measurement of the velocity of the turbulent layers enabled the investigators to select the low-frequency cutoff to be used in data processing, the outer scale of the turbulence near the ground being evaluated from independent estimates. Finally, values are obtained for Fried's parameter r_0, the integral $\int C_N^2\, dh$ of the structure constant for the variations of the refractive index of the air on the thickness of the atmosphere traversed and the root mean square of the angle-of-arrival fluctuations. These values seem consistent with independent estimates drawn from statistical analysis of the solar granulation, *in situ* soundings, or study of the agitation of the solar limb made under similar conditions.

[1] R. E. Hufnagel, Proceedings of AGARD Conference (Ankara) (1967).
[2] N. V. Bystrova and A. N. Demidova, Solnecnye Dannye **3**, 73 (1961).
[3] J. Borgnino and F. Martin, J. Opt. (Paris) **8**, 319–326 (1977).
[4] J. Borgnino and F. Martin, J. Opt. Soc. Am. **67**, 1065 (1977).
[5] F. Martin and J. Borgnino, "Statistical analysis of wavefront random deformations produced by atmospheric turbulence near the ground." 2nd part, "Correlation function estimation by numerical processing", J. Opt. (Paris) (to be published).
[6] D. L. Fried, J. Opt. Soc. Am. **56**, 1372 (1966).
[7] C. Roddier, J. Opt. Soc. Am. **66**, 478 (1976).
[8] A. Rocca, F. Roddier, and J. Vernin, J. Opt. Soc. Am. **64**, 1000 (1974).
[9] C. E. Coulman, Sol. Phys. **7**, 122 (1969).
[10] M. A. Kallistratova, Radiofizika **9**, 50 (1966).
[11] P. N. Brandt, Sol. Phys. **7**, 187 (1969).
[12] G. Ricort, Thesis, 3rd cycle, (Nice University, France, 1973).
[13] C. Aime, Thesis (Nice University, France, 1977).
[14] V. I. Tatarski, "The effects of the turbulent atmosphere on wave propagation" (1971) translated by Israel Program for Scientific Translations.

Astron. Astrophys. 276, 663–672 (1993)

ASTRONOMY AND ASTROPHYSICS

Isoplanatism and high spatial resolution solar imaging

A. Irbah[1], J. Borgnino[2], F. Laclare[3], and G. Merlin[3]

[1] Observatoire d'ALGER, CRAAG, B.P. 63 Bouzareah, Alger, Algerie
[2] Départment d'Astrophysique-Université de Nice-Sophia Antipolis, Faculté des Sciences, F-06108 Nice Cedex 2, France
[3] Observatoire de la Côte d'Azur, CERGA, Avenue Copernic, F-06130 Grasse, France

Received July 2, 1992; accepted February 22, 1993

Abstract. A method is presented allowing one to estimate, in the case of daytime observations, the angle-of-arrival isoplanatic patch size from the measurement of the differential image motion of the solar limb. The experimental results have been obtained using the solar astrolabe of Calern Observatory (CERGA-France). Performing a modelization as proposed by Fried (1977) leads to an explanation of these results by an equivalent atmosphere formed with two impulse turbulent layers corresponding to two different scales for the size of the isoplanatic patch. Finally, the isoplanatism is quantified for speckle interferometry and adaptive optics experiments.

Key words: atmospheric effects – methods: observational – techniques: image processing – Sun: general – Sun: photosphere

1. Introduction

The formation of astronomical images through the terrestrial atmosphere by means of ground-based telescopes is generally formalized as a convolution product which expresses a spatial-frequency linear filtering. By using this formalism, one assumes in particular that the point spread function of the whole system, telescope and atmosphere, is invariant over the observation field. If one considers wavefronts coming from a point source through the atmospheric turbulent layers, they appear randomly perturbed, in space and time, which gives consequently a random behaviour to this point spread function. At any moment, one can consider that the point spread function is invariant only on a precise patch, named the isoplanatic patch, of the observation field and that it follows well-determined characteristics of the perturbations due to the atmosphere.

The importance of knowledge of this patch size has increased with the development of high-angular-resolution observation techniques (real-time and post-detection image restoration) which allow one to overcome the optical effects due to atmospheric turbulence and to reach the theoretical resolution of the instruments. Thus, in adaptive optics, the creation of laser backscattered reference stars (Foy & Labeyrie 1985) which would lead to the measurement of the wavefront and then to real-time compensation of the atmospherical effects has to be elaborated by taking into account the constraints related to the size of the isoplanatic patch (Welsh et al. 1991; Séchaud et al. 1990; Chassat 1989). Similarly, for image reconstruction techniques applied to extended astronomical objects (Sun, multiple star systems, ...), it is necessary to break up the image into an array in which each element to be corrected has to be smaller than the isoplanatic patch size (Von Der Lühe 1988).

This paper has been conceived as a contribution to the study of the angle-of-arrival isoplanatism in the case of daytime high angular resolution imaging for which the promising results of adaptive optics in the stellar field (Primmerman et al. 1991; Fugate et al. 1991) could be applicable. In the first part are reviewed the different concepts and useful theoretical results together with measurement techniques for isoplanatic patch size estimation. A subsequent method for evaluating the angle-of-arrival isoplanatism in the case of solar observations is introduced. An experiment is described and some experimental results obtained on the site of Calern (CERGA-Grasse-France) are presented. Finally, using a modelization proposed by Fried (1977), a vertical localization of the turbulence "optical strength" $C_n^2(h)$ (structure constant of the air-refractive-index fluctuations) is deduced, which leads to the estimation of the isoplanatic patch sizes for adaptive optics and speckle interferometry.

2. Isoplanatism. Theoretical aspects

Atmospheric turbulence causes perturbations on the wavefront coming from a point source which gives at ground level, random fluctuations of the phase and of the intensity. One considers frequently only the phase fluctuations (near-field approximation); one observes the point spread function in the focal plane as an image of speckles,

Send offprint requests to: J. Borgnino

which have spatio-temporal dependence. Speckle formation is due to the random phase differences which create an interferogram in the focal plane. The number of speckles in the image is of the order of $(D/r_0)^2$ where D is the pupil diameter and r_0 is the so-called Fried's parameter which is related to the size of the coherence areas of the wavefront arriving at the entrance of the telescope pupil. The image motion is due to the angle formed by the pupil plane with the wavefront slope all over the pupil; this defines an averaged angle of arrival which may be also considered at each point of the wavefront.

This isoplanatism expresses in a general way, the similarity of the wavefronts arriving on the pupil from two point sources separated by an angle θ on the sky and which have traversed different zones of the turbulent atmosphere. According to the desired application, which can be categorised by the features of interest in the images, a precise analysis of the wavefront deformations can be done which implies the definition of several types of isoplanatism. In the framework of this study, the classification introduced by Fried (1976) has been used, but limited to the case of isoplanatism relevant to angle-of-arrival observations, and also for adaptive optics and speckle interferometry for which the general concepts are reviewed.

The angle-of-arrival isoplanatic patch is the angular field of view on which one can consider that all image points are subjected to the same motion effect which results from the averaging of the angle-of-arrival fluctuations over a pupil of diameter equal to D. It expresses in fact, the angular covariance of these fluctuations observed on two lines of sight separated on the sky by θ. To characterize this isoplanatism, it is convenient to make use of the structure function $D_I(\theta)$ defined as:

$$D_I(\theta)=\langle[\alpha(\theta_1)-\alpha(\theta_1+\theta)]^2\rangle,$$

where $\alpha(\theta_1)$ describes the angle-of-arrival fluctuations averaged over a pupil of diameter D for the wavefront coming from a source in the direction θ_1 and $\langle\ \rangle$ symbolizes a set mean.

An analytic expression for $D_I(\theta)$ has been established by Fried (1976) whose later approximate form (Fried 1977) we use:

$$D_I(\theta)=D^{-1/3}\int_{\text{Path}} C_n^2(h)\,F(h,\theta)\,dh, \tag{1}$$

where h denotes the altitude and

$$F(x)=5.98\left(1+\left(\frac{0.864}{x}\right)^2\right)^{-1} \quad \text{with} \quad x=\frac{\theta h}{D}.$$

The analytic expression has been calculated numerically and compared to the approximate form. A good agreement between the two expressions has been found and for conciseness, the second one will be used hereafter.

According to the definition given by Fried (1977), the isoplanatic patch is:

$$\theta_{AOA}=0.864\frac{D}{h_{AOA}}, \quad \text{where} \quad h_{AOA}=\left[\frac{\int h^2 C_n^2(h)\,dh}{\int C_n^2(h)\,dh}\right]^{1/2}. \tag{2}$$

The speckle interferometry isoplanatism corresponds to the angular field over which one can consider that the speckle interferograms obtained when one observes two point sources separated by θ are the same, according to a given criterion. Its expression can be found by considering the cross-correlation between the corresponding optical transfer functions which can be expressed according to the complex amplitude second-order moment $B_\theta(f)$ (Fried 1979; Roddier et al. 1982):

$$B_\theta(f)=\langle\psi(u,\theta_1)\,\psi(u+f,\theta_1+\theta)\rangle$$

In the case of a fully-developed turbulence (Kolmogorov's law) and for $D\gg r_0$, this moment can be expressed by:

$$B_\theta^2(f)=\exp\left(-6.88\left(\frac{\lambda}{r_0}\right)^{5/3}\frac{\int\left|f+\frac{\theta h}{\lambda}\right|^{5/3}C_n^2(h)\,dh}{\int C_n^2(h)\,dh}\right). \tag{3}$$

The isoplanatic patch for speckle interferometry can be obtained by integrating expression (3):

$$\theta_{SP}=0.36\frac{r_0}{h_{SP}},$$

$$\text{where} \quad h_{SP}=\left[\frac{\int h^2 C_n^2(h)\,dh}{\int C_n^2(h)\,dh}-\left[\frac{\int h C_n^2(h)\,dh}{\int C_n^2(h)\,dh}\right]^2\right]^{1/2}. \tag{4}$$

For adaptive optics, the isoplanatic patch is the angular field on the sky where one can consider that the wavefronts coming from two points sources angularly separated by θ and arriving on the same point in the pupil plane of the instrument are similar according to a given criterion. The expression for isoplanatic patch can also be deduced from the relation (3) by calculating $B_\theta(0)$ (Roddier et al. 1982):

$$\theta_{AO}=0.31\frac{r_0}{h_{AO}}, \quad \text{where} \quad h_{AO}=\left[\frac{\int h^{5/3} C_n^2(h)\,dh}{\int C_n^2(h)\,dh}\right]^{3/5}. \tag{5}$$

One can see that in every case, knowledge of the vertical profile of the optical strength $C_n^2(h)$ permits the estimation of the isoplanatic patch which can be interpreted using a model (Shapiro 1976) in which a single thin layer is localized at an altitude (h_{AOA}, h_{SP}, h_{AO}) defined by a weighting of $C_n^2(h)$ [Expressions (2), (4) and (5)].

Another remark is that when observing with a small aperture telescope, the size of the isoplanatic patch will not differ considerably for one type of isoplanatism to another but will vary notably for large astronomical telescopes.

3. Measurement techniques

Several techniques have been used to estimate the isoplanatic patch. Some of them give direct measurements,

other use an intermediate parameter and a model to describe the terrestrial atmosphere. In the following we give some techniques which permit isoplanatic patch estimations and some typical values obtained by observers.

Various measurements of isoplanatic patch for stellar speckle interferometry and adaptive optics were performed in the visible by Roddier et al. (1982) who derived the parameter using turbulence profiles $C_n^2(h)$ and applying the expressions (4) and (5). The measurements show that for speckle interferometry, the isoplanatic patch is systematically more important (mean value of the order of 3 arcsec) than for adaptive optics (mean value of the order of 2 arcsec). From the cross-correlation function of double star speckle interferograms, Vernin et al. (1991) deduce the degree of isoplanatism (Fried 1982) and derive an estimation of the isoplanatic angle. Using the SCIDAR technique which consists of a statistical analysis of scintillation patterns, permits these observers to obtain turbulence profiles $C_n^2(h)$ and with seeing measurements to compute the isoplanatic patch for speckle interferometry. These two techniques give the same estimate of the isoplanatic patch which is of the order of 3.6 arcsec. Direct measurements of the isoplanatic patch were performed by Walters (1985) who developed a stellar scintillometer from an approximation of Fried's expression (1982) for given light wavelength and telescope diameter. The conception of an isoplanometer which is also a stellar scintillometer is due to Loss & Hogge (1979) and White & Garvey (1985) who have performed continuous measurements of the isoplanatic patch for speckle interferometry. The mean value of the measurements is of the order of 1 arcsec which is smaller than the results of other observers.

For solar observations, there are fewer isoplanatism measurements than for night observations. One can first reference the experiment of Borgnino & Martin (1977) who analysed the spatio-temporal characteristics of the wavefronts arriving on the pupil by observing it through two diaphragms placed on the solar limb image. They observed that some wavefront areas stayed correlated on an angular field which might be extended. Turbulence profile measurements $[C_n^2(h)]$ in daytime conditions allowed to Murphy et al. (1985) to compute from Fried's expression (1979) isoplanatic patch estimates which typically were of the order of 1–2 arcsec. Finally, adaptive optics techniques were used to obtain high angular resolution solar images (Hardy 1981; Acton 1988; Rimmele & Von der Lühe 1988). For these experiments it has been assumed that the maximum value reached by the isoplanatic patch was of the order of 3 or 4 arcsec. A value of the same order was also used in the framework of post-detection reconstruction methods (Von der Lühe 1988).

4. Isoplanatic patch measurement using a photoelectric detector

The point spread function of the atmosphere–telescope system can be obtained by observing an unresolved star or, in the case of solar observations, by considering the brightness discontinuity formed by the solar limb. In a first approximation, the solar limb intensity can be considered, taking into account the resolving power of the instrument and the wavelength at which the observations are performed, as an Heaviside distribution $H(\alpha)$ (Druesne et al. 1983). Indeed, if a one-dimensional detector such as a linear photodiode array is put perpendicularly to the solar image edge (Fig. 1a), one can write, assuming that each photoelement is of negligible width and moreover that its physical properties are not taken into account, the detector spatio-temporal response $F(\alpha, t)$ (Fig. 1b) as:

$$F(\alpha, t) = [H(\alpha) * S(\alpha, \beta, t)]\delta(\beta), \quad (6)$$

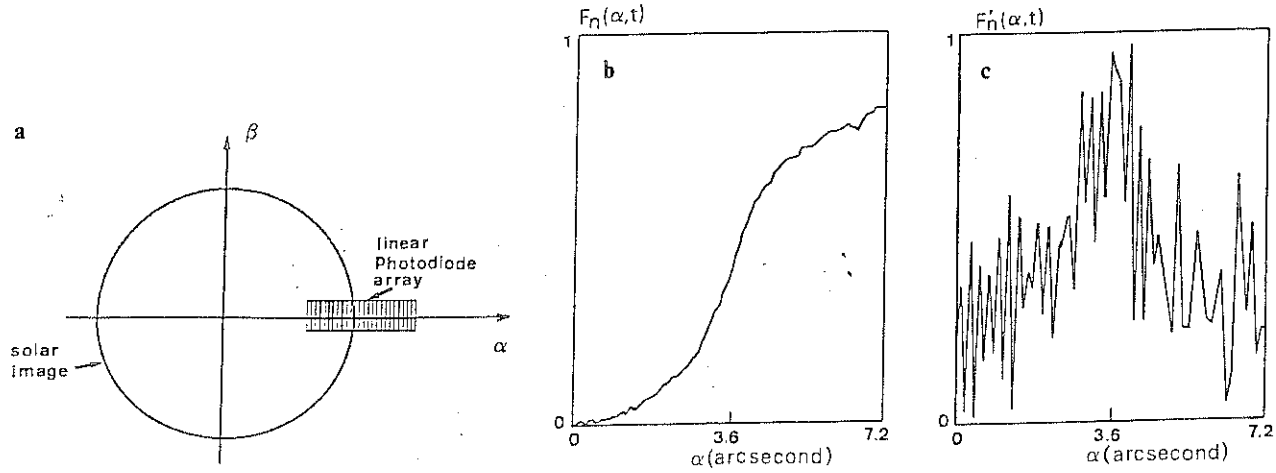


Fig. 1a–c. Estimation of the point spread function of the telescope–atmosphere system obtained at the Nice Observatory using a 38 cm solar telescope: **a** principle of the experiment, α, β = angular directions on the sky; **b** $F_n(\alpha, t)$ = normalized irradiance distribution in the solar limb image [Expression (6)]; **c** $F'_n(\alpha, t)$ = normalized point spread function of the telescope-atmosphere system [Expression (7)]

where $*$ denotes a convolution product, α and β are the components of an angular direction on the sky, $S(\alpha, \beta, t)$ is the point spread function of the system formed by the atmosphere and the telescope and δ the Dirac distribution.

If this expression is derived with respect to α, one obtains the one dimensional point spread function as already presented in Druesne et al. (1983):

$$F'(\alpha, t) = [\delta(\alpha) * S(\alpha, \beta, t)]\delta(\beta) = \delta(\beta) \int S(\alpha, \eta, t)\, d\eta. \quad (7)$$

This expression shows that one should obtain experimentally a one-dimensional projection of the point spread function (Fig. 1c). Thus, the continuous acquisition of the solar image formed on the detector gives the point-spread-function temporal evolution which allows estimation of the parameters qualifying the atmospheric turbulence or more precisely the perturbed wavefronts (r_0, time constants, isoplanatic patch size).

For the angle-of-arrival isoplanatism study, there are two possibilities according to whether one uses a one or a two-dimensional detector.

The angle-of-arrival isoplanatism can be studied using a linear photodiode array, with rectangular elements (the ratio between the two dimensions being for example of the order of 100). In the following, the detector is assumed to have a linear intensity response. Indeed, if the linear photodiode array is placed on the solar image in a direction parallel to the limb (Fig. 2a), each photoelement response will be the solar limb intensity distribution integrated on a few arcseconds. This integration will lead to a solar limb position for each observation field point defined by each photoelement (Fig. 2b). The continuous image acquisition allows to observe and record the solar limb fluctuations (image motion) (Fig. 2c) for which a spatio-angular correlation leads to an estimation of the angle-of-arrival isoplanatic patch size.

The advantage of the method is the simplicity of the application for estimating in real time the parameter of interest. The main difficulties are related to the spatial calibration of the fluctuations and to the dynamics which is imposed by the continuum of the mean position, more or less important, of the solar image on the detector.

The use of a two-dimensional detector as a CCD camera gives access to more information and makes it possible the estimation of all the parameters qualifying the terrestrial atmosphere and consequently the astronomical images. Indeed, as for the preceding case, the CCD camera is put on the edge of the solar image (Fig. 3). Each line of the camera gives a solar limb profile which allows to deduce a projection of the point spread function of the whole system, telescope and atmosphere, as seen in the previous section [Expression (7)]. The image acquisition gives then, a spatio-temporal evolution of the point spread function for an angular field on the sky. From this evolution, one can deduce the angle-of-arrival isoplanatic patch size from the angular correlation of the fluctuations shown by the position of the point spread function projection defined as the position of the photocenter. A study of the correlation between the point spread functions obtained from the different line signals (perpendicular to the solar limb) of the CCD camera, leads to perform a speckle interferometry type analysis if a spectral filtering is done on the solar image.

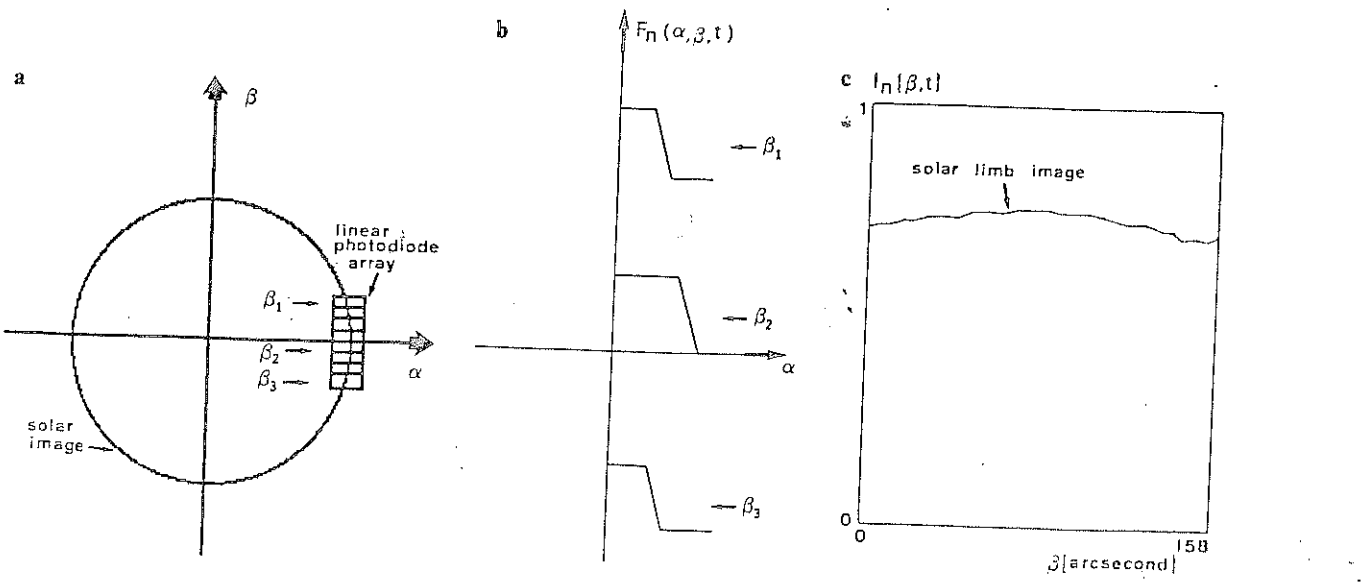


Fig. 2a–c. Estimation of the angle-of-arrival isoplanatic patch size using a linear photodiode array with the same experimental device as for the result presented in Fig. 1: a principle of the experiment; b schematic examples of the solar limb profile; c normalized solar limb intensity with the continuum before analogic–numerical conversion. One will note the small magnitude of the fluctuations averaged according to the angular component α, on a range of the order of 100 arcsec

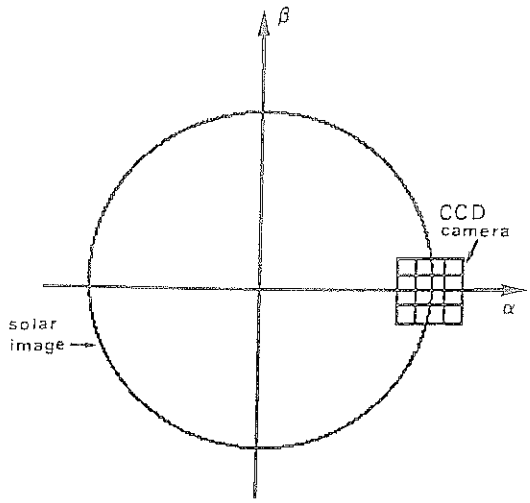


Fig. 3. Estimation of the angle-of-arrival isoplanatic patch size (and eventually, of the spatial coherence of the perturbed wavefronts as expressed using Fried's parameter r_0, of the time constants ...). The principle of the experiment is given if the detector in use is a CCD camera

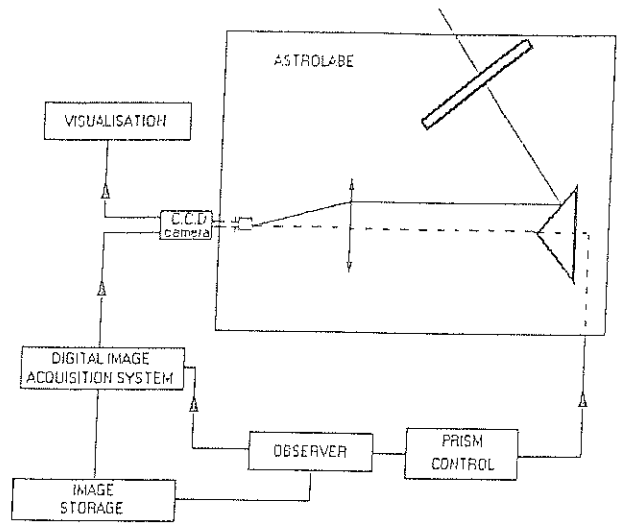


Fig. 4. The data acquisition device. The instrument is widely described in the paper of Laclare & Merlin (1991)

5. Observations and results

The measurements have been performed making use of the experimental principle detailed in the previous section but with the difference that the observed solar limb image is moving in the focal plane during the observation time. The instrument is a Danjon astrolabe which does not compensate the earth diurnal motion.

5.1 Observations

The observations have been made using the solar astrolabe of the Calern Observatory (Observatoire de la Côte d'Azur) which is currently used for solar diameter measurements (Laclare & Merlin 1991). For the study of atmospheric turbulence, the experiment has been modified. These modifications consist for the main part, in the two following points:

— the analogic detection system of the solar limb inflexion point given by a CCD camera which provides 512×512 pxl, has been replaced by a digital image acquisition system.

— the astrolabe is an instrument which gives in its focal plane two images of the same object (a direct and a reflected image). For the solar diameter measurements, the two images are used and formed alternatively on the CCD camera by a mechanical obturator. For this experiment, the obturator is removed and only the direct image formed by the upper part of the objective which has an elliptic form (the major axis is 8 cm and the minor 5 cm) is used. Because of the limited memory of the system and to process a greater number of images, a window of 128×256 pxl has been placed on the solar image.

Figure 4 shows the data acquisition device.

An acquisition of the solar limb image is done every 20 ms which is the standard integration time of the camera. The fluctuations of the images are attributed to the motion effect, the result of the angle-of-arrival fluctuations observed at each wavefront point, averaged on the astrolabe pupil during the integration time of the camera. In the case of an unresolved solar limb from which one can define the point spread function position as the photocenter position, each point of the image edge is affected only by the motion effect. The displacement fluctuations obtained by observing the temporal evolution of a part of the solar image will then give an estimation of the angle-of-arrival structure function which allows one to deduce the value of the associated isoplanatic patch.

5.2. Results

The experimental results presented here come from observations performed in June 1990 at the Calern Observatory. In Fig. 5a one can see two estimations of the angle-of-arrival structure function $D_l(\theta)$ [Expression (1)] obtained from the computational data of two different observation days. In this figure no correction has been done but one must take into account the noise effects on the structure or autocorrelation function analysis. So let's consider hereafter the noise effects. One supposes that a white noise is superposed on the fluctuation signal measurements which is translated on the autocorrelation function (or on the structure function) by a peak located at the origin or on the power spectrum by a uniform energy distribution over all frequencies as clearly observed after the telescope frequency cut-off (Aime et al. 1979). Consequently, to estimate the noise level, one considers the power spectrum and also the behaviour of the structure function of the

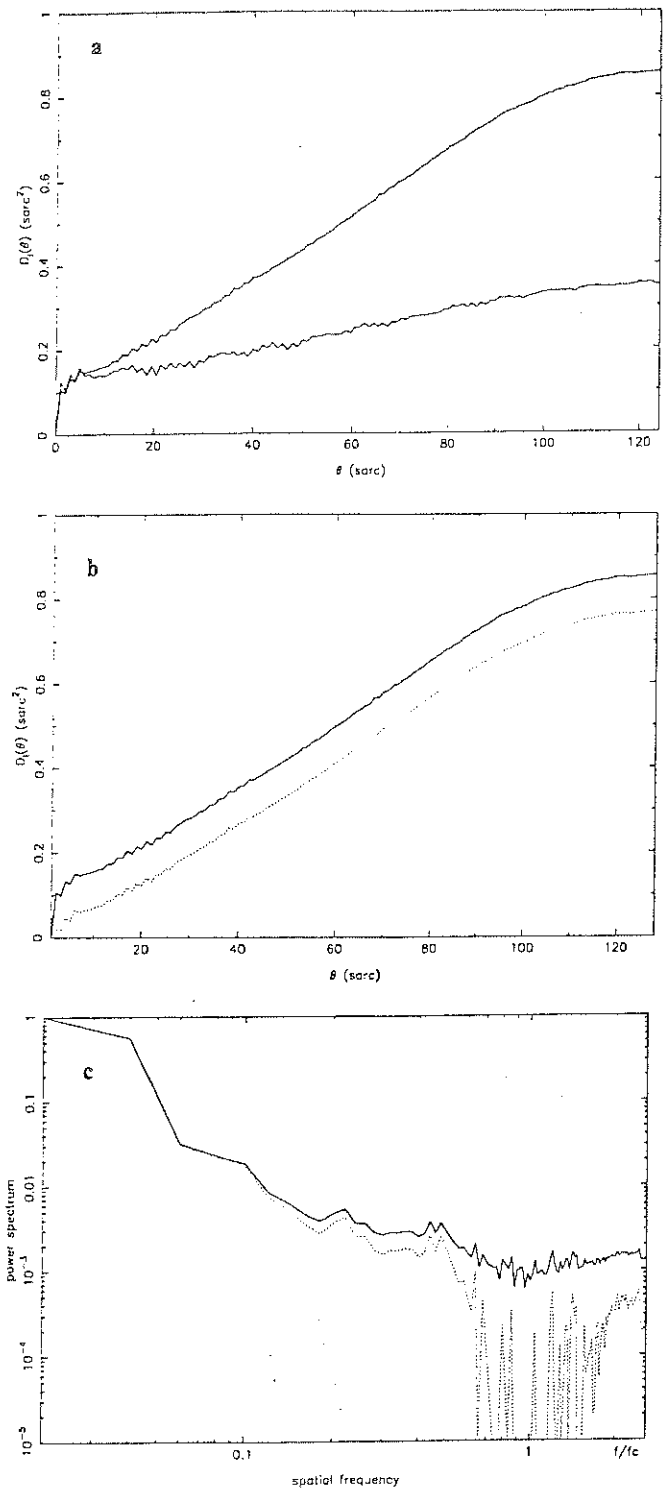


Fig. 5a–c. Experimental estimations of the angle-of-arrival structure function obtained observing the solar limb motion (without noise correction **a**). Effect of the correction of the photon noise on a typical estimation of the angle-of-arrival structure function **b** and on the corresponding power spectrum **c**

angle-of-arrival fluctuations for small values of θ as done by Fried (1977). Indeed, to define the isoplanatic patch Fried has considered the intersection between a parabolic fit of the structure function $D_I(\theta)$ for small values of θ and the straight line giving the saturation of this function for large values of θ. Fried's definition leads to the relation (2) in Sect. 2 which gives the angle-of-arrival isoplanatic patch size as a function of the pupil diameter D and of the altitude h_{AOA} of an impulse layer equivalent to the whole turbulent atmosphere (an experimental illustration is given in Fig. 6). To have a noise level estimate, one fits the structure function by a parabolic law where the first point is not included and deduces its value from the fit. One can see in Fig. 5b the effect of the noise correction on a typical structure function and in Fig. 5c the corresponding effect on the power spectrum. In the last case, one can note the effect of the noise level reduction on the high spatial frequencies while the low frequencies are not notably affected as identically observed by Aime et al. (1979). However, from the data coming from all the observations, one can note that there is not one single way to fit a parabolic law for small values of θ but that this can be performed on two distinct angular ranges (Fig. 7). According to Fried's definition and for two series of observations are shown, in Table I, the results deduced from parabolic fits in the two typical variation ranges of the structure function. The first range corresponds to the variation of the structure function at the origin which expresses the fast angle-of-arrival fluctuations averaged on the instrument pupil and the second range corresponds to the slowest variation of this structure function. Determination of isoplanatic patch sizes from these two variation ranges seems identical to that performed by other observers who deduced two different time constants from the measurement of the temporal autocorrelation function obtained by analysing during the time, the brightness intensity of the solar granulation (Aime et al. 1981). For night observations, the same results

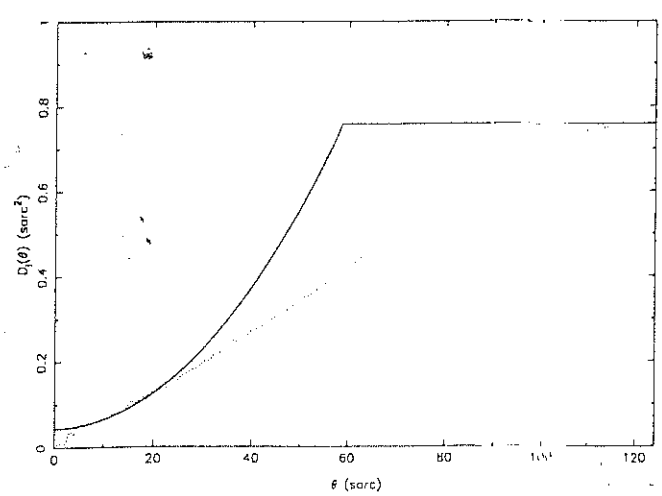


Fig. 6. Estimation of the isoplanatic patch size using a parabolic fit (continuous line) near the origin of the experimental structure function (dotted line) obtained from the observation of the angle-of-arrival fluctuations. The horizontal straight-line gives an approximated value of the saturation which occurs at large values of θ

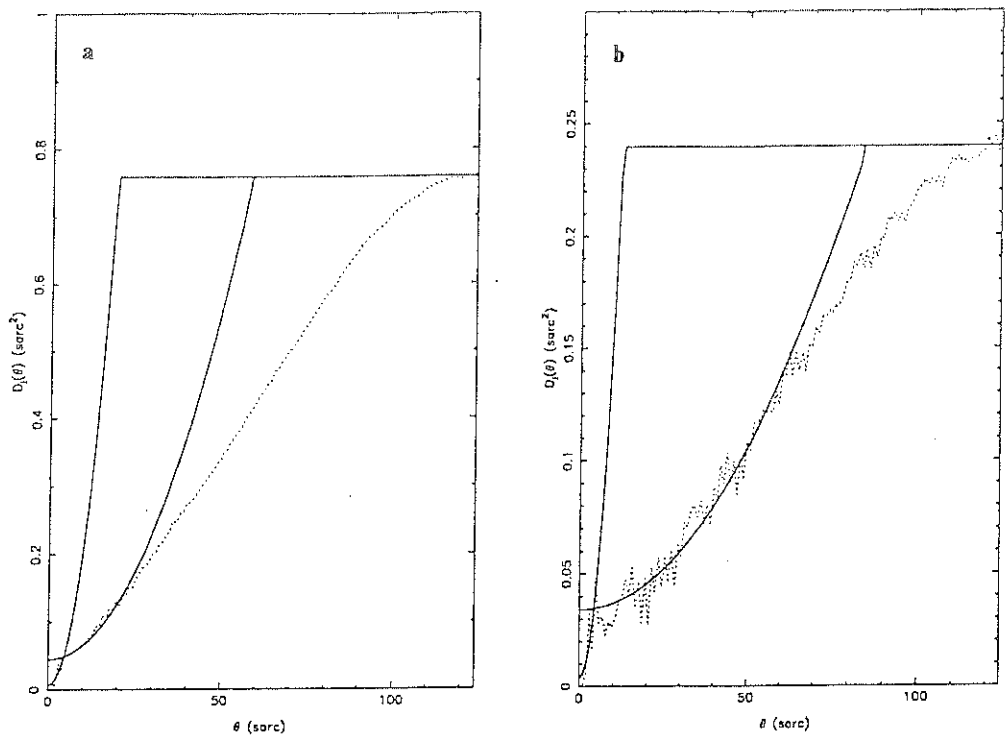


Fig. 7a and b. Possible fits (continuous lines) on two examples of the experimental angle-of-arrival structure function (dotted line) in order to estimate the isoplanatic patch size: **a** date = 21/06/90, $\theta_{AOA1} = 19.3''$, $h_{AOA1} = 642$ m, $\theta_{AOA2} = 58.8''$, $h_{AOA2} = 210$ m; **b** date = 25/06/90, $\theta_{AOA1} = 12.1''$, $h_{AOA1} = 1024$ m, $\theta_{AOA2} = 84.9''$, $h_{AOA2} = 146$ m

Table 1. Isoplanatic patch size: experimental results From this two-layer model are computed the isoplanatic patch sizes and the corresponding altitudes h_{AO}, h_{sp}, h_{AOA} (Expressions (5), (4) and (2)) for adaptive optics, speckle interferometry and for the angle-of-arrival fluctuations

Date	21/06/90	21/06/90	21/06/90	25/06/90	25/06/90	25/06/90
r_0 (cm)	11.2	6.7	7	12.4	13.8	10.2
H_{AOA1} (m)	1046	642	1365	1092	1024	931
Isoplanatic patch Range 1 (arcsec)	11.83	19.28	9.07	11.33	12.09	13.29
H_{AOA2} (m)	164	210	154	146	146	145
isoplanatic patch Range 2 (arcsec)	75.70	58.81	80.44	84.58	84.85	85.62
isoplanatism adaptive optics (arcsec)	4.9	3.8	2.2	5.8	5.8	5.7
isoplanatism speckle interferometry (arcsec)	4.4	3.3	2.2	5.1	5.3	4.9
isoplanatism angle-of-arrival (arcsec)	5.4	6.7	4.1	5.7	5.2	6.7
h_{AO} (m)	1474	1139	2043	1372	1524	1140
h_{SP} (m)	1889	1530	2421	1782	1941	1531
h_{AOA} (m)	1984	1592	2604	1866	2041	1593

r_0 = Fried's parameter
H_{AOA1}, H_{AOA2} = altitudes of the two impulse turbulent layers corresponding to the isoplanatic patch sizes (Ranges 1 and 2) which can be deduced from the experimental angle-of-arrival spatio-angular structure function.

have been obtained (Aime et al. 1986; Scaddan & Walker 1978) and an interpretation has been proposed in the case of stellar speckle patterns introducing a new model based on the image motion (Aime et al. 1986).

6. Discussion

The results presented above show that the experimental structure function $D_I(\theta)$ has two variation ranges on which can be defined two isoplanatic patch sizes. The shape of $D_I(\theta)$ is related to the vertical atmospheric turbulence profile (see Sect. 2); one can then assume, in a first approximation, that each variation corresponds independently to a thin turbulent layer localized at an altitude h_{AOA} which can be estimated by (Fried 1977):

$$h_{AOA} = \frac{D}{\theta_{AOA}},$$

where D is the diameter of the instrument pupil.

One can then, with this assumption, locate the layers responsible for the two variation ranges presented by the structure function $D_I(\theta)$. The fast variation is due to a layer localized at the higher altitude whereas the slower variation is due to a layer at a lower altitude. In Table 1, one can also found, for each isoplanatic patch, the altitude of the associated turbulence layer. In Figs. 8b and 9b are presented the vertical C_n^2-profiles for both Hunfnagel model (daytime conditions) and the restored profile which corresponds to the experimental structure functions. For each layer, the turbulence strength is chosen to fit the angle-of-arrival structure function, computed from the relation (1) (see Sect. 2), to the experimental data (Figs. 8a and 9a). One can note that for the two cases, one can access to a vertical C_n^2-profile which explains correctly the observations and defines, as already said above, the magnitude of the different isoplanatic patch sizes. Thus, with a simple model of two thin layers and the relations given in Sect. 2, one can deduce an estimate of the isoplanatic patch for adaptive optics, speckle interferometry and angle-of-arrival fluctuations using only an angle-of-arrival statistical analysis. It must be noted that one can also deduce the angle-of-arrival isoplanatic patch from the relation (3) which is equivalent to a parabolic fit at the origin of $D_I(\theta)$. From this relation, one obtains values more or less different than those derived from the fit on the experimental data done using a least-mean-square adjustment on a chosen angular field which can be overestimated compared with Fried's hypothesis in the approximate form. For each observation series, performed at a wavelength equal to 500 nm, an estimate of a vertical C_n^2-profile has been done which allows to compute estimates of Fried's parameter r_0, as well as the isoplanatic patch for adaptive optics θ_{AO}, for speckle interferometry θ_{SP}, for angle-of-arrival fluctuations θ_{AOA} and the scale heights for the single thin layer model (Table 1). It is advisable to note that for speckle interferometry determination, the expression implies that D is great compared to r_0 which is not true for our observations. The value has been computed to give an estimate of this parameter which appears to be comparable with the other values. One can see that for all

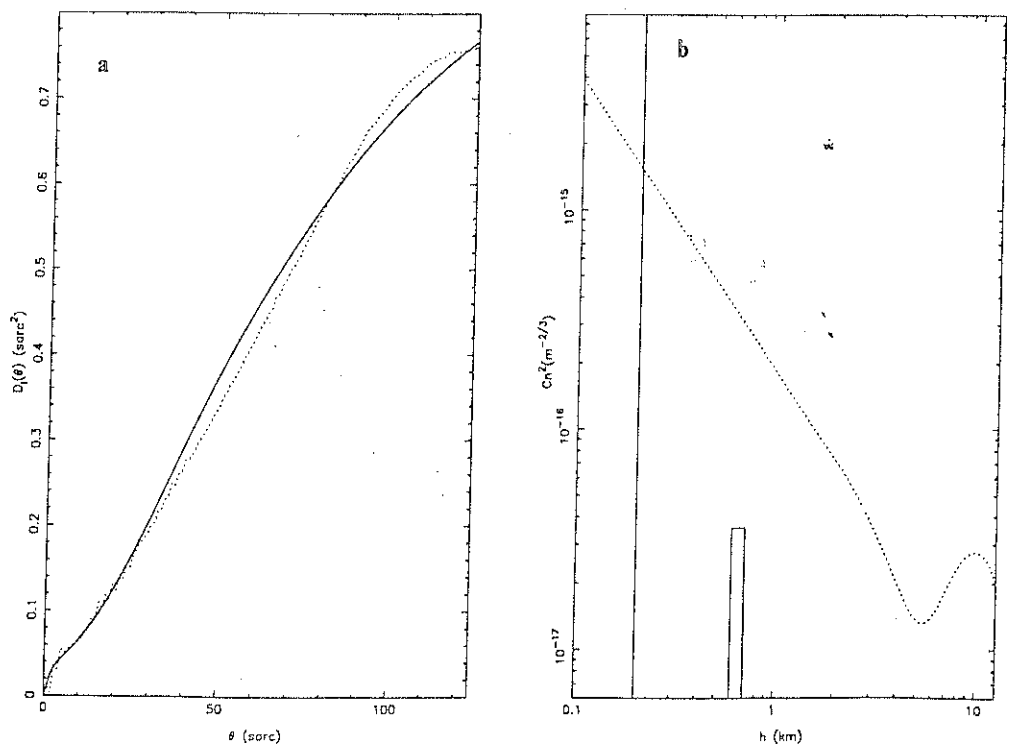


Fig. 8a and b. Interpretation of the experimental angle-of-arrival structure function using a two-layer model to describe the atmospheric turbulence – Example (a) of Fig. 7: a (... ...) experimental result; (——) function deduced from relation (1) when the turbulence is given by a two-layer distribution (see b); b (——) model of turbulence; (... ...) Hufnagel mean model-daytime conditions

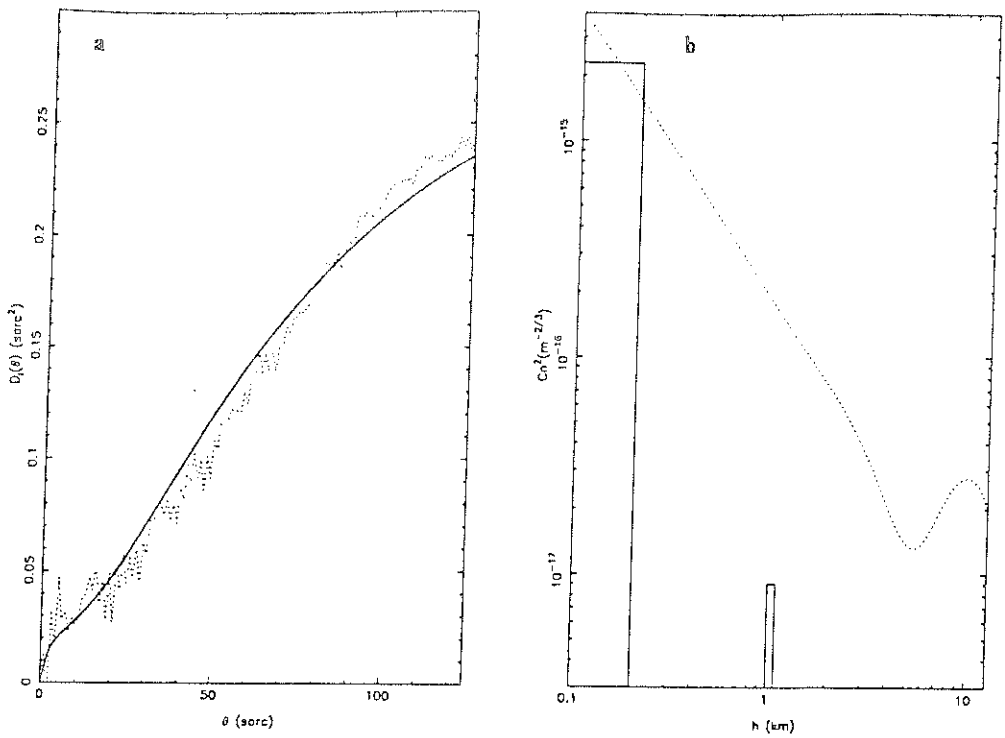


Fig. 9a and b. Interpretation of the experimental angle-of-arrival structure function using a two-layer model to describe the atmospheric turbulence – Example (b) of Fig. 7: **a** (... ...) experimental result; (——) function deduced from relation (1) when the turbulence is given by a two-layer distribution (see b); **b** (——) model of turbulence; (... ...) Hufnagel mean model-daytime conditions

cases, the estimate is of the same order but more larger than those reported by other observers (see Sect. 3). Finally, one can note, analyzing the estimated vertical C_n^2-profiles, that the atmospheric turbulence relevant to high spatial resolution solar imaging is localized in the first hundred meters.

7. Conclusion

The principle of a method which allows the measurement of the angle-of-arrival isoplanatic patch for day-time observations has been presented. The results deduced from observations performed using the solar astrolabe of Calern Observatory (CERGA-France), show that the experimental structure function $D_l(\theta)$ has two variation ranges on which an isoplanatic patch size can be estimated. The interpretation of these two variation ranges can easily be done by the use of a simple model of two thin layers; the associated vertical turbulence C_n^2-profile has been obtained by fitting the experimental data using a procedure proposed by Fried (1977). This estimated vertical C_n^2-profile which, in all cases, imposes the magnitude of the isoplanatic patch, has allowed to compute an estimate of the isoplanatic patch for the angle-of-arrival fluctuations, but also in the framework of speckle interferometry and adaptive optics. For all cases, the estimation is globally of the same order but notably larger than the values reported by other observers. To conclude, we emphasize that anisoplanatism may appear at different scales related to a small number of impulse turbulent layers which forms an equivalent vertical profile. This is important when observing extended astronomical objects at high spatial resolution.

References

Aime C., Kadiri S., Ricort G., Roddier C., Vernin J., 1979, Optica Acta 26, 575–581
Aime C., Kadiri S., Martin F., Ricort G., 1981, Opt. Commun. 39, 287–292
Aime C., Borgnino J., Kadiri S., Martin F., Petrov R., Ricort G., 1986, J. Opt. Soc. Am. 3, 1001–1009
Acton D.S., 1988, in: Von der Lühe O. (ed.) Proc. 10th Sacramento Peak Summer Workshop, High Spatial Resolution Solar Observations, 22–26 August, Sunspot, New Mexico, p. 71
Borgnino J., Martin F., 1977, J. Opt. (Paris) 8, 319–326
Chassat F., 1989, J. Opt. (Paris) 20, 13–23
Druesne P., Borgnino J., Aime C., Petrov R., Kadiri S., 1983, J. Opt. (Paris) 14, 11–17
Foy R., Labeyrie A., 1985, A&A 152, L29–L31
Fried D.L., 1976, SPIE 75, 20–29
Fried D.L., 1977, in: High Angular Resolution Stellar Interferometry, Colloquium no 50 (U.A.I.), 4.1–4.44
Fried D.L., 1979, Opt. Acta 26, 597–613
Fried D.L., 1982, J. Opt. Soc. Am. 72, 52–61
Fugate R.Q., Fried D.L., Ameer G.A., Boeke B.R., Browne S.L., Roberts P.H., Ruane R.E., Tyler G.A., Wopat L.M., 1991, Nat 353, 141–143
Hardy J.W., 1981, in: Dunn R.B. (ed.) Solar Instrumentation: What's Next? p. 421
Laclare F., Merlin G., 1991, C. R. Acad. Sci. (Paris) 313, 323–330
Loss G.C., Hogge C.B., 1979, Appl. Opt. 18, 2654–2661
Murphy E.A., Dewan E.M., Sheldon S.M., 1985, SPIE 551, 156–162

Primmerman C.A., Murphy D.V., Page D.A., Zollars B.G., Barclay H.T., 1991, Nat 353, 141–143
Rimmele T., Von der Lühe O., 1988,in: Von der Lühe O. (ed.) Proc. 10th Sacramento Peak Summer Workshop, High Spatial Resolution Solar Observations, 22–26 August, Sunspot, New Mexico. p. 90
Roddier F., Gilli J.M., Vernin J., 1982, J. Opt. (Paris) 13, 63–70
Scaddan R.J., Walker J.G., 1978, Appl. Opt. 17, 3779–3784
Sechaud M., Fontanella J.C., Rousset G., Primot J., Chassat F., 1990, SPIE 1312, 58–71
Shapiro J.H., 1976, J. Opt. Soc. Am. 66, 469–477
Vernin J., Weigelt G., Caccia J.L., Müller M., 1991, A&A 243, 553–558
Von der Lühe O., 1988, in: Von der Lühe O. (ed.) Proc. 10th Sacramento Peak Summer Workshop, High Spatial Resolution Solar Observations, 22–26 August, Sunspot, New Mexico. p. 147
Walters L., 1985, SPIE 551, 38–41
Welsh B.M., Gardner C.S., 1991, J. Opt. Soc. Am. 8, 69–80
White K.O., Garvey D.M., 1985, SPIE 551, 163–169

ATMOSPHERIC TURBULENCE PROFILE ESTIMATION FROM FLUCTUATION ANALYSIS OF EXTENDED OBJECT IMAGES

A. Bouzid, A. Irbah

Centre de Recherche en Astronomie, Astrophysique et Géophysique, BP 63 Bouzareah, Algiers, 16340, Algeria
E-mail: irbah@unice.fr ; Tel: 213 290 44 54 # 252 Fax: 213 290 44 58

J. Borgnino and H. Lanteri

Université de Nice-Sophia Antipolis, UMR Astrophysique 6525, Parc Valrose F-06108 Nice Cedex 2 France
E-mail: borgnino@unice.fr

ABSTRACT

Atmospheric turbulence is responsible of spatio-temporal fluctuations of astronomical object images obtained by means of ground-based telescopes. The image motion is due to the angle formed by the pupil plane with the wave-front slope all over the pupil. This defines an averaged angle of arrival which may be also considered at each point of the wave-front. Fried [Ref. 1] has established an expression that links between the turbulence "optical strength" $Cn^2(h)$ along an optical path and the spatial structure function $d(\theta)$ of object image fluctuations. The aim of this work is to propose an optical method to estimate the atmospheric turbulence profile. This is based on the inversion of Fried's integral equation which leads to the estimation of vertical turbulence profile from the observed structure function. The inverse problem is linear in Cn^2 but ill-conditioned as it is showed by the singular value decomposition. In order to get stable solution, we use the Marquardt-Levenberg method. Application on synthetic data show the efficiency and the stability of the developed method. We applied then this method to estimate the optical turbulence profile from the analysis of solar images.

Key words : Atmospheric turbulence - Daytime observation - Inverse problem.

1.INTRODUCTION

The terrestrial atmosphere is largely responsible of the degradations observed on the object images recorded with a ground-based telescope. These degradations are more or less important according to the Earth turbulence state in the light of sight at the moment of the observations. In fact, the wave-fronts coming from a point source through the atmospheric turbulent layers are randomly perturbed in space and time which gives a random behavior of the point spread function (*psf*) of the whole system atmosphere-telescope. The angular dependence of the *psf* defines then a precise observation field on the sky over which it can be considered as an invariant. This field size is known as the isoplanatism patch which plays an important role in adaptive optics [Ref. 2, 3, 4, 5] together to the laser guide star techniques [Ref. 6, 7, 8]. The knowledge of this atmospheric parameter is also important in the formalism of the image formation [Ref. 9] or in image restoration techniques [Ref. 10]. The isoplanatism expresses in a general way the similarity of the wave-fronts arriving on the pupil from two point sources separated by an angle θ on the sky and which have traversed different zones of the turbulent atmosphere. Several types of isoplanatism were introduced by Fried [Ref. 11] according if the wave-front (adaptive optics and angle-of-arrival) or the speckle image is considered (speckle interferometry). The angle-of-arrival isoplanatic patch defines the angular field of view on which we can consider that all image points of the object are subjected to the same motion effect resulting from the averaging of the angle-of-arrival fluctuations over the telescope pupil. A model developed by Fried [Ref. 1] links the structure function of these fluctuations to the vertical localization of the turbulence "optical strength" $C_n^2(h)$ (structure constant of the air-refractive-index fluctuation) by an integral equation. The use of this property allows then to estimate the optical turbulence profile $C_n^2(h)$ from the fluctuations observed on an extended object like the Sun [Ref. 12]. This atmospheric parameter is fundamental in adaptive optics since it defines the isoplanatic patch [Ref. 2] and the magnitude of the focus anisoplanatism effect when laser guide stars are used [Ref. 13]. In addition, the localization of the turbulence layers allows the use of multiconjugate adaptive optics in order to correct for low and high altitude contributions to atmospheric distortion on object images [Ref. 14, 15]. The knowledge of this parameter gives also access to the quality of the observations (Fried's parameter r_0 [Ref. 16]) and to the optical transfer function [Ref. 9].

The aim of this paper is to present the method leading to the optical turbulence profile estimations. After a brief recall of the model, the inversion method of the Fried's formula is presented. It is based on the Marquardt-Levenberg method [Ref. 17, 18]. It is developed using synthetic models of $C_n^2(h)$ profile. It is then applied to solar data in order to estimate $C_n^2(h)$ profile for daytime observations. The first results are presented in the last section and discussed.

2. METHOD

2.1. THE ATMOSPHERIC TURBULENCE PARAMETERS

The atmospheric turbulence causes temperature fluctuations along the optical wave-front propagation. Assuming Kolmogorov-Obukhov's laws, the structure function $d_T(\vec{\rho})$ of these fluctuations can be expressed as [Ref. 9] :

$$d_T(\vec{\rho}) = \left\langle \left[T(\vec{r}+\vec{\rho}) - T(\vec{r})\right]^2 \right\rangle = C_T^2 \rho^{\frac{2}{3}} \tag{2.1}$$

where $T(\vec{r})$ is the air temperature at the $\vec{r}$ -position in the atmosphere and C_T^2 the structure constant of temperature fluctuations. Since they induce refractive index variations, an analog equation exists :

$$d_n(\vec{\rho}) = \left\langle \left|n(\vec{r}+\vec{\rho}) - n(\vec{r})\right|^2 \right\rangle = C_n^2 \rho^{\frac{2}{3}} \tag{2.2}$$

where $n(\vec{r})$ is the refractive index at the $\vec{r}$ -position and C_n^2 the structure constant of the refractive index fluctuations. The two structure constants are related by the equation :

$$C_n = 80 * 10^{-6} \frac{P}{T^2} C_T \tag{2.3}$$

where P is the air pressure expressed in millibars and T the temperature in Kelvin degrees.

Due to the refractive index fluctuations along the optical path propagation, the plane wave-front coming from a point source and arriving at the entrance of the telescope pupil will have phase distortions (near field approximation) directly related to the structure constant C_n^2. Different optical parameters are then commonly used to caracterize the wave-front degraded by the atmospheric turbulence. They are the Fried's parameter r_0 [Ref. 16], the characteristic evolution time τ [Ref. 19, 20], the outer coherence scale L_0 [Ref. 21, 22] and the isoplanatic angle θ_{iso} [Ref. 23, 12]. In addition, the angle-of-arrival are also considered and defined as the gradient at each point of the degraded wave-front. The figure 1 shows a wave-front propagation through the atmospheric turbulence and the all defined optical parameters. The image motion is due to the integration of the angle-of-arrival fluctuations over the telescope pupil. Fried [Ref. 11] defined the angle-of-arrival isoplanatism by considering their fluctuation average over the pupil D in two lines of sight separated on the sky by an angle θ. To characterize the isoplanatism, the structure function $d(\theta)$ was used and the formula established as [Ref 1] :

$$d(\theta) = \left\langle \left[\alpha(\xi) - \alpha(\xi+\theta)\right]^2 \right\rangle = D^{-1/3} \int_{path} Cn^2(h).F(h,\theta).dh \tag{2.4}$$

where $\alpha(\xi)$ are the angle-of-arrival fluctuations averaged over the pupil D and coming from a source in the direction ξ. h denotes the altitude and

$$F(h,\theta) = \frac{a}{1+\left(\frac{b.D}{h.\theta}\right)^2} \tag{2.5}$$

where a and b are constants respectively equal to 5.98 and 0.864.

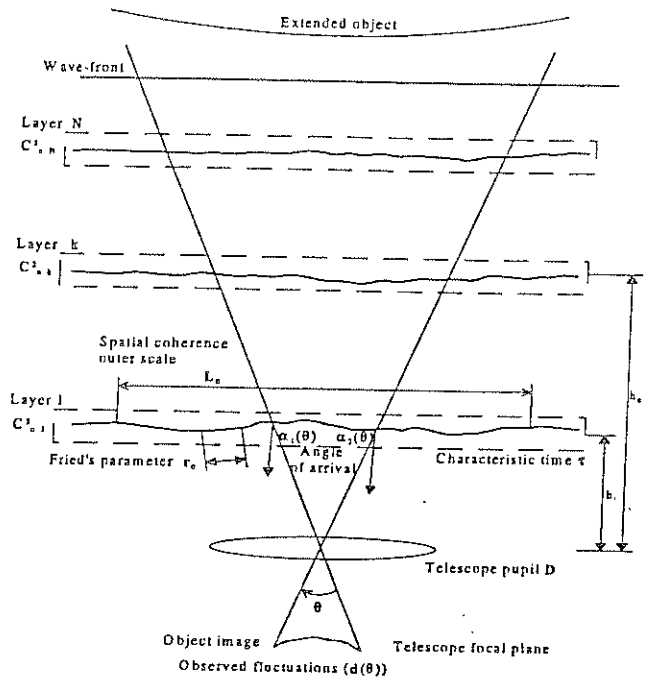


Figure 1 : Wave-front propagation through the atmospheric turbulence and the defined optical parameters. In the figure, the angle-of-arrival $\alpha_1(\theta)$ and $\alpha_2(\theta)$correspond to $\alpha(\xi)$ in the equation (2.4) of the structure function.

2.2. FORWARD PROBLEM

Equation (2.4) shows that the spatial structure function $d(\theta)$ of object image fluctuations observed in the telescope focal plane is linked to the turbulence "optical strength" $C_n^2(h)$ along an optical path by a Fredholm integral equation of first kind.

If we consider that in the neighborhood of the optical path, the atmosphere is a N-layer stratification where each layer j is characterized by a C_{nj}^2 and a thickness $h_j - h_{j-1}$, then the Fried's integral can be written as a matrix equation form :

$$d = F \,.\, C \qquad (2.6)$$

where $d = (d_1, d_2, ..., d_M)^T$ and $C = (C_{n1}^2, C_{n2}^2, ..., C_{nN}^2)^T$ F is a M x N matrix ($M > N$) with the element F_{ij} given by :

$$F_{ij}=aD^{-1/3}\left\{\left(h_j-h_{j-1}\right)-\frac{b.D}{\theta_i}\left[arctg\left(\frac{h_j\theta_i}{b.D}\right)-arctg\left(\frac{h_{j-1}\theta_i}{b.D}\right)\right]\right\} \qquad (2.7)$$

The F matrix linearly links the data d to the model parameter C. The elements of every line-vector say F_i of F matrix represent the contribution of the C_{nj}^2 to the observation d_i.

2.3 INVERSE PROBLEM

To infer the turbulence profile C from the observed structure function d_{obs}, we invert, by using the Marquardt-Levenberg method [Ref. 17,18, 24], the above matrix equation (2.6) which is a linear but ill-posed inverse problem in the sense that small changes in the observations lead to large changes in the parameters C. Since the Marquardt method, as all Newton methods, works well providing that the first estimate (C_0) is not far from the solution, we calculate C_0 by resolving (2.6) in the least-squares sense then we improve it by calculating an amount of C by using an iterative process.

Because F is strongly ill-conditioned, we minimize :

$$L = \| d_{obs} - F.\, C \|^2 + \gamma \| C \|^2 \qquad (2.8)$$

with respect to the parameters C. This leads to the solution :

$$C = (F^T \,.\, F + \gamma I)^{-1} \,.\, F^T \,.\, d_{obs} \qquad (2.9)$$

The parameter γ is used to stabilize and smooth the solution. An appropriate value of γ is then selected to resolve the main features of the solution.

To built an iterative process, we expand the structure function d around the approximated estimate C_0 of the solution :

$$d = d_0 + J \,.\, (C - C_0) \qquad (2.10)$$

In this equation, we have only the fist derivative since d(C) is linear. d_0 corresponds to $d(C_0)$ and J to the Jacobean matrix of partial derivatives of the structure function d with respect to the parameters C defined by :

$$J=\left|\frac{\delta d_i}{\delta C_{n\,j}^2}\right|_{i=1,M\,;\,j=1,N.} \qquad (2.11)$$

It is easy to show that J = F. Thus, to resolve the system:

$$\delta d = F \,.\, \delta C \qquad (2.12)$$

where $\delta d = d - d_0$ and $\delta C = C - C_0$, we use the Marquardt-Levenberg method in which, we minimize the functional :

$$\Phi = \| \delta d - F.\, \delta C \|^2 + \nu^2 \| \delta C \|^2 \qquad (2.13)$$

with respect to the vector δC. Here, ν^2 is the Lagrange multiplier (or *Marquardt parameter*). This leads to the solution :

$$\delta C = (F^T \,.\, F + \nu^2 \,.\, I)^{-1} \,.\, F^T \,.\, \delta d \qquad (2.14)$$

or, at the iteration k+1 :

$$C_{k+1} = C_k + (F^T \,.\, F + \nu^2 \,.\, I)^{-1} \,.\, F^T \,.\, (d_{obs} - F \,.\, C_k) \qquad (2.15)$$

To invert $(F^T \,.\, F + \nu^2 \,.\, I)$ we expand F in a singular value decomposition [Ref. 25]. It yields to :

$$F = U \,.\, S \,.\, V^T \qquad (2.16)$$

where U is a M x N matrix and V is N x N such as $U^T \,.\, U = I$ and $V^T \,.\, V = I$. S is a N x N diagonal matrix of the singular values ($s_1 > s_2 > ... > s_N > 0$).

With some algebra, we can write :

$$C_{k+1} = C_k + V.\, T \,.\, S^{-1} \,.\, U^T (d_{obs} - U \,.\, S \,.\, V^T \,.\, C_k) \qquad (2.17)$$

T is the diagonal matrix of damping factors t_i [Ref. 26] such as :

$$t_i=\frac{s_i^2}{s_i^2+\nu^2} \quad \text{or} \quad t_i=\frac{k_i^2}{k_i^2+\mu^2}$$

where $\mu = \nu/s_1$ is the relative threshold and $k_i = s_i/s_1$.

The matrix T has the interesting property that it damps the small singular values, in comparison with the threshold μ, in order to prevent numerical instabilities due to noise in data or machine zeroing and leads to a stable solution C. Furthermore, to prevent negative parameters when they will become very small, we make the following change of variables $C = \exp(x)$ and $d = \exp(y)$ [Ref. 26]. Thus, this makes J dimension free and makes the problem stable.

3. APPLICATIONS

The Marquardt-Levenberg method presented above is used to invert Fried's formula to restore atmospheric turbulence profile using first synthetic data and then applied to observed structure function deduced from the analysis of solar images.

3.1 SYNTHETIC DATA

In order to study the efficiency and the robustness of the developed method, we perform applications on synthetic data. A C_n^2-profile with two turbulent layers is shown on figure 2. The first one is located at the bottom of the atmosphere with a thickness of 800 m and the higher one of 2000 m thick situated between the altitude 5 and 7 km. The associated structure function was calculated using the forward problem (Fried's formula 2.6) and perturbed by an additive gaussian noise with zero mean and standard deviation of 2%. To infer the turbulence profile from these synthetic data we use a model with twenty layers and an atmosphere of 10 km thick. After 10 iterations we get a good fit between the model response and the synthetic data. The obtained solution shows a smooth turbulent profile which exhibits an increase in C_n^2 value in the bottom (1000 m thick) of the atmosphere and about 6-7 km high. Consequently, we can show that the algorithm allows us to calculate a turbulence profile which is close to the solution. To illustrate the fact that F is strongly ill-conditioned we display on Fig. 3 the structure of the diagonal matrix S. We can clearly see that the most singular values become very small. Thus, they are strongly affected by the noise.

In order to invert synthetic data associated to a realistic turbulent profile, we use the Hufnagel mean turbulent model [Ref. 12] of day-time observations (figure 4). The related synthetic data were calculated by the forward problem and perturbed with gaussian noise of zero mean and 2% standard deviation. The figure 4 shows the solution obtained for a twenty layer model after 10 iterations. This solution restitutes well the two levels of turbulence located at the bottom of the atmosphere and

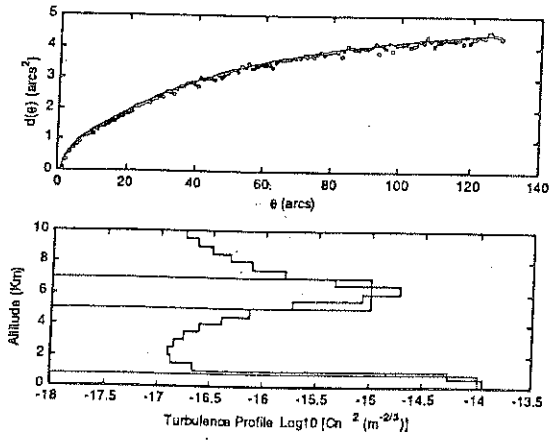


Figure 2 : Solution to fitting a synthetic data corrupted with 2% noise level. In the bottom: solution obtained after 10 iterations (solid line) with comparison with the theoretical model (dashed line) used. In the top: The fit obtained between the data observed (dots) and data predicted (solid line)..

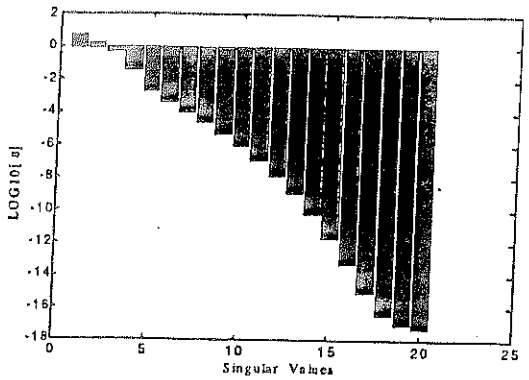


Figure 3 : Singular values structure of the diagonal matrix S obtained by singular value decomposition of F of the model showed in fig. 2.

at about 10 km high. However, the turbulent layers located near the earth surface (first kilometers) are well reconstructed contrarily to the higher ones which need some iterations to be restituted. Moreover, these later layers are more sensitive to noise. Thus, if the noise level is high we have to increase the threshold μ to avoid numerical instabilities due to the noise but, unfortunately, this makes difficulties to restore the higher turbulent layers.

Applications on synthetic data show that the method works efficiently if the problem is well parameterized. That is the appropriate number of layers, atmosphere thickness and threshold values must be well selected. A few layer model leads to stable inverse but can not resolve thick layers. In the opposite, when the layer number is chosen very large in order to resolve the thick layers, it produces numerical instabilities in the solution. Between these two extreme limits, we should find the appropriate number of layers which allows us to recover the fine features of the turbulence profile without instabilities .

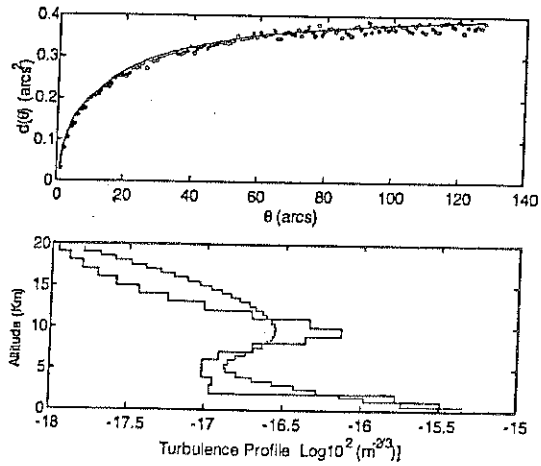


Figure 4 : In the bottom is represented the solution (solid line) obtained after 10 iterations in comparison with the Hufnagel mean profile (dashed line). The top of the figure shows the obtained fit.

The same problem occurs with the choice of the threshold μ. A compromise should be found between a large value that leads to stable but very smooth solution without fine features and very small one, which produces instabilities in the solution. We establish a threshold that decreases with iteration k

$$\mu_k = \mu_1 \cdot \alpha^{1-k}$$

in which μ_1 and α values depend basically on the noise level. The inversion of synthetic data shows that μ_1 is approximately equal to the noise level. The α parameter defines the manner on how μ_k decreases when the iteration number increases. If the data are slightly corrupted by noise then a great value of α is adopted which allows to resolve the finest features of the solution.

3.2 ESTIMATION OF THE TURBULENCE PROFILE FROM THE ANALYSIS OF SOLAR IMAGES

After studying the efficiency and the robustness of the Marquardt-Levenberg method to invert a synthetic data and how the parameterization of the problem affect the solution, we applied the method to real data obtained from the analysis of solar images. Thus, two sets of day-time observations were used to calculate the turbulence optical strength C_n^2. These observations have been performed in June 1990 using the solar astrolabe of the Calern Observatory (Observatoire de la Côte d'Azur, France) [Ref. 12]. The instrument has an elliptic objective with major axis of 8 cm and the minor of 5 cm. The first analyzed data file shows a corrupted structure function by the noise (fig. 5). An accepted fit between data and the response corresponding to 40 layer model is obtained after 7 iterations. The solution displays turbulent profile dominated by two main layers.

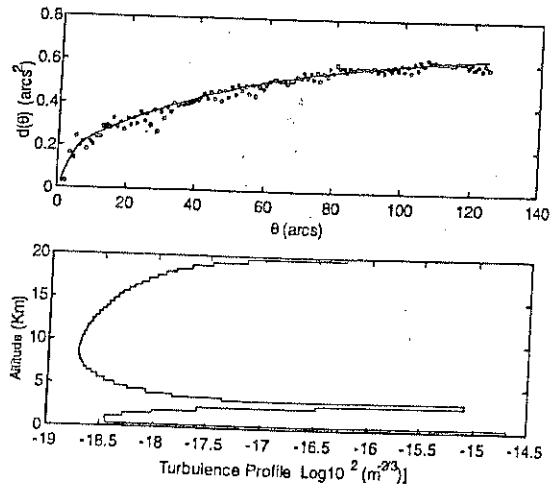


Figure 5 : Result of a real data set inversion. In the top, the obtained fit from the observed structure function deduced from the solar image analysis. In the bottom, the solution after 7 iterations.

In the bottom of the profile, a layer of 400 m thick and $C_n^2 = 2.04\ 10^{-15}\ m^{-2/3}$ is obtained. The second layer is located at 3000 m high with a C_n^2 peak value of $8.16\ 10^{-16}\ m^{-2/3}$.

In fig. 6, we show the solution obtained after 8 iterations by inversion of the observed structure function of another data set performed the same day 2 minutes later. We use a 50-layer model of equal thickness of 200 m. The turbulence profile is also dominated by two turbulent levels. At the bottom of the atmosphere, it exhibits a layer of 400 m thick and a C_n^2 equal to $1.1\ 10^{-15}\ m^{-2/3}$. At the higher altitude (1700 m), the solution displays a 1400 m thick layer with a C_n^2 peak value of $1.7\ 10^{-16}\ m^{-2/3}$.

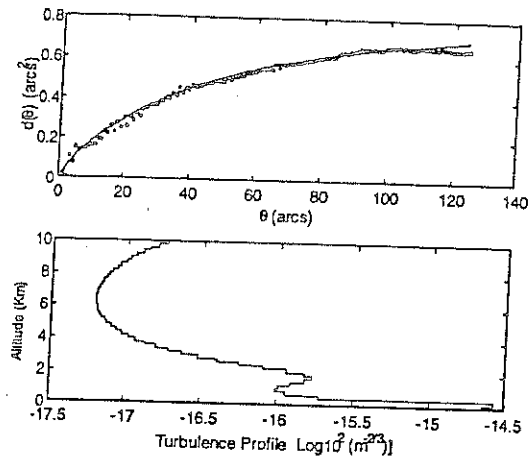


Figure 6 : Inversion result of a second real data set recorded the same day 2 minutes later. In the top, the obtained fit from the observed structure function deduced from the solar image analysis. In the bottom, the solution after 8 iterations.

4. DISCUSSION

The Marquardt algorithm [Ref. 17] was implemented and used to calculate the atmospheric turbulence C_n^2-profile from the structure function $d(\theta)$ of angle of arrival fluctuations by inverting the Fried's integral equation.

The results obtained with synthetic data show that the algorithm converges quickly to stable solution in few iterations (fig. 2 and 4). However, a well parameterization of the problem should be used to found a good solution. That is an optimum value of the threshold μ, the atmosphere thickness and the layer number have to be selected. Unfortunately, if the noise level is high corresponding to dirty data, this leads to unstable solution. To stabilize the solution, we have to rise the threshold value and consequently the fine features of the turbulent profile are lost. Thus, to

recover the subtle features of the C_n^2-profile, the data have to be as clean as possible.

Application on observed data (fig. 5 and 6) obtained from the analysis of solar images leads to solutions with turbulent C_n^2-profile dominated by two turbulent levels both situated in the first kilometers of the atmosphere. One of them is located in the bottom with few hundreds of meters thick. The second one is situated at 2 to 3 km high. These results are in good agreement with those obtained by Irbah et al. [Ref 12] who used same data. The fact that data are corrupted by so high noise level does not allows us to recover the more fine features of the solution obtained.

5. CONCLUSION

The developed method allows us to invert the integral Fried's formula in order to infer the atmospheric turbulence C_n^2-profile from the fluctuation analysis of extended object images.

The method was then applied on synthetic data which show that the inversion algorithm is robust and converge in few iterations to a stable solution. However, if the data are clean in the sense that they are slightly corrupted by noise, it will be possible to recover the fine features of the solution. Also, the method was applied to estimate the atmospheric turbulence C_n^2-profile from the analysis of solar images. The solutions obtained are in good agreement with results obtained in previous study.

REFERENCES

1. Fried D. L., 1977, in : *High Angular Resolution Stellar Interferometry*, Colloquium n° 50 (U.A.I.), 4.1-4.44.
2. Molodij G. and Rousset G., 1997, J. Opt. Soc. Am. A 14, 8, 1949-1966
3. Chassat F., 1992, Thesis, Propagation optique à travers la turbulence. Etude modale de l'anisoplanétisme et application à l'optique adaptative, Univ. Paris - Sud Orsay, France
4. Welsh B. M. and Gardner C. S., 1991, J. Opt. Soc. Am. 8, 69-80
5. Séchaud M., Fontanella J. C., Rousset G., Primot J., Chassat F., 1990, SPIE 1312, 58-71
6. Fugate R. Q., Fried D. L., Ameer G. A., Boeke B. R., Browne S. L., Roberts P. H., Ruane R. E., Tyler G. A. and Wopat L. M., 1991, Nature (London) 353, 144-146
7. Primmerman C. A., Murphy D. V., Page D. A., Zollars B. G., Barclay H. T., 1991, Nature (London) 353, 141-143
8. Foy R. and Labeyrie A., 1985, Astron. Astrophys., 152, L29-L31
9. Roddier F., 1981, Progress in Optics, 19, E. Wolf (ed), North-Holland publishing Co Amsterdam,
10. Von der Lühe, 1993, Astron. Astrophys., 268, 374-390
11. Fried D. L., 1976, SPIE 75, 20-29
12. Irbah A., Borgnino J., Laclare F. and Merlin G. 1993, Isoplanatism and high spatial resolution solar imaging, Astron. Astrophys., 276, 663-672.
13. Fried D. L. and Belsher J. F., 1994, J. Opt. Soc. Am. A 11, 1, 277-287
14. Johnston D. C. and Welsh B. M., 1994, J. Opt. Soc. Am. A 11, 1, 394-408
15. Beckers J. M., 'increasing the size of the isoplanatic patch with multiconjugate adaptive optics" in *Very Large Telescopes and their Instrumentation*, M. H. Ulrich ed., European Southern Observatory Proceeding N°30, (European Southern Observatory Garching bei München, Germany), 1988, 693-703
16. Fried D. L., 1966, J. Opt. Soc. Am. 56, 1372-1380.
17. Marquardt D. W. 1963, An algorithm for least-square estimation of non-linear parameters, J. SIAM, 11, 431-441.
18. Levenberg K. 1944, A method for the solution of certain non-linear problems in least-squares, Quarterly of Applied Mathematics, 2, 164-168.
19. Roddier F., Gilli J. M. and Lund G., 1982, J. Opt. (Paris) 13, 263,-271.
20. Aime C., Borgnino J., Martin F., Petrov R., Ricord J. and Kadiri S., 1986, J. Opt. Soc. Am. 3, 7, 1001-1009
21. Tatarski V. I., 1971, "Effects of the Turbulent Atmsophere on Wave Propagation", Isarel Program of Scientific Translation, Jerusalem.
22. Borgnino J., 1990, Applied Optics, 29, 13, 1863-1865
23. Roddier F., Gilli J. M. and Vernin J., 1982, J. Opt. (Paris) 13, 2, 63,-70
24. Menke, W. 1984, Geophysical data analysis, Academic press inc.
25. Lanczos C. 1958, Linear Systems in self-adjoint form, Am. Math. Monthly, 65, 665-679.
26. Jupp D. L.B. and Vozoff K. 1975, Stable iterative methods for inversion of geophysical data, Geoph. J. Roy. Astro. Soc., 42, 957-976.
27. Penrose R. 1955, A generalized inverse of matrices, Proc. Camb. Phil. Soc., 51, 406-413.

AKNOWLEDGEMENTS

This work has been performed with support of the *Observatoire d'Alger* (CRAAG) and the French Foreign Affaire Ministry in the framework of scientific cooperation between France and Algeria (contract 96MDU357)

ASTRONOMY & ASTROPHYSICS
SUPPLEMENT SERIES

Astron. Astrophys. Suppl. Ser. 138, 155–162 (1999)

Error due to atmospheric turbulence effects on solar diameter measurements performed with an astrolabe

L. Lakhal[1], A. Irbah[1], M. Bouzaria[1], J. Borgnino[2], F. Laclare[3], and C. Delmas[3]

[1] C.R.A.A.G, Observatoire d'Alger, BP. 63, Bouzaréah Alger, Algeria
e-mail: irbah@unice.fr
[2] Université de Nice-Sophia Antipolis, UMR 6525 Astrophysique, Parc Valrose, F-06108 Nice Cedex 2, France
[3] Observatoire de la Côte d'Azur, Département C.E.R.G.A, Avenue Copernic, F-06130 Grasse, France

Received March 15; accepted May 26, 1999

Abstract. Diameter measurements performed with the solar astrolabe are affected by instrumental and atmospheric effects. The problem is to know how these effects contribute to the error on diameter measurements. Thus, a numerical simulation is developed to bring some responses to this problem. For this purpose, synthetic images of the Sun similar to the ones obtained by the instrument through the Earth atmosphere are simulated. A fractal model is used to generate randomly perturbed wavefronts and therefore optical response of the whole system, atmosphere and instrument. Many sequences of solar images are then simulated for various observation conditions (Fried's parameter r_0, spatial coherence outer scale L_0 and atmospheric characteristic times). They are used to define the time of contact of the direct and reflected solar images which is fundamental in the solar astrolabe experiment. It is then studied as a function of the observation conditions relatively to the experimental characteristics (exposure time).

Key words: Sun: fundamental parameters — atmospheric effects — methods: numerical

1. Introduction

Many authors reported and discussed variations observed in the Sun's diameter measurements performed during the last three centuries (Toulmonde 1997). These results added greater interests to the solar diameter measurements and long term variations. Thus, many programs were born for solar geometry goals. Visual and photoelectric measurements have been made using instruments dedicated to the solar diameter measurements (Brown et al. 1982; Bode et al. 1995; Laclare 1983; Laclare et al. 1980, 1996; Neckel 1995; Wittmann 1997; Wittmann et al. 1981, 1991). The mean values of solar radius reported from these programs were dispersed. The difference lied between a few tenths to more than two arcseconds. Moreover, variations have not always been noted from the observation series of the solar programs. Using the observations recorded with the solar diameter monitor (Brown et al. 1982) during the period 1982 to 1987, Brown & Christensen-Dalsgaard (1998) did not observe any variations. In their work, they used special methods in order to eliminate some atmospheric effects. However, in opposite, variations were observed in diameter measurements performed with the solar astrolabe (Delache et al. 1985; Laclare et al. 1996).

The astrolabe experiment of Calern Observatory (France) has begun in 1975, when the first measurements were obtained. Since the beginning of the solar program up to now, visual observations were made regularly while the CCD ones began in 1988. Figure 1 represents the visual solar data recorded at Calern Observatory astrolabe during the period 1975 to 1996. It is clearly shown an oscillation with a period of about ten years corresponding probably to the solar cycle but in opposite phase. Others new solar astrolabe programs have been then developed from these new exciting results (Laclare et al. 1996; Leister & Benevides Soares 1990; Noël 1995; Sanchez et al. 1995). Several studies were also developed in order to analyze (Moussaoui et al. 1998; Delache et al. 1985; Gavryusev et al. 1994) and to valide the recorded data (Laclare et al. 1996; Irbah et al. 1994). For this purpose and to improve the astrolabe experiment, all effects which are able to cause variations or degradations of the solar data, are required to be studied.

The present work is a study of the instrumental and atmospheric turbulence effects to the contribution to diameter measurement errors when observing with a solar astrolabe. It is developed using a numerical

Send offprint requests to: J. Borgnino

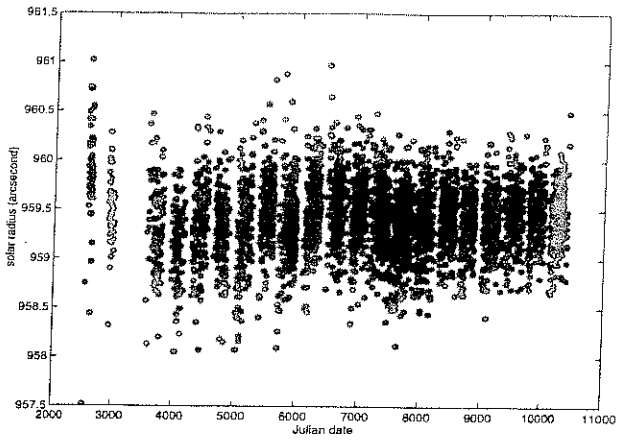


Fig. 1. Solar radius measurements obtained using the Calern Observatory astrolabe during the period 1975 to 1996

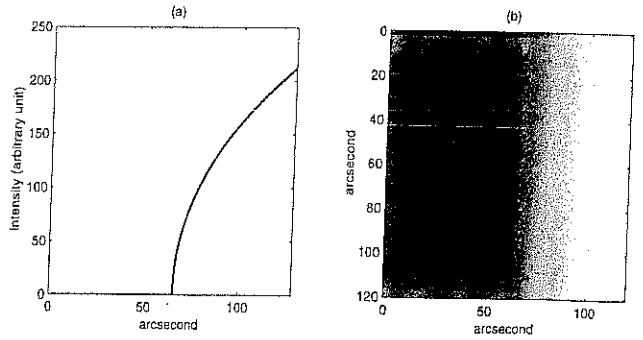


Fig. 2. Solar limb darkening function a) and the synthetic image of the sun b)

simulation where the principal atmospheric parameters are introduced. The effect of each parameter is studied separately in order to evaluate its proper contribution to the global diameter error. Section 2 presents the simulation of solar images as observed at the astrolabe through the atmospheric turbulence. In the simulation, a fractal model is used to generate randomly perturbed wavefronts and therefore point spread functions (psf) of the whole atmosphere-instrument. In Sect. 3, we present the steps leading to the instant of the Sun transit by the small circle needed for the diameter measurement with the astrolabe. Finally, we expose and discuss the results obtained for the contribution of each atmospheric parameter to the error on the diameter estimation.

2. Synthetic images as observed at the solar astrolabe

In this section, solar images with similar characteristics as those recorded at the astrolabe through the atmospheric turbulence are simulated. The optical response of the whole system atmosphere and instrument is then calculated using a fractal model to generate the randomly perturbed wavefronts. It is used to build solar images in various seeing conditions and with different exposure times. Let us first present the synthetic image of the Sun which is needed for the simulation.

2.1. Synthetic image of the Sun

Several models of the solar limb darkening function exist. The model we use to build the synthetic image of the Sun is given by (Allen 1973):

$$O_\lambda(\alpha) = O_\lambda(0)\left[1 - u_2 - v_2 + u_2\cos(\alpha) + v_2\cos^2(\alpha)\right] \quad (1)$$

where $O_\lambda(\alpha)$ is the intensity of the solar continuum at an angle α from the centre of the disk. α represents the angle between a Sun's radius vector and the line of sight. $\alpha = 0$ corresponds to the centre of the disk and $\alpha = \frac{\pi}{2}$ to the solar edge. The ratio $\frac{O_\lambda(\alpha)}{O_\lambda(0)}$, which varies with the wavelength λ defines the limb darkening. For the used observation wavelength ($\lambda = 0.55\ \mu$m), the constants u_2 and v_2 are respectively equal to 0.93 and -0.23. The plot in Fig. 2a shows the solar limb darkening function where the intensity was normalized between 0 and 255 for our needed calculations. The Fig. 2b represents a solar image sample where the field size is equal to 128 by $128''^2$.

2.2. Simulation of the optical response of the whole system, atmosphere and instrument using a fractal model

The psf of the whole system instrument and atmosphere is needed to generate the solar image sequences as recorded through the atmosphere in various observation conditions. We present first, the fractal model used to generate the two-dimensional randomly perturbed wavefronts and then the deduced optical responses.

2.2.1. The randomly perturbed wavefront synthesis using a fractal model

The turbulence follows a fractal structure. The model used to generate the randomly perturbed wavefront function φ is based on a mid point displacement algorithm (Lane et al. 1992; Beaumont et al. 1996). To simulate a L by L phase screen, the first step is to choose three points ϕ_1, ϕ_2 and ϕ_3 disposed at the summits of an isoceles triangle with base and height equal to $2L$ (Fig. 3). Phase function values at these points are Gaussian random variables with zero means and with variances given by:

$$\sigma^2(\phi_1) = D_\phi\left(\sqrt{5}L\right) - \frac{1}{2}D_\phi(2L) \quad (2)$$

and

$$\sigma^2(\phi_2) = \sigma^2(\phi_3) = \frac{1}{2}D_\phi(2L) \quad (3)$$

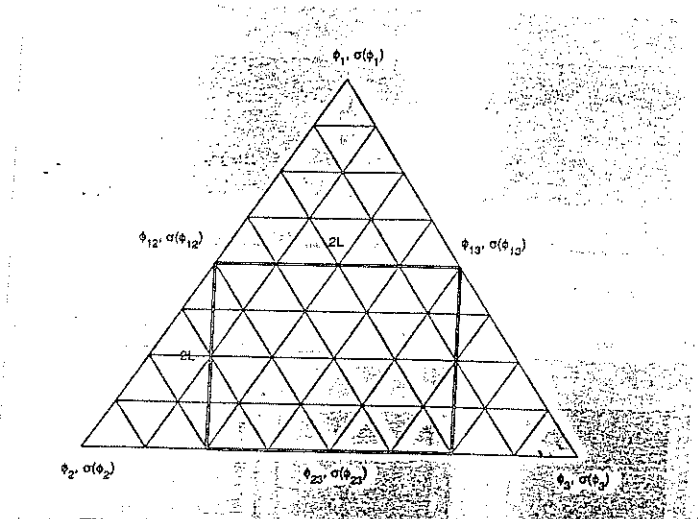


Fig. 3. The fractal interpolation grid used to generate the perturbed wavefronts

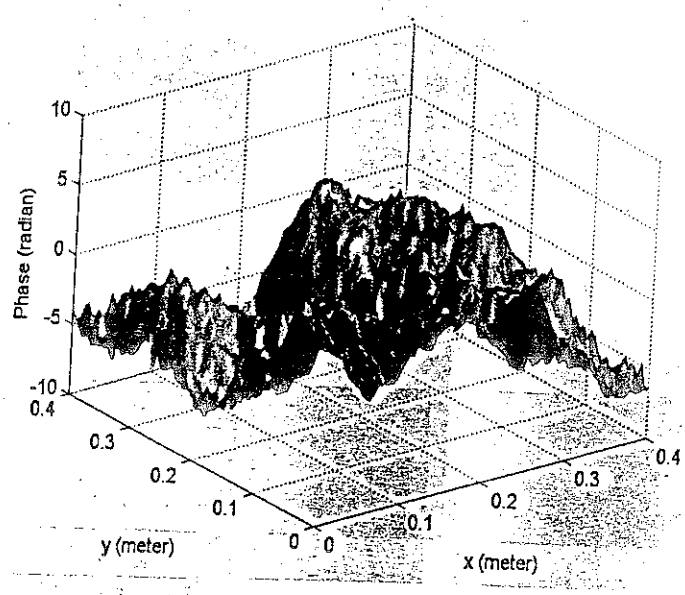


Fig. 4. Perturbed wavefront sample generated for $r_0 = 4$ cm and L_0 infinite

where $D_\phi(r) = \left\langle |\varphi(x) - \varphi(x+r)|^2 \right\rangle = 6.88 \left(\frac{r}{r_0}\right)^{\frac{5}{3}} *$

$$\left[1 - 1.485 \left(\frac{r}{L_0}\right)^{\frac{1}{3}} + 5.383 \left(\frac{r}{L_0}\right)^{2} - 6.281 \left(\frac{r}{L_0}\right)^{\frac{7}{3}}\right] \quad (4)$$

$\langle\ \rangle$ denotes a mean average. $D_\phi(r)$ is the phase structure function deduced from the Kolmogorov's law and the von Karman model (Ziad 1993). r_0 is the Fried's parameter which qualifies the observations (seeing) (Fried 1966) and L_0 the spatial coherence outer scale of the wavefronts (Borgnino 1990).

Equations (2), (3) and (4) show that ϕ_1, ϕ_2 and ϕ_3 follow the theoretical phase structure function deduced from the Kolmogorov turbulence law since:

$$\left\langle |\phi_1 - \phi_2|^2 \right\rangle = \left\langle \left|\varphi(x) - \varphi(x+\sqrt{5}L)\right|^2 \right\rangle = D_\phi\left(\sqrt{5}L\right) \quad (5.1)$$

$$\left\langle |\phi_3 - \phi_1|^2 \right\rangle = \left\langle \left|\varphi(x) - \varphi(x+\sqrt{5}L)\right|^2 \right\rangle = D_\phi\left(\sqrt{5}L\right) \quad (5.2)$$

$$\left\langle |\phi_3 - \phi_2|^2 \right\rangle = \left\langle |\varphi(x) - \varphi(x+2L)|^2 \right\rangle = D_\phi(2L)\,. \quad (5.3)$$

Three new points ϕ_{12}, ϕ_{13} and ϕ_{23} of the phase screen are generated midway between each existing points by a process of linear interpolation and addition of independent random variables ε_1, ε_2 and ε_3, such as:

$$\phi_{12} = \frac{1}{2}(\phi_1 + \phi_2) + \varepsilon_1 \quad (6.1)$$

$$\phi_{13} = \frac{1}{2}(\phi_1 + \phi_3) + \varepsilon_2 \quad (6.2)$$

$$\phi_{23} = \frac{1}{2}(\phi_2 + \phi_3) + \varepsilon_3 \quad (6.3)$$

$$\sigma^2(\varepsilon_1) = \sigma^2(\varepsilon_2) = D_\phi\left(\frac{\sqrt{5}}{2}L\right) - \beta D_\phi\left(\sqrt{5}L\right) \quad (7.1)$$

and

$$\sigma^2(\varepsilon_3) = D_\phi(L) - \beta D_\phi(2L) \quad (7.2)$$

where β is a semi-empirical coefficient equal to 0.25.

The iterative procedure interpolation/displacement is then repeated in each new generated triangle until the desired numbers of samples are obtained. The needed L by L phase screen is extracted from the middle of the base of the original isoceles triangle (Fig. 3). The Fig. 4 shows the simulation of a perturbed wavefront sample using the model. It is simulated for a Fried's parameter r_0 equal to 4 cm and a spatial coherence outer scale supposed infinite.

2.2.2. The simulated point spread function

The psf S of the whole system telescope and atmosphere is given by the square modulus of the Fourier Transform (FT) of the complex amplitude Ψ limited to the pupil area:

$$S(\vec{\theta}) = \left[FT_{\text{pupil}}\left(\Psi\left(\vec{\xi}\right)\right)\right]^2 \quad (5)$$

where

$$\Psi\left(\vec{\xi}\right) = \exp\left(i\varphi\left(\vec{\xi}\right)\right).$$

Equation (8) assumed the near field approximation (Roddier 1981). φ is the turbulent phase generated with the fractal model, $\vec{\xi}$ is the angular frequency vector considered in the pupil plane and $\vec{\theta}$ the angular coordinate vector in the focal plane.

$S(\vec{\theta})$ corresponds to an image of speckles. In Fig. 5 are represented four typical short exposure speckle images obtained using the procedure developed in the previous section. They are simulated for Fried's parameters r_0 equal

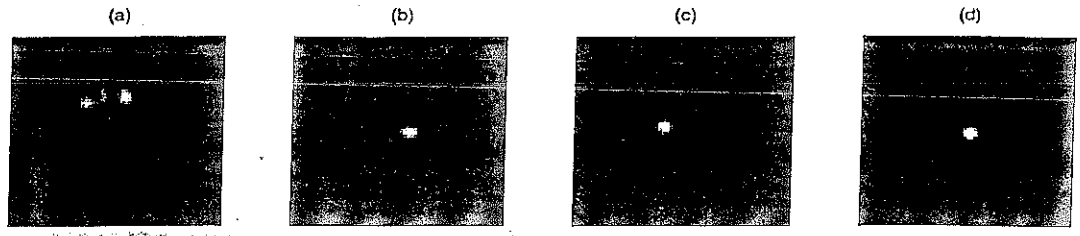


Fig. 5. Speckle images obtained from the fractal model. The image field is equal to 64 by $64''^2$ and the Fried's parameter equal respectively to 2 a), 4 b), 6 c) and 10 cm d)

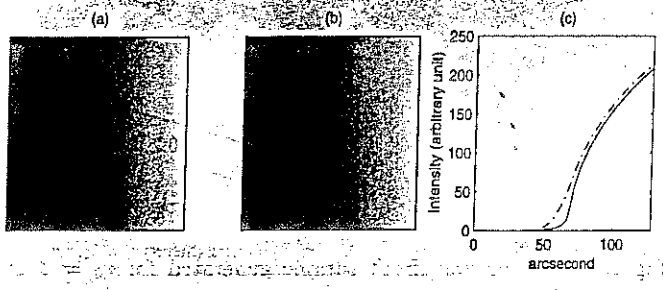


Fig. 6. Simulated solar images recorded with a short exposure time and r_0 equal to 3 a) and 7 cm b). Solar limbs extracted from images recorded in these seeing conditions (dashed line: $r_0 = 3$ cm and solid line: $r_0 = 7$ cm) c)

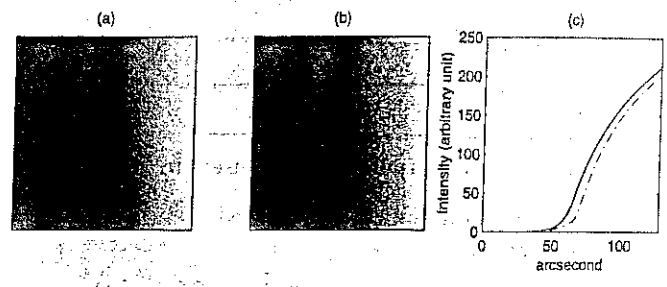


Fig. 7. Simulated solar image recorded in same seeing conditions ($r_0 = 5$ cm) but with different exposure times ($t \leq \tau$ a) and $t \gg \tau$ b)). Solar limbs extracted from images recorded with exposure time respectively lower (solid line) and higher (dashed line) than the atmospheric characteristic time τ c)

respectively to 2, 4, 6 and 10 cm and with a pupil aperture D equal to 10 cm. The spatial coherence outer scale of the used randomly perturbed wavefronts has an infinite value. Large boiling and displacements of the speckle centroids are observed for small values of r_0 while for r_0 equal to the pupil aperture, the speckle image is similar to the diffraction pattern of the instrument.

We are then able to simulate psf's of the whole system telescope and atmosphere in various seeing conditions and also for different integration times (average of short exposure samples).

2.3. Simulation of recorded solar images in various observation conditions

Solar images as recorded through the terrestrial atmosphere are simulated. Assuming isoplanatism, a solar image is obtained by the convolution of the synthetic image of the Sun (see Sect. 2.1) with the psf of the imaging system (atmosphere and telescope):

$$I(\vec{\theta}) = O(\vec{\theta}) \otimes S\left(\vec{\theta}\right) \quad \text{with} \quad \left|\vec{\theta}\right| \leq \theta_0 \tag{6}$$

where $\otimes$ is the convolution symbol and θ_0 the isoplanatic angle.

We use this formalism to build solar images recorded in various seeing conditions and with different CCD integration times. The spatial coherence outer scale of the generated perturbed wavefronts is infinite. The pupil aperture D and the observation wavelength are respectively taken equal to 10 cm and 0.55 μm. These kind of images will be useful in the next section to develop the error study on solar diameter measurement. They have similar properties as those recorded with the solar astrolabe (Laclare et al. 1996; Laclare & Merlin 1991).

2.3.1. Solar images recorded in different seeing conditions but with a short exposure time

In this case, solar images are simulated using various Fried's parameters r_0 (Fig. 6) but integration times short enough to freeze the turbulent motion of the atmosphere i.e. the integration time t is less than the characteristic evolution time of the atmosphere τ (Aime et al. 1986). For a given simulated image sequence, Fried' s parameter r_0 remains constant but images are obtained with independent psf's.

2.3.2. Solar images recorded in same seeing conditions but with different exposure times

Long exposure solar images are obtained by the average over a great number of short exposure frames. The integration time t of the long exposure images is then equal to $n\tau$ where n is the number of averaged images and τ the atmospheric characteristic time. Figure 7 shows the simulated solar images recorded in same seeing conditions ($r_0 = 5$ cm) but with different integration times.

3. Error on the diameter measurements performed with a solar astrolabe. Results and discussion

We use in this section, the previous developments to study the error behavior of solar diameter measurements performed with a solar astrolabe in various seeing conditions

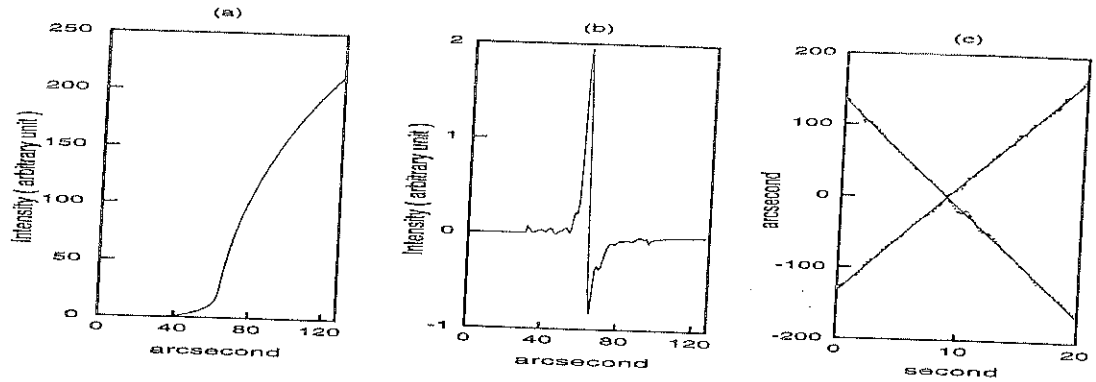


Fig. 8. Analysis of an image sequence composed of short exposure frames recorded for a Fried's parameter equal to 3 cm. a) Typical simulated solar limb extracted from a solar image. b) Second derivative of the solar limb function and definition of the inflexion point. c) Reconstructed trajectories of both direct and reflected solar images approximated by straight lines using least-square fits

ıd for different integration times of the CCD camera. It is useful to recall first the basic properties of the solar astrolabe experiment.

3.1. The solar astrolabe experiment

he diameter measurement principle consists in the determination of the time transits of the solar edges by the small circle localized at an altitude Z defined by the angle the astrolabe prism (Laclare 1983). The solar diameter deduced from the time interval between the two solar limb transits by the same small circle. Near the transit of e Sun by the small circle, the astrolabe gives two images of the object: a direct and a reflected ones. Each of them moves in the astrolabe focal plane due to the diurnal motion. The instant when the solar edge crosses the nall circle corresponds to the contact of the two images. ın the solar experiment, each solar image is formed on a CCD camera using a rotating shutter (Laclare & Merlin 991). The solar image is analyzed by the acquisition system which extracts in real time, the solar edge. The edge is determined by the inflexion points of the solar limb function given by each image line.

For one solar image, the recorded data represent the solar edge associated to the corresponding time acquisition. For each solar edge transit by the small circle, data nsist in a sequence of about 100 images recorded dur-g about 20 seconds. The solar trajectory is determined from the data for both direct and reflected images. The tersection point of the trajectories gives the time when ıe solar edge crosses the small circle.

2. Simulation of solar data recorded in various observation conditions

To simulate observations at the astrolabe, solar image sequences recorded in various observation conditions are needed. For given observation conditions, a simulated sequence is constituted with 50 direct images and 50 reflected ones. Each simulated solar image has a size of 128 by $128''^2$. The pupil aperture D and the observation wavelength are also respectively equal to 10 cm and 0.55 μm. A Sun mean velocity of $15''$ by second of time is taken in order to introduce the diurnal motion. To each solar image is associated a recorded time taking in reference the first simulated one. The acquisition sampling is fixed to 20 seconds. Each solar image of the sequence is then analyzed and the solar edge extracted. As in the solar experiment, the edge is defined as the zero of the second derivative of each solar limb function assimilated to an image line. The edge associated to the corresponding time allows to build the trajectories for both direct and reflected solar images. The trajectories are after that approximated by straight lines using least-square fits and the desired intersection point so determined (Fig. 8).

3.3. Results and discussion

Since the diameter measurement is deduced from the two instants of the solar edge transit by the small circle, we will develop our error study around the time transit behavior. Using the previous developments, many sequences of solar images have been simulated in various observation conditions (Fried's parameter r_0, outer scale L_0, exposure time t) (see Sect. 2.3). The sequence analysis leads to the transit time of the Sun by the small circle directly linked to the observation conditions. Thus, because of temporal fluctuations observed on the trajectories, the time transit is not well defined (Irbah et al. 1994). We define the error Δt associated to the transit time t_0 as:

$$\Delta t = |t_0 - t_{\text{true}}| \tag{7}$$

where t_{true} denotes the true contact time of solar images obtained in ideal seeing conditions.

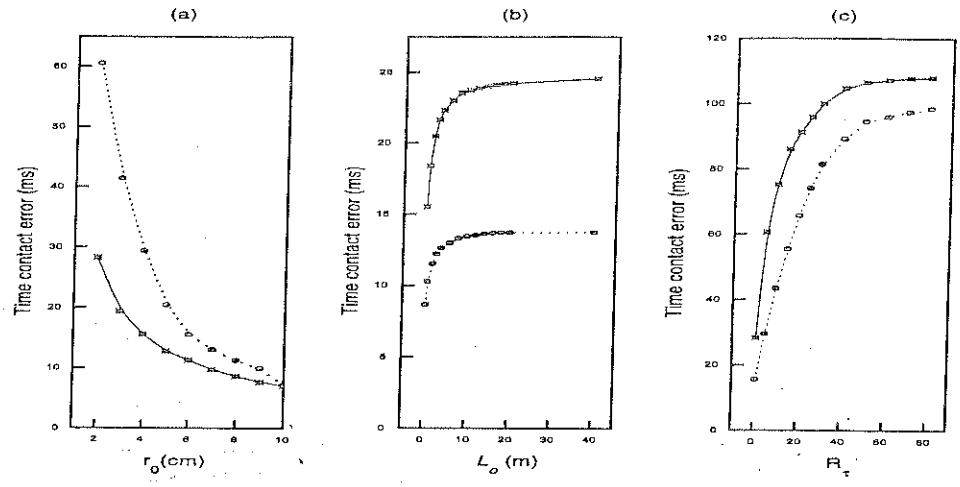


Fig. 9. Time contact error with: **a)** the seeing (-*: short and .●.: long exposure frames), **b)** the outer scale L_0 (-*: $r_0 = 2$ cm and .●.: $r_0 = 4$ cm) and **c)** the parameter R_τ (-*: $r_0 = 2$ cm and .●.: $r_0 = 4$ cm) (see text)

We will now analyze the error behavior with the observation conditions.

3.3.1. Error due to the seeing

Solar image sequences composed of short and long exposure frames are used to study the error behavior with the seeing. They are simulated for various seeing conditions and supposing an infinite outer scale of the randomly perturbed wavefronts. For a given Fried's parameter r_0, the error Δt is determined over an average of 50 transit times deduced from each kind of the simulated solar sequences. The plot of the Fig. 9a shows the error behavior with the seeing as obtained from the simulation. In each case, a decrease of the error with good seeing conditions is observed. The use of long exposure frames in the experiment gives however, a greater error on the time contact than when using short exposure frames. This is better observed on the figure for poor seeing conditions. Indeed, in case of short exposure frames, the error is greater than 28 ms when the r_0 value is about 2 cm and falls down to about 13 ms for r_0 equal to 5 cm (see Table 1). The precision improvement is then equal to 54%. The error still decreases to about 9 ms for r_0 equal to 8 cm and improves the precision of about 68%. When using long exposure frames, the error which is equal to 61 ms when r_0 is equal to 2 cm, falls down to about 20 ms for r_0 equal to 5 cm. The precision improvement is then equal to 67%. The error decreases to about 11 ms for r_0 equal to 8 cm which gives a precision improvement of about 82%.

For mean seeing conditions at Calern Observatory ($r_0 = 4$ cm) (Irbah et al. 1994), the error is about 16 ms if short exposure frames are used and about 29 ms in case of long exposure frames. According to the considered Sun mean velocity (see Sect. 3.2), the error on the solar diameter measurement is respectively equal to 0.5″ and 0.9″ when short and long exposure frames are used (see Table 2).

3.3.2. Error due to the spatial coherence outer scale of the perturbed wavefronts

To study this effect, image sequences composed of short exposure frames recorded in same seeing conditions are generated for different spatial coherence outer scales. The error Δt is determined over an average of 30 transit time samples. The Fig. 9b represents the time contact error behavior with the outer scale L_0 in two different seeing conditions ($r_0 = 2$ and 4 cm). In each case, the error increases with the outer scale L_0 in order to reach a limit value. It is also observed from the figure that this parameter has a significant effect only when it has small values ($L_0 \leq 8$ m). It is limited after that by the error induced by the seeing. For the mean seeing conditions of the Calern Observatory, the error on the time transit is respectively equal to about 12 and 13 ms for L_0 equal to 2 and 8 m (see Table 1). It remains then constant to about 14 ms when L_0 values are greater than 20 m. This corresponds to an error on the solar diameter measurement of about 0.1″ when L_0 takes values from 2 to 20 m (see Table 2).

3.3.3. Error due to the exposure time relatively to the observation conditions

A similar study has been also developed using sequences simulated in case of different exposure times relatively to the turbulence characteristic time. The outer scale is supposed infinite and two seeing conditions are considered ($r_0 = 2$ and 4 cm). We define the parameter R_τ as the ratio between the exposure time and the characteristic time. The Fig. 9c shows the time difference Δt behavior with the

ible 1. Error on the time contact

r_0 (cm)	Δt (ms) (L_0 infinite)		L_0 (m)	Δt (ms) ($R_\tau \leq 1$)		R_τ	Δt (ms) (L_0 infinite)	
	$R_\tau \leq 1$	$R_\tau \succ 1$		$r_0 = 2$ cm	$r_0 = 4$ cm		$r_0 = 2$ cm	$r_0 = 4$ cm
2	28.2	60.5	0.5	15.5	8.7	1	28.2	15.5
3	19.3	41.4	1	18.4	10.3	5	60.6	29.4
4	15.5	29.4	2	20.5	11.5	10	75.1	43.4
5	12.7	20.4	3	21.6	12.2	15	86.0	55.3
6	11.3	15.5	4	22.3	12.6	20	91.2	65.6
7	9.7	13.0	6	23.0	13.0	25	95.8	74.1
8	8.6	11.2	8	23.6	13.3	30	100.0	81.2
9	7.6	9.9	10	23.7	13.5	40	104.7	89.1
10	7.0	7.3	12	23.9	13.5	50	106.5	94.4
			14	24.0	13.6	60	107.2	95.9
			16	24.1	13.7	70	107.8	97.4
			40	24.6	13.7	80	108.0	98.5

Table 2. Error on the solar diameter measurements

r_0 (cm)	ΔD ($''$) (L_0 infinite)		L_0 (m)	ΔD ($''$) ($R_\tau \leq 1$)		R_τ	ΔD ($''$) (L_0 infinite)	
	$R_\tau \leq 1$	$R_\tau \succ 1$		$r_0 = 2$ cm	$r_0 = 4$ cm		$r_0 = 2$ cm	$r_0 = 4$ cm
2	0.9	1.8	0.5	0.5	0.3	1	0.9	0.5
3	0.6	1.2	1	0.6	0.3	5	1.8	0.9
4	0.5	0.9	2	0.6	0.4	10	2.3	1.3
5	0.4	0.6	3	0.7	0.4	15	2.6	1.7
6	0.3	0.5	4	0.7	0.4	20	2.7	2.0
7	0.3	0.4	6	0.7	0.4	25	2.9	2.2
8	0.3	0.3	8	0.7	0.4	30	3.0	2.4
9	0.2	0.3	10	0.7	0.4	40	3.1	2.7
10	0.2	0.2	12	0.7	0.4	50	3.2	2.8
			14	0.7	0.4	60	3.2	2.9
			16	0.7	0.4	70	3.2	2.9
			40	0.7	0.4	80	3.2	3.0

R_τ parameter. For the considered seeing conditions, it is observed a growth of the time difference Δt for small R_τ values which reaches a limit value. For the mean seeing condition of Calern Observatory, the error on the time ransit is equal to 15.5 ms ($0.5''$ on the diameter measure-ients) for R_τ equal to 1 (short exposure frames) which corresponds to the error due to the seeing ($r_0 = 4$ cm). It s multiplied by a factor 2.8 then 4.2 when R_τ value goes om 10 to 20. It remains to a constant value of about 100 ms ($3''$ on the diameter measurements) for the higher alues of the R_τ parameter. Consequently, the precision oss is about 280% when R_τ goes from 1 to 10 and about 420% when it becomes equal to 20 (see Tables 1 and 2).

We can notice finally that, although long exposure rames are obtained in best seeing conditions, the precision is worse than that we obtain in case of poor seeing onditions but with short exposure frames (with $R_\tau \leq 1$ nd $r_0 = 2$ cm, $\Delta t = 28$ ms while with $R_\tau = 10$ and $r_0 = 4$ cm, $\Delta t = 43$ ms). Thus, to have at least same accuracy's time contact than for poor seeing conditions, R_τ needs to be less than a factor 5. Thus, the R_τ parameter appears to be fundamental in the solar astrolabe experiment. A knowledge of time turbulence properties is then suitable to adjust experimental parameters and improve accuracy of diameter measurement performed with the solar astrolabe. Table 1 summarizes the results on the time contact error obtained from this simulation while Table 2 presents the same results but for the solar diameter measurements.

4. Conclusion

Solar diameter measurements performed at Calern Observatory astrolabe during two solar cycles (22 years) shows variations. These variations leaded to many studies and one cause often advanced is the Earth atmosphere. It is then in order to quantify how the atmospheric turbulence effects contribute to the error in the solar diameter estimations that the present work was developed. It is based around a numerical simulation of the measurements at the solar astrolabe in various observation conditions. The first step was to simulate images of the Sun as those observed at the solar astrolabe through the Earth atmosphere. A synthetic image of

the Sun was then needed. It was built using a model of the limb darkening function. A fractal model was after used to generate wavefronts randomly perturbed by the atmospheric turbulence and therefore optical responses of the whole system atmosphere and instrument. They were generated for various observation conditions and used to obtain the solar images. The second step was to simulate the astrolabe experiment and to define the needed parameters for the diameter measurements. The observed trajectories of both direct and reflected images are then built for various observation conditions. These are defined by the Fried's parameter, the spatial coherence outer scale of wavefronts and the ratio of the exposure time to the atmospheric characteristic time. The intersection point of the trajectories corresponding to the Sun transit time by the small circle, was then determined linked to the observation conditions. The study of the error due to atmospheric turbulence effects was developed around the transit time behavior with the observation conditions. Results show a decrease of the error with good seeing conditions whatever the used exposure times. The precision is however better in case of short exposure times than for long ones. A growth of the error is observed with the values of spatial coherence outer scale. It is significant only for small values of the outer scale and limited after by the error induced by the seeing. The error behavior is more critical with the exposure time relatively to the turbulence characteristic time. The error increases rapidly with the time ratio in order to reach a limit value. Thus, to have at least the same accuracy on the diameter measurement in poor seeing conditions that what we have with good seeing but using long exposure frames, this parameter needs to be less than a factor 5. This ratio seems then to be fundamental for the precision of the measurements with the solar astrolabe. To improve measurement diameter accuracy with the solar astrolabe, knowledge of time turbulence properties is suitable to adjust experimental parameters.

Acknowledgements. This work has been performed with support of the Observatoire d'Alger (C.R.A.A.G) and the French Foreign affair Ministry in the framework of scientific cooperation between France and Algeria (contract 96 MDU 357).

References

Aime C., Borgnino J., Kadiri S., et al., 1986, J. Opt. Soc. Am. A 3, 1001
Allen C.W, Astrophys. Quant., 1973, Athlone (ed.), p. 169
Beaumont H., Aime C., Sanchez L., Lanteri H., 1996, ESO Workshop on Science with the VLT interferometer. Garching-bei München
Bode H.J., Buchner R., Mushardt M., 1995, Sterne Weltraum 34, 646
Borgnino J., 1990, Appl. Opt. 29, 1863
Brown T.M., Elmore D.F., Lacey L., Hull H., 1982, Appl. Opt. 21, 19, 3588
Brown, Dalsgaard, 1998, ApJL v 500, L195
Delache Ph., Laclare F., Sadsaoud H., 1985, Nat 317, 548
Fried D.L., 1966, J. Opt. Soc. Am. 56, 1372
Gavryusev V., Gavryuseva E., Delache P., Laclare F., 1994, A&A 286, 305
Irbah A., Laclare F., Borgnino J., Merlin G., 1994, Solar Phys. 149, 213
Laclare F., Demarcq J., Chollet F., 1980, C. R. Acad. Sci. Paris, 291B, 189
Laclare F., 1983, A&A 125, 200
Laclare F., Merlin G, 1991, C. R. Acad. Sci. Paris, 313 SII, 323
Laclare F., Delmas C., Coin J.P., Irbah A., 1996, Solar Phys. 166, 211
Lane R.G, Glindemann A., Dainty J.C., 1992, Waves Random Media 2, 209
Leister N.V., Benevides Soares P., 1990, C. R. Acad. Sci. Paris, 313 SII, 399
Moussaoui R., Irbah A., Abdelatif T., et al., 1998 (submitted to Solar Phys.)
Neckel H., 1995, Solar Phys. 156, 7
Noël F., 1995, A&AS 113, 131
Roddier F., 1981, Progr. Opt. XIX, Wolf (ed.), No. 18, 283
Sanchez M., Parra F., Soler M., Soto R., 1995, A&AS 110, 351
Toulmonde M., 1997, A&A 325, 1174
Wittmann A., Bonet Navarro J.A., Wöhl H., 1981, The physics of Sunspots, Sacramento Peak Nat Observ., p. 424
Wittmann A., Alge E., Bianda M., 1991, Solar Phys. 135, 243
Wittmann A., 1997, Solar Phys. 171, 231
Ziad A., 1993, Univ. de Nice-Sophia Antipolis, Thesis